ELECTRICAL ENGINEERING AND ENERGY

Vol. 5 No. 2 (2026)

eISSN: 3062-3979

ELENE press

Electrical Engineering and Energy
Volume 5, Issue 2, Published: August 31, 2026
e-ISSN: 3062-3979

Electrical Engineering and Energy
Volume 5, Issue 2, Published: August 31, 2026
e-ISSN: 3062-3979

Contents

Research Articles:

ELECTRICAL ENGINEERING AND ENERGY

OPEN ACCESS

Selecting and Estimating Optimum Passive Designs of Energy Efficiency in Educational Buildings in Turkey

Ashraf Najmaldeen Hussein Hussein[1], Mustafa Acaroğlu[2]

[1] Ministry of Electric, State Company of Electricity Power Northern Region, Al shaheed Al Mohandes Abdullah Hamza Ahmed Power plant, Kirkuk, Iraq

[2] Selçuk University, Mechanical Engineering Department, Konya, Türkiye

Submitted:12. December 2025
Accepted :19 January 2026
Online First:21 January 2026

Corresponding author
Mustafa Acaroğlu
acaroglu@selcuk.edu.tr

DOI:10.64470/elene.2026.23

Abstract: The consumption of energy in building sector consists about 40% of energy consumptions by words. In this investigation we analysis using the passive design in educational buildings by selecting the Technology faculty building in Selçuk university at Konya city as example of Tik-tip project .To estimate the optimum case of passive designs, firstly proposal two new educational building envelopment (cubic building with 1:1 aspect ratio and cylindrical building) at same floor area of original existing envelopment at same façades design and more compact by less outdoor walls and then analysis to use eight passive designs (orientation , double façades, window wall ratios, court yards, green-lands and environment's area, shading device, set temperature and building tightness) in each new envelopments by simulations each ones using Autodesk Revit 2020 and analysis optically same designs by Ecotect 2011 based on actually yearly weather data selecting it in NASA weather data web site .At the result of analysis the proposed the new envelopment's we have more energy efficient at each one about %16.7 decreasing in cooling load and %20.76 saving of heating load in cubic building with % 19.9 saving in cylindrical envelopment and then have saving in total yearly air-conditioning load about % 19.3 and % 18.75 in cubic and cylindrical envelopment respectively. A last when used the other passive designs in optimum case we have total energy saving in air conditioning load about %33.36 in cubic envelopment and %30.9 in cylindrical envelopment when compared it with existing building envelopment of technology faculty in Selçuk University.

Keywords energy efficiency, green energy, passive designs,

1. Introduction

The building sector is identified as the leading global consumer of energy. Adopting energy-efficient technology innovations has been recognized as the most promising approach to reduce energy consumption in buildings. However, the adoption of such technology is significantly lacking due to traditional techno-economic thinking that lacks a human focus. Energy culture has been identified as a field of research that successfully overcomes the traditional techno-economic focus of technology diffusion. However, current energy culture studies on the adoption of energy efficient technology innovations in buildings are limited to exploring specific energy cultures rather than investigating the holistic energy culture maturity that guides the gradual diffusion of energy efficient technology innovations. Conversely, cultural maturity has been studied in other areas of cultural research, such as safety cultures (Soorige et all, 2022).

Today, buildings still account for almost half of global energy consumption and carbon emissions. This highlights the need to increase energy efficiency requirements worldwide in a concerted effort to reduce the construction industry's impact on the environment. Current energy policies are moving towards a design based on airtight and highly insulated envelopes. As a result, energy efficient homes have been found to have inadequate indoor air exchange rates, affecting indoor air quality and resulting in higher latent loads. Increased indoor humidity, combined with the increasing trend of using bio-based building materials, can easily support mold growth and facilitate indoor organic proliferation. The proportion of buildings damaged by mold is estimated to be 45% in Europe, 40% in the USA, 30% in Canada and 50% in Australia, highlighting the magnitude of this problem. Beyond the economic loss resulting from the remediation work required to correct building deterioration due to fungus, mold also has significant negative health effects on building occupants. Data shows that the incidence of asthma symptoms is higher in new, energy-efficient buildings with poor ventilation. This article explores the impacts of building sustainably on the indoor environment in relation to the risk of mold growth. Conducive conditions for growth, causes of growth, effects on health, and possible solutions are discussed. The results are a step towards a more precise and detailed understanding of mold growth to support policymakers and promote sustainable housing standards (Brambilla, 2020).

In general, the design process of a building; concept design, domestic design, advanced design and detailed design stages. During the concept design, a project group is formed to determine the needs of the building together with the stakeholders. At this stage, project goals and design requirements (site orientation, envelopment shape, initial services and building system) are determined and classified into 3 to 8 dimensions in terms of CAD software dimensions (Table 1).

Table 1 The dimensions meaning in CAD software system.

	Dimension	Meaning
1-	3D	Dimensions
2-	4D	+ time
3-	5 D	+ Cost
4-	6D	+ Sustainability
5-	7D	+Time schedule
6-	8D	+Safety

The aims to articulate a fundamental well-being framework that integrates thermal and photobiological needs with biophilic proposals to characterize positive links with Arctic climates for energy-efficient buildings. A scoping literature review was conducted to discuss the thermal and photobiological needs of building occupants in relation to biophilic recommendations and Arctic climatic conditions. As a case study, the shortcomings of current building practices in Cambridge Bay, Nunavut, Canada, related to well-being, indoor-outdoor connections, and energy efficiency needs are examined. The proposed well-being framework for positive indoor-outdoor connections in Arctic buildings integrates (i) thermal and (ii) photobiological indicators based on biophilic proposals. The integrated health framework enables the characterization of thermal and (photobiological) lighting adaptation scenarios that respond to Arctic weather, daylight and photoperiods, and energy efficiency. Intermediate spaces are also proposed as a proposed architectural solution to address integrated wellbeing framework energy efficiency in arctic buildings. Overall, the proposed framework can help architects, building designers, and stakeholders develop more architectural solutions for positive, energy-efficient indoor-outdoor connections for Arctic buildings and their inhabitants (Abazari et al, 2022). Using ground raw perlite through alkali activation to produce a variety of construction materials such as plaster, grout and concrete can provide economic and environmental advantages by reducing the consumption of Portland cement. The aim of this study is to produce cement-free pastes and cement-free mortars based on alkaline activation of raw perlite and standard sand. Experimental finding revealed that the addition of 0.25% H_2O_2 (perlite by mass) to the mixtures enabled the production of lightweight pastes and mortars with lower density and lower coefficient of thermal conductivity without a significant loss of ultimate strength. The developed perlite-based gas geopolymer is an environmentally friendly and energy efficient solution for buildings. Based on the results, more than 0.5% H_2O_2/Perlite and more than 45% water/Perlite should be avoided for both putty and mortars. To obtain optimum results in terms of workability, strength, density and thermal conductivity, it is recommended that the H_2O_2/Perlite ratio be 0.25% and the Water/Perlite ratio be 40% for all samples (Acar, 2023).

Phase change materials (PCMs) have great potential to improve building thermal comfort and save energy towards energy-efficient buildings. The current study sheds light on the passive use of PCM in a thin building envelope in an extremely hot location using EnergyPlus software. The thermal contribution of PCM to indoor thermal comfort was evaluated considering average temperature fluctuation reduction (ATFR), thermal load balancing reduction (TLLR), and operating temperature reduction (OTR). Additionally, total average heat gain reduction (AHGR) and equivalent CO_2 emissions and electricity cost savings (ECS) are discussed to measure energy savings. Simulation results demonstrated the effectiveness of PCM on the hottest summer days. Quantitatively, PCM contributed 5 ◦C- 6 ◦C to ATFR, along with TLLR and OTR, contributing an average of 38%-59% and 6 ◦C, respectively. According to the energy saving analysis, thanks to PCM integration, the total daily AHGR ranged from 66.6% to 76.5%, with the roof sharing the most. The results also demonstrated environmental and economic benefits, with a reduction in CO_2 emissions of up to 2 kg/day and ECS of up to 250 IQD/day. As a result, PCM can significantly improve building performance when passively integrated with thin envelope elements in extremely hot locations (Al-Yasiri,2023). When PCM with the possibility of phase change was used, annual energy use decreased by 28%, demonstrating that the possibility of phase change is very effective in reducing energy consumption. In addition to BioPCM M182/Q21, several BioPCMs with different enthalpy-temperature curves were used and it was observed that Q21 and Q23 BioPCMs fully met the heating needs of the building and reduced energy consumption in the building cooling section by 23.4% and 22.1%, respectively. Considering this, it has been found that there are more suitable options. Considering the effect of metabolic rate on PCM usefulness, in the range of 99-180 Watts per person, the addition of PCM to the building led to lower energy demand (Alharbey,2022).

Developing methods to recover waste heat and share it within a neighborhood can reduce that neighborhood's energy footprint and reduce its dependence on electrical grids. A mixed-use neighborhood consisting of retail, residential and greenhouse buildings was modeled to develop a holistic energy sharing strategy design. The waste heat recovery and distribution network at the neighborhood level is modeled in the EnergyPlus-DesignBuilder joint simulation platform. The energy sharing methodology is applied to different neighborhood configurations and neighborhood densities. Results show that by applying energy-efficient design and integrated energy sharing methodology with on-site solar, a net energy reduction of 74% was achieved in the mixed-use neighborhood compared to a design that complies with the minimum requirement of applicable energy codes. Similarly, a net 90.46% reduction in greenhouse gas (GHG) emissions is achieved by energy sharing and on-site carbon capture using a neighborhood greenhouse (Muslim, 2023).

Phase Change Materials (PCMs) improve cementitious composites by exploiting latent heat capacity, reducing heating and cooling demands. Thermal Energy Storage Aggregates (TESAs) were created using Parafol 18–97 and Parafol 20Z PCMs. Sand was partially replaced by TESAs and cork granules. Analyzes evaluated physical, thermal and mechanical properties, revealing favorable phase change temperatures and remarkable latent heat values in TESA-A and TESA-B. While TESAs reduced mechanical properties, they outperformed cork granules. TESA-mortar samples exhibited acceptable properties, with TESA-50 showing the best energy-saving performance and longest time delay. These findings highlight the potential of PCM-inoculated fungal granules in energy-efficient cement mortar (Ates, 2024). Approximately 12% of greenhouse gas emissions in the EU come from buildings. More energy efficient technologies should be implemented to reduce emissions from buildings. To achieve this, drivers for the implementation of energy efficient technologies are important. Interviews were held with different actors within the scope of a city district development project to find drivers for the implementation of energy efficient technologies in buildings. These drivers were tied to different phases of a building project to see when they had the highest potential impact. Connecting drivers to various stages of the construction process has not been investigated before. As a result, they are the drivers that have the most impact on the Planning Program phase and the Project Planning phase. The most frequently mentioned drivers are cost reduction from lower energy use, greater knowledge in the construction industry, long-term perspective on the customer, both mentioned by ten out of 18 respondents, and National requirements and customer demands, both mentioned by eight out of 18 respondents. The most obvious driver appears to be economic gains, and LCC calculations are therefore a very important tool to demonstrate potential economic gains. Training with subsequent certification in working with energy-saving technologies and building techniques can be a driving force and will also combat the lack of knowledge within the business. In-house information on the Customer, Long-term perspective on the Customer and Customer demands are the three big driving forces. Therefore, clients on building projects should aim to have good in-house knowledge and a long-term perspective to be able to identify the right requirements and steer energy efficient technologies (Carlande, 2022).

Understanding and predicting the energy performance of existing buildings and new construction is crucial to decarbonization. Instead of using simulation software, multiple regression models are used to accelerate this process to predict building energy consumption while ensuring indoor thermal comfort. However, previous predictive models prioritize reducing energy demand with a limited focus on thermal comfort. This study aims to support decision-making during retrofit and new construction planning when developing a predictive model. An air-conditioned office building served as the reference building for simulation. 21 design parameters were analyzed, including weather, building envelope, internal loads, ventilation and temperature settings. Stepwise regression results revealed significant variables in the final model, with 8, 9, 13 and 6 variables remaining for peak cooling load, annual cooling load, overheating hours (WE) and Environmental Quality Index (EQITC) for thermal comfort in the perimeter and core 5, 6, 8 and 5 variables for regions respectively. Additionally, information was provided on important variables related to cooling load and thermal comfort, respectively. Weather- and envelopes-related variables such as cooling degree-days, global solar radiation, solar heat gain coefficient (SHGC), and U-value have the highest impacts on the cooling load. For thermal comfort, variables such as temperature set point, occupant activity level, and factors related to window sunlight transmission performance such as SHGC, window area ratio, and overhang projection ratio have proven to be effective. Overall, this study provided accurate models for evaluating optimal strategies for energy efficiency and thermal comfort in early design stages and advancing building performance practices (Chen X, 2022).

A new life cycle cost (LCC) analysis method is presented to evaluate the long-term cost-effectiveness of energy efficiency features in buildings by accounting for future costs associated with earthquake-induced damage to these features. Buildings located in a seismic zone are likely subject to lifetime earthquakes, and their nonstructural elements, such as energy efficiency features, may suffer varying levels of damage requiring repair or replacement to restore a satisfactory level of building energy efficiency. However, current LCC analysis methods have ignored such earthquake-related costs, potentially leading to unreliable cost-effectiveness assessment of energy efficient buildings. To address this issue, we propose a method to rigorously quantify the expected cumulative future cost due to repair/replacement of earthquake-damaged energy efficiency features and then integrate this cost into the LCC analysis. The new method is demonstrated using a medium-sized office building located in a high seismic area with a Mediterranean climate. The costs associated with the initial installation, as well as future energy consumption, environmental impacts and seismic damage of two alternative types of window installation with different levels of energy efficiency are calculated and compared. It has been found that when the cost of seismic damage is considered, the cost-effectiveness of energy efficiency features can be noticeably reduced and, equivalently, the payback period for building energy efficiency investment is extended (Liu, 2017).

So, in the relevant literature shown Table 2, the investigators research and optimizations the parameters of building envelopment and the passive design used in the different type of building and calculated the amount of energy consumptions in each iteration with energy saving to increase energy efficiency of buildings by using different building energy simulation or coding based on the actual or virtual weather data of the climate of it.

Lastly previous studies have extensively investigated parameters of passive design individual such as devices of shading, (WWR Window to wall ratio), and insulation materials, limited research has addressed the combined impact of building form compactness façade s and multiple passive strategies in educational buildings under specific climates such as Konya city. This study addresses this gap by integrating form optimization with passive design strategies by suggesting using two complementary simulation program tools with two.

Table 2 Energy efficient parameters literature

Year	Researchers	Climate	Parameters	Total Energy Efficiency Saving	Programming and Investigation Methods
2024	Soliman (Soliman, 2022)	Alexandria (Egypt)	Windows orientation and Shading devices Windows glass Vegetations Green roof Internal Temperature Site	4%	Revit and Design builder programs
2024	Naji Alhasnawi et all.(Alhasnawi, 2024)	Iraq	Smart Urban Buildings (SUBs)	%38	mproved Sine Cosine Algorithm (ISCA)
2024	Reddy et all.(Reddy, 2024)	Virtual	PCM	%19-59	A comprehensive review
2023	Cuce et all. (Cuce, 2023)	Virtual	Alternative novel insulation plaster (NIP)	%47.9	Experimental
2023	Uzun(Long, 2023)	Vietnam	Pareto-optimal building envelope	%8.48	AI optimization algorithms
2023	Wasim et all.(Wasim, 2023)	Virtual	Glazing type, Construction wal, Insulation layers WWR, floor and roof types	%28.7	Revit, Matlab, Design builder and energy plus
2023	Müller et all.(Müller, 2023)	EU	new ventilation approache	%28	Mathematical optimization
2022	Jakovic and Goia (Jankovic, 2022)	Virtual	Duable envelopment w	---	Statistical DOE method
2022	Zhou and Razaqpurm(Zhou, 2022)	Virtual	Tromb wall with PCM	%20	static

2021	Bui (Bui, 2021)	Texas Melbourne	Using Biomimetic adaptive electrochromic windows in shading and window materials	(19.3-23.5)%	python coded
2020	Geçimli (Geçimli, 2020)	Different climates	Technical solutions, façade, chimney, sound insulation, ventilation, light tube, solar panels, rainwater	86%	Bee gaming
2020	Anwar et al. (Anwar, 2020)	Australia	Green roof	(13.6 -11.7)%	Simulation with practice
2019	Li and Wang (Li, 2019)	Chaina	Building direction, solar roofs, absorbability, WWR	---	Wizard Coding
2019	Burratti et al.(Buratti, 2019)	Italy	Aro-gel on windows	17%	TRYsis program
2019	Li et all. (Li, 2019)	Ningbo	Green roof, vertical landscaping	2.8%	Design builder program
2019	Esen (Esen, 2019)	Antalya	Shading elements, TS-825 insulation	56.70%	Green building studio
2019	Fabbri et al. (Fabbri, 2019)	Parma (Italy)	Microclatic with the color of the courtyard and interior walls	----	Envi-met simulations
2019	Rivera-Gomez et al. (Rivera-Gómez, 2019)	Spain	Courtyard aspect ratios	---	Experimental
2019	Çimen (Çimen, 2019)	---	Vermicute plant and normal wall insulation	66.70%	Practical
2019	Koç (Koç, 2019)	Antalya	Shading elements, window-wall ratio	(6-14)% Primary energy savings	Matlab coding
2019	Koyun and Koç (Koyun, 2017)	Antalya	Wall and window ratio and material, Roof height	---	Simulations
2019	Cüce et al.(Cüce, 2019)	---	PV glasses, active glass systems	(16-22)%	Simulations

2. Software and Program Selection

Today, energy efficient buildings are mainly concerned only with existing standards when defining their performance. This approach is correct only in terms of official competence to fulfill the requirements of legal rules and give people confidence. Beyond these facts, today's energy efficient buildings should be known not only in the context of current technology, but also in terms of the evolution of the equipment and design concept used in sync with the modernity of science. This article provides a historical and painstaking presentation of the evolution of techniques and concepts that led to energy efficient buildings as we know them today. An overview of the modern approach to the design of the main elements of such buildings is also presented. The article carries out a review of the current state of energy efficient buildings in terms of definitions and characteristics (Kishore,2022).

In these studies, used mainly two simulation programs to optimization the perfect design of passive design in the new proposal building design of Selçuk university technology faculty based on annual weather conditions of Konya city.

2.1. Autodesk Revit 2020

The Autodesk revit2020 program, the building will be drawn exactly like the three-dimensional real one. It is a 3D building design and analysis program (Yori,2019). In selecting the objects related to the shell of the building and determining their thermal properties, either the elements will be loaded and used by using the ready data in the program, or a new thermal property definition will be made using the same substance.

The location and the weather files data (climate conditions) of the building selected if the values of some world cities were contained from the program or determined with the Google Earth program to use the exact climate of the building and automatically updated to the Revit program (Figure 1).

Figure 1 The selection of the position of building from google-earth web sites (Earth, 2022).

NASA weather data were selected from NASA POWER web sites to their accessibility, because it was long-term consistency, with suitability for building simulations of energy at regions where high-resolution local meteorological data are limited weather characteristics or artificial data available. While national and global meteorological data were considered, the NASA data web-set provided a very comprehensive and actually annual weather data compatible with both Autodesk tools as Revit 2020 and Ecotect environment simulations program (Figure 2).

Finally, before calculating the cooling and heating energy consumption of the building, it is necessary to divide the building into different thermal areas (energy model). After division, the program will draw the energy model of the building, calculating the energy consumption for each area in one way or another.

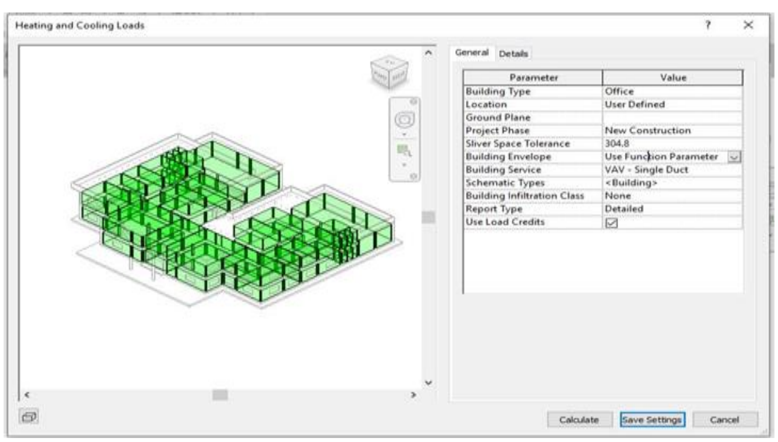

Figure 2 Energy models of building (Tulukçu, 2021)

2.2. Ecotect 2011

It is a software program used for analysis purposes for environmentally friendly buildings in the early stages of the design of buildings (Figure 3). Although Ecotect 2011 is the latest version and after 2016 Autodesk has replaced energy simulation and alternative solutions with Revit with internet-based green building studio, it is still the Ecotect program in the design stages of the building. Due to the gradual behavior of passive designs, the fusion of the building with the climate, and the optimization of the daylight and shading parameters gained by the building, and the behavior of the designs very efficiently at the stage of characteristics of the designs, 3D drawing drawings are still used in passive design analysis in the market and in the relevant sector, although they are simple compared to Revit and other architectural programs.

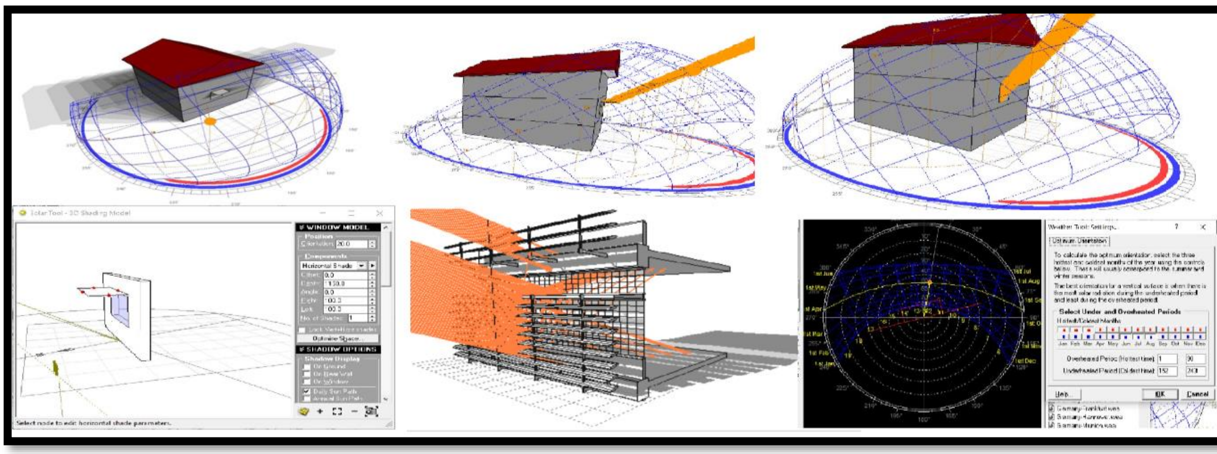

Figure 3 Passive design analysis by ecotect 2011 (Issa et all, 2009).

3. Methodology

3.1. Proposed Inside of Shells program Energy efficiency portability analysis

The material used in the square and cylindrical shells of the proposed new technology faculty was analyzed on the web for energy efficiency realization in energy optimization trials, and the Autodesk-inside program analyzed the newly proposed shells through the Autodesk-inside program.

The was primarily for detailed energy modeling of each envelopment and annual heating and cooling with total load calculations by Autodesk Revit 2020, while employed in the early design stages of early design to evaluate solar analysis, daylight usefully, shading performance, and orientation sensitivity. The geometric models were kept consistent across both platforms to ensure comparability of results. The key assumptions were related to properties of material, schedules of occupancy, and gains of internal load were harmonized between the two programs.

As a result of the analysis of energy transport in the use of passive, active (shell and insulation materials) and renewable energy systems, we understood the possibility of obtaining a higher (plus) building at zero (-31.8 kW/m^2/year) in the square shell, but the possibility of obtaining a building close to the cylindrical building (10.2 kW/m^2/year).

3.2. Passive Designs Analysis

3.2.1 Orientation

To select the best direction of educational building we have two sets of iteration shown below:

3.2.1.1. Normal Directions

In the first set of orientation analysis, we rotate the building to normal eight directions (North, Northeast, East, East South, South, West South, West, West North) for each proposal building (Figure 4 and 5).

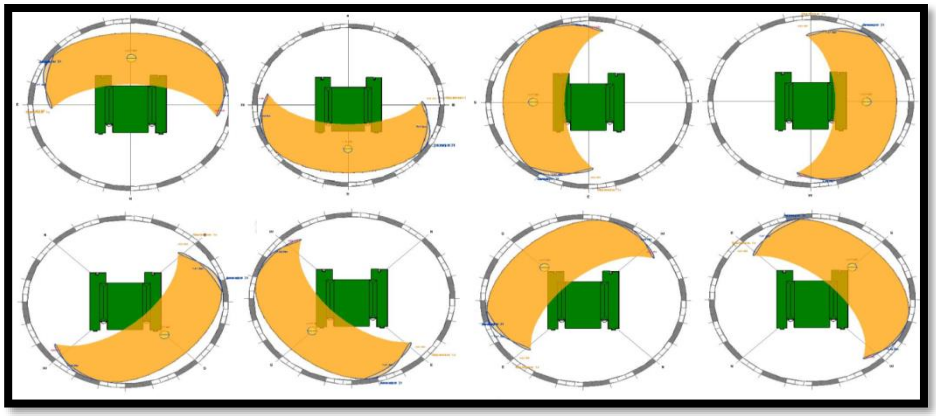

Figure 4 Normal direction analysis of cubic shell

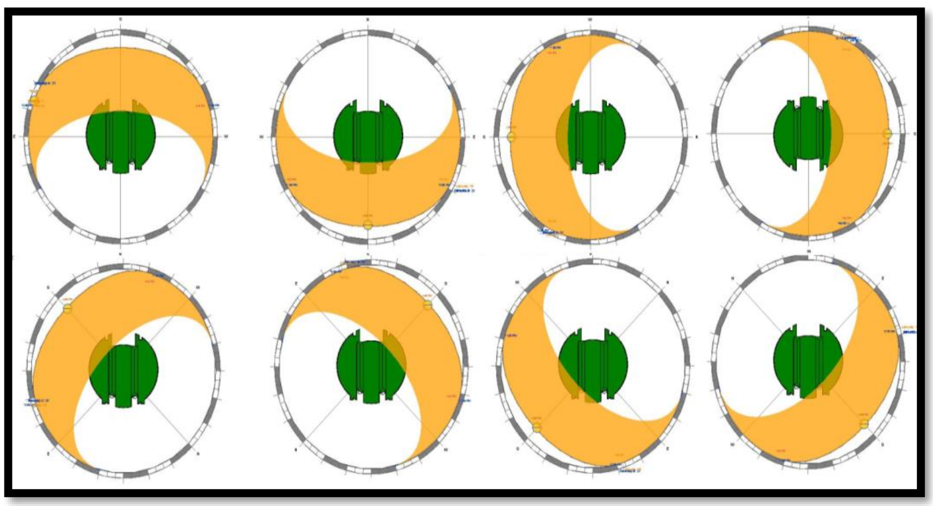

Figure 5 Normal direction analysis of cylindrical shell

3.2.1.2. Exact Directions

As a result of the optimum direction analysis in the Ecotect program, it was aimed to find the most productive direction by comparing the building with the most bearish direction (150 – 210) degrees and the energy consumption and south direction of 13 iteration construction with a difference of 5 degrees between these degrees (Figure 6 and 7).

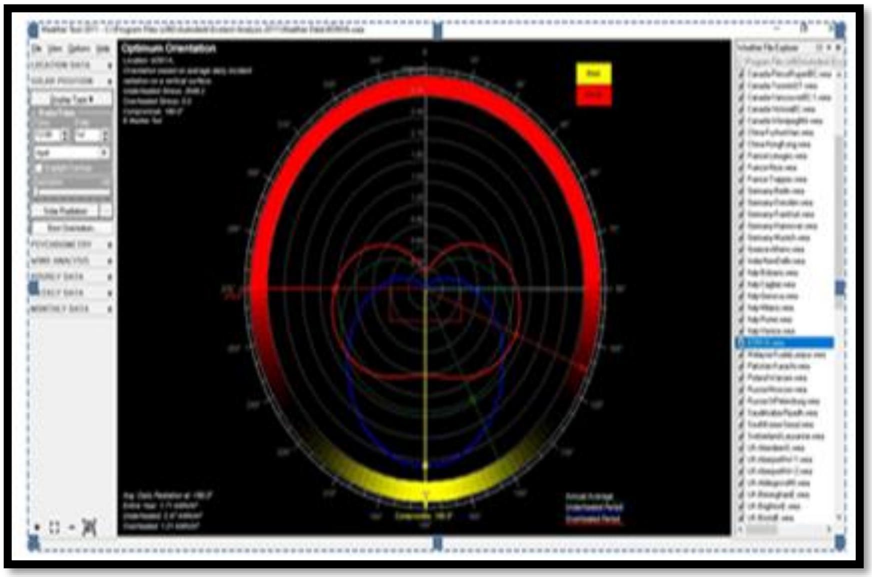

Figure 6 Selection of the optimum orientation of buildings by Ecotect 2011

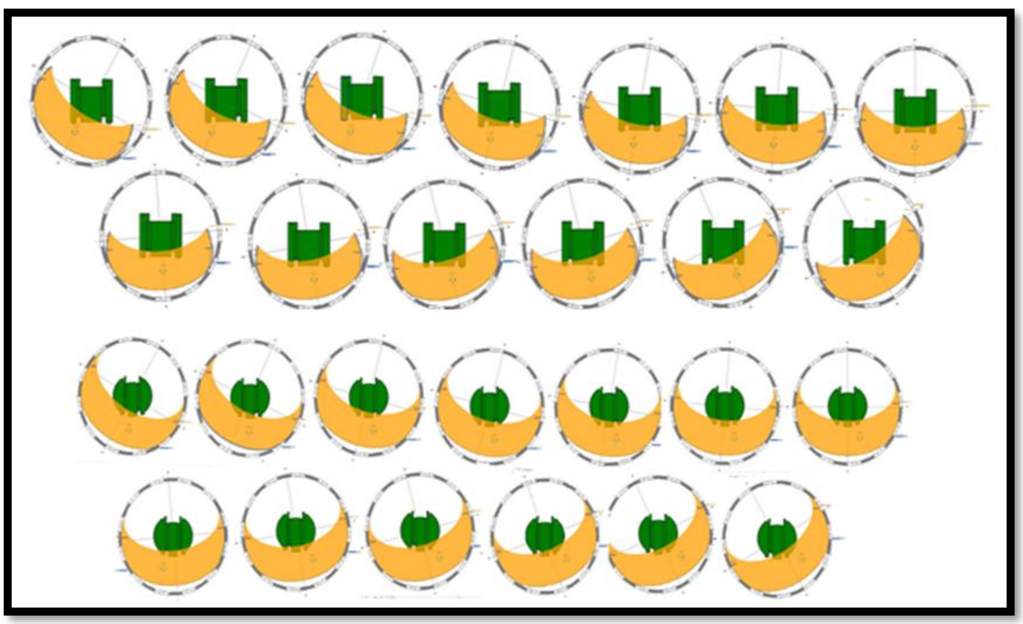

Figure 7 The Analysis of the exact optimum direction between (150-210) degree

3.2.2. Double Shall Walls

To reduce the heat loss or gain from outside walls used two types of double walls to achieved increasing in thermal resistance by utilizations the air buffered between walls by two methods, firstly by direct air gape (23 mm) between two walls because generally the walls thickness in turkey cannot be excess 64 mm, secondly by installed the greenhouse façade on building walls (Figure 8).

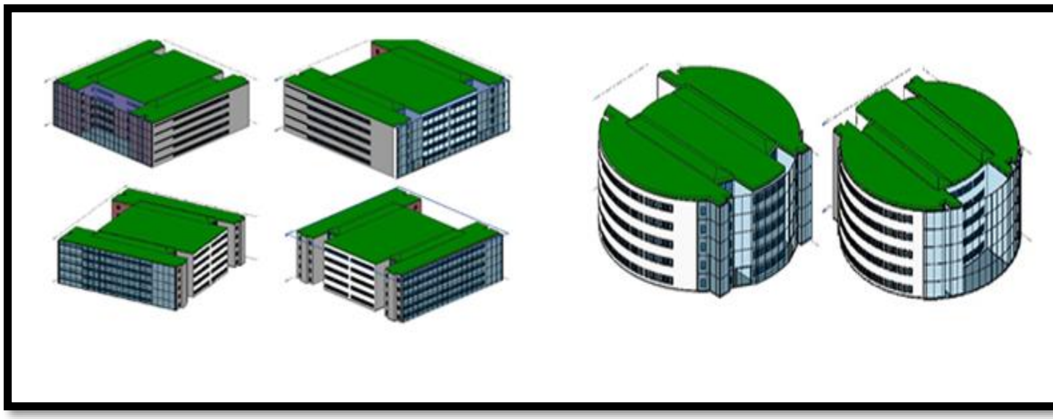

Figure 8 The green house wall installed in buildings model.

In the last stage, since the air-tampered walls between the air walls are more efficient, both shells connected in terms of efficiency level in the walls used the attach certification on the double facades.

1. Less efficient composition of two
2. Least + most bearish efficient combination
3. Best + second moment less efficient combination
4. Top month two-yielding combination
5. Second efficient + second bad combination
6. Second best + worst efficient combination

3.2.3. Window wall ratios (WWR)

In order to select the most efficient window-to-wall ratio in the four directions in the proposed shells, the amount of energy saving with the original shell window-to-wall ratio was calculated after placing the same type of window volumes used in the old building in the wall-to-window ratio on each façade (0%, 25%, 50%, 75%, 100%) in accordance with the ratios and analyzing the energy consumption (Figure 9 and 10).

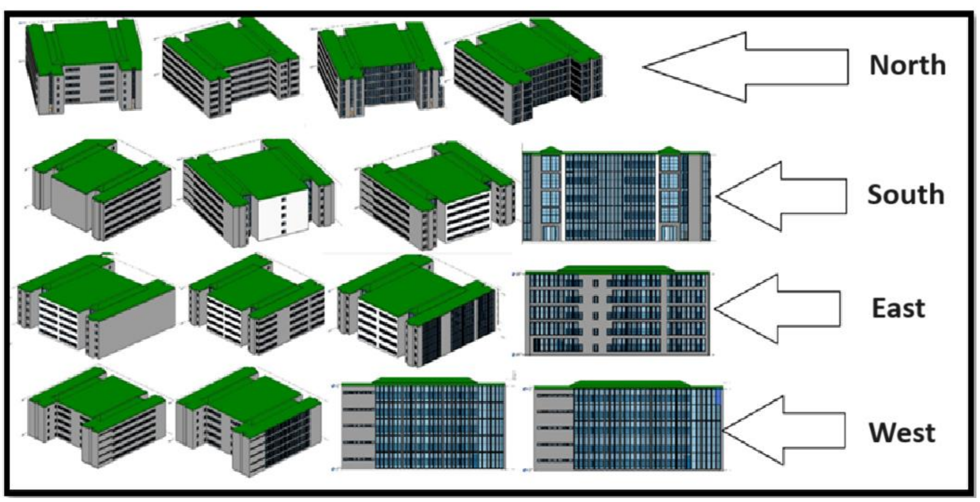

Figure 9. Images of sample trials on wall window proportions cubic shells

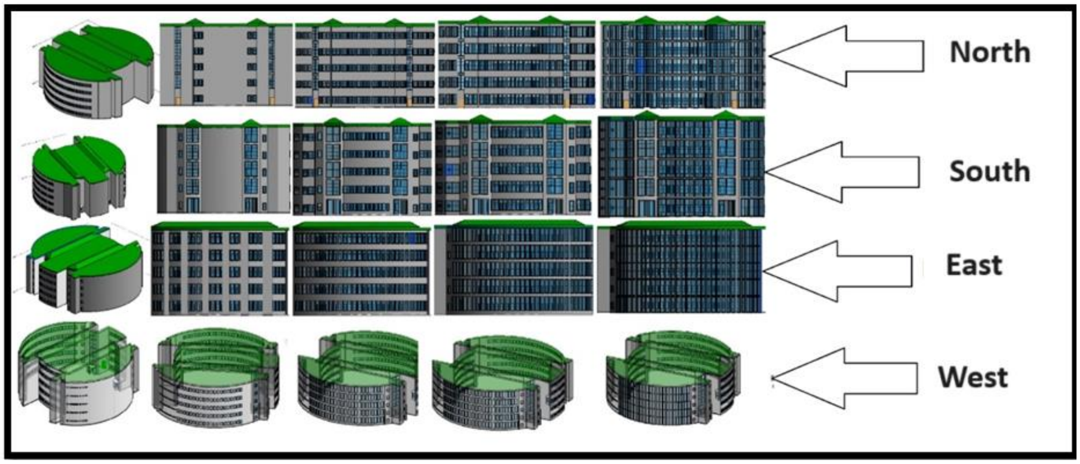

Figure 10 Images of sample trials on wall-window proportions in cylindrical shell

3.2.4. Courtyard

In the proposed cubic and cylindrical buildings, the new building was modeled and used in two ways, using the area of approximately (25 × 6.3) m, which is the middle part of the original building, as a courtyard to increase the natural daylight and passive air conditioning of the building, and taking the aspect ratio of approximately 2:1 (Figure 11)

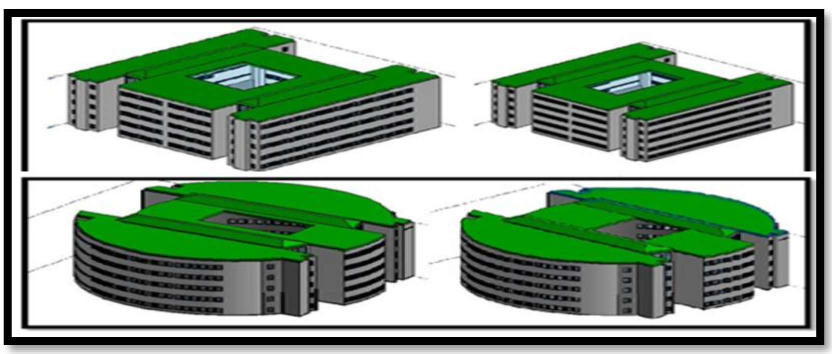

Figure 11 The shapes of courtyard

3.2.5. Landscaping and Surrounding Area

Since Selçuk University is in the south/west part of Esentepe and generally pine trees are grown in the green areas and gardens of Selçuk University, the height of the pine trees will be between (1.5 - 4.35) m by placing them as green and garden areas in the north and east directions around the newly proposed Technology Faculty. In our study, the average height of the trees was taken as 3m, with a gap of 2.75m between the trees in four rows of zigzag shape. The simulation was made to ensure that pine trees provide windbreaks in the winter and shade unwanted solar radiation in the mornings in the summer. On the other hand, the western perimeter of the building was chosen as a parking area for vehicles and areas for students to sit and do other activities between classes.

3.2.6. Shading Elements

Windows and controls, including shading systems, are among the most critical building components that affect both energy consumption and occupant comfort. With the increasing demand for fully glazed facades, designers and researchers are actively developing advanced control strategies to address the challenges posed

by excessive sunlight penetration and heat transfer. These strategies aim to align the benefits of natural light with the need for comfortable indoor environments and reduced energy consumption(Nazari, 2023).
Extended shading elements are used on the horizontal window, which is most conveniently used on the south facade. The following formula is used to obtain the optimum length (Woh) of window shading elements.

$$\text{Who} = \frac{H\ oh}{SLF} \quad (1)$$

3.2.7. Internal Conditions Parameters

3.2.7.1. Internal Temperature

In order to understand how much increase or decrease is possible in the internal temperature levels used, the comfort temperature levels that can be kept in annual, winter and summer seasons were analyzed in the psychometrics chart (weather characteristics chart) in the Konya climate in the Ecotect program.
After analyzing the air internal temperature comfort levels with Ecotect, reducing the adjustment level from 21.11°C to 20,19,18 and 17°C in winter and increasing the internal temperature from 23.33°C to 24 and 25°C in summer, energy saving in square and cylindrical buildings is achieved. analysis was made.

3.2.7.2 Building Tightness

In all experiments carried out in the Revit program, the density level of the building was taken as medium. Since the building density level is an important parameter in the air conditioning energy of the building's internal air due to its direct effect on the air leakage rate in the shell, square and cylindrical building shells were analyzed as dense (tied) and poor (lose) shells reaching the middle level.

4. Results and Discussion

This part presents the investigation results by simulation tools of the proposed envelopes of building and passive design parameters strategies, focusing on their energy consumptions impact like annual heating, and annual cooling with total air-conditioning energy loads demand.

4.1 Orientation

4.1. 1.Normal Directions

The results of the experiments, as a result of comparing the buildings with the original south orientation, were obtained as the South/North direction in the total air conditioning energy savings of the two shells shown in Figure 12 and 13 , and although the total energy savings between the north and south directions were 1.69% in the square shell and 0.42% in the cylindrical shell, the north direction in heating energy was achieved. and the same amount of consumption was obtained in the southern regions.

In both shells, the worst directions were the west and north-west and northwest directions, with energy consumption increases between -9.82% and -8.78% in the square shell and -11.16% and -9.56% in the cylindrical shell, respectively.

In the second stage, after obtaining the best direction for heating, optimum direction analysis was carried out in the Konya climate with the Ecotect program to find the exact direction in the energy efficiency of the building.

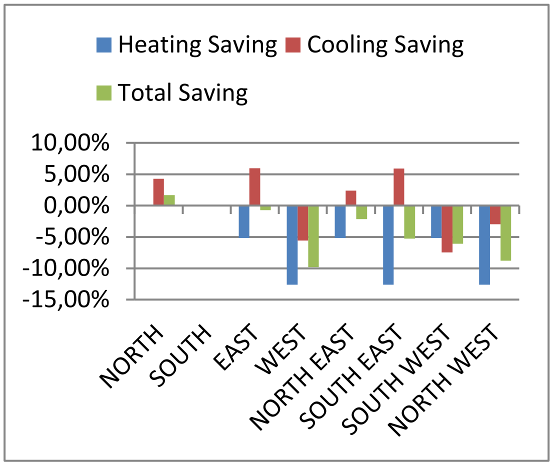

Figure 12 The energy saving of exact direction analysis in Cubic Shape Building

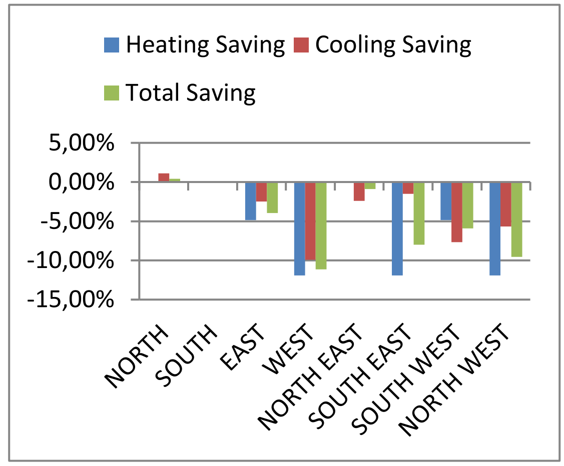

Figure 13 The energy saving of exact direction analysis in Cylindrical Shape Building

4.1.2 Exact Direction

As a result of the directional analysis in the square shell Show in Figure 7, there is a difference between the savings increase in the cooling load in the minus direction of 180 degrees (East direction) depend in suggestion at Figure 6 and the increase rate in every 5 degrees in the direction of increasing to 180 degrees (West direction) without any change in the heating load (0.7-1.15). It was calculated as (0.38-0.238).

Likewise, the cylindrical shell (150-210) degrees does not see any difference in the heating load or savings load, and even though there is a small difference in the energy consumption for every 5 degrees in cooling, the total energy saving, and increase is calculated between (0.34 - 1.84) %. He realized that there was little difference in the rate of energy consumption between the degrees (Figure 14 and 15).

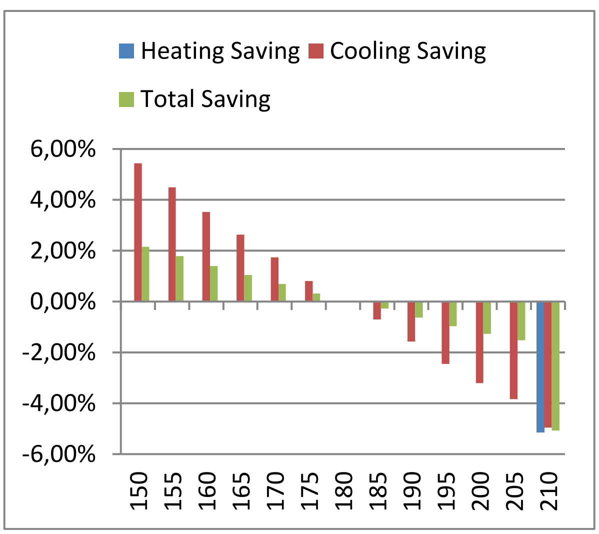

Figure 14 The energy saving in exact directions angle between (150-210) of Cubic Shell

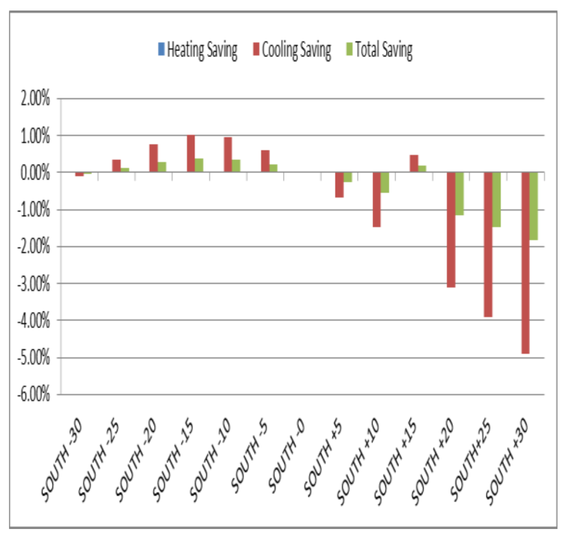

Figure 15 The energy saving in exact directions angle between (150-210) of Cylindrical Shell

4.2. Double Shall Walls

The highest energy efficiency in the square shell is on the south facade, where the total air-conditioning energy saving was 15.3% in the use of air-buffered walls, and in the use of greenhouses, the total savings on the south facade decreased by 8.23%. On the other facades, in the use of air-buffered double walls in the north 14.74%, in the east 10.24% and in the west 7.89%. They ranked second, third and fourth by achieving total energy savings.

On the other hand, the maximum total air conditioning energy savings on the other facades, except for the south facade, did not exceed 3.87% on each facade. In the Cylindrical Shell, the maximum savings in the double walls with air buffers were 14.36%, and in the northern, eastern and western walls, it was calculated as 11.99%, 8% and 7.05% (Figure 16 and 17)

In the last stage, since the air buffered walls between the air walls are more efficient was shown in figure 8, the results were obtained when the analysis was performed on the double facades of both shells depending on the efficiency level in the walls.

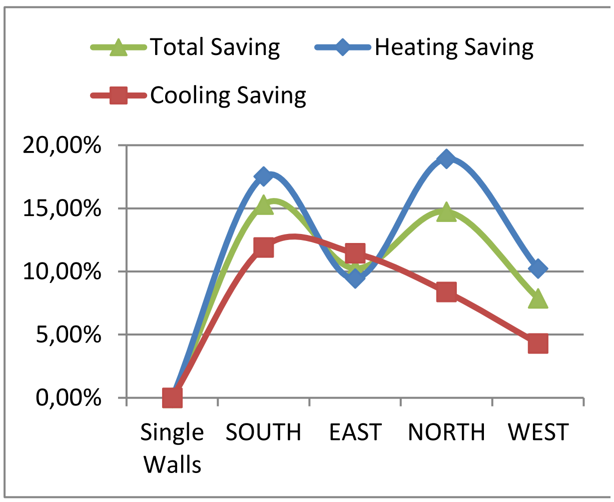

Figure 16 Energy saving in air-buffered double shell on facades of Cubic Shell

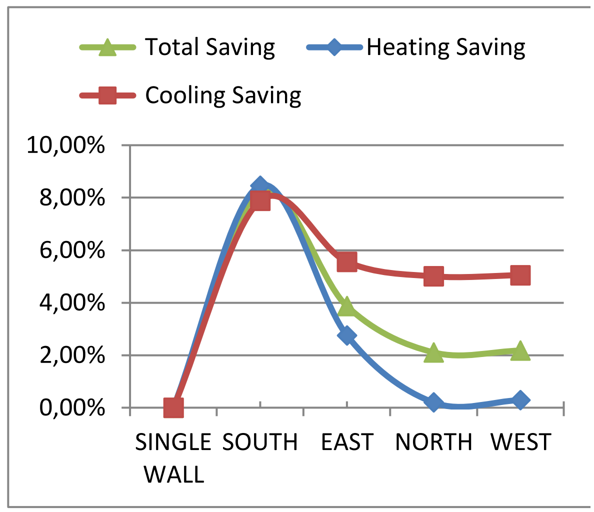

Figure 17 Greenhouse on the facades of the square shell energy-saving in the Double Shell

4.3. Window Wall Ratio (WWR)

As a result of the experiments, among the five wall ratios, the maximum energy savings were 2.86% and 0.97%, respectively, with 75% wall and window ratio on the south walls of buildings with square shown in figure 9 and cylindrical shown in figure 10 acceptances. At the second level, on the western walls, with a window wall ratio of 25%, the total energy saving is 1.68% in the square shell and 0.78% in the cylindrical shell, and on the eastern walls, with a similar window-wall ratio on the western walls, it is 0.39% and in the cylindrical shell it is 0.69%. savings in energy have been achieved. Finally, savings of 0.1% to 1.01% were calculated for square and cylindrical shells on walls without windows in the north direction.

4.4. Court-Yard

According to the analysis results, the heating loads in square and cylindrical shells are 3 times higher than the cooling load amounts in Konya, and since the courtyard is generally used in hot and hot dry regions, if the courtyard is used in Konya, it causes an increase in the total annual consumption energy due to the increase in heating energy. It was understood that the use of the courtyard was inefficient like shown in Figure 11.

4.5. Landscaping and Surrounding Area

In the use of landscape design, a 2.6% - 3.38% increase in heating load and a 7.27% - 8% increase in cooling energy were observed in square and cylindrical shells, resulting in a 4.787% - 4.98% increase in the annual air conditioning total energy.

4.6. Shading Elements

As a result of the analysis of the use of south facade shading systems, although the most efficient shading element in the square shell is the most efficient with a roof extension with a saving of 7.69% in terms of cooling load, the most efficient shading element in terms of total annual air conditioning load is 2.12% in terms of total annual air conditioning load, due to a -2.02% consumption increase in heating load. has provided.

4.7. Visual Analysis

In order to understand the effect of the sun path on the building in winter and summer seasons, Revit sun path feature is utilized, and it is seen that the landscape distribution is utilized as shading elements on all windows on the first floor of the square building, and a lower shading area is provided due to the rounding of the cylindrical facades on the south / north side (Figure 19).

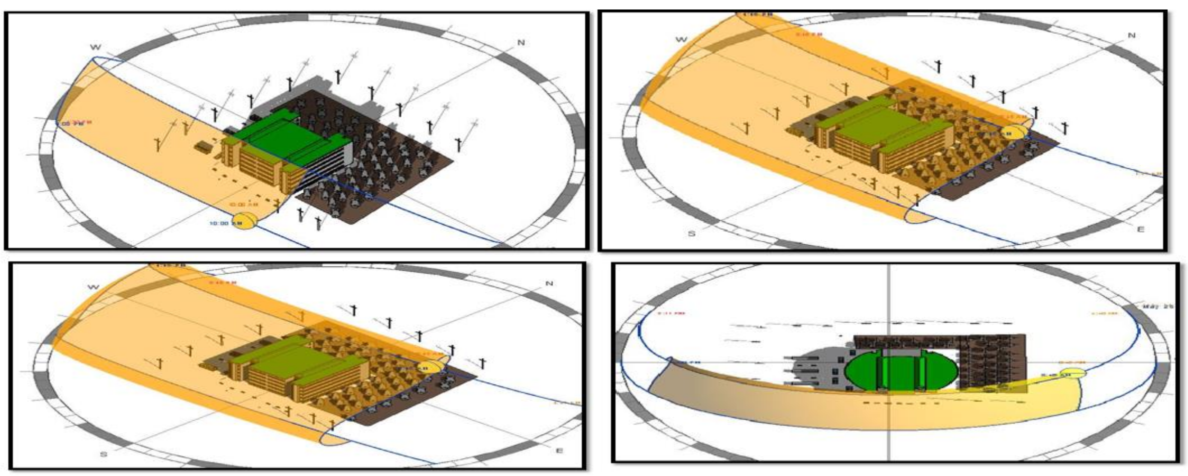

Figure 19 The visual analysis of landscape shading effect by Ecotect

4.8. Internal Condition Parameters

4.8.1. Temperature

By keeping the cooling and heating at two degrees each (19 °C, 25 °C) and (18 °C, 24 °C) at the indoor air settings, 12.47% and 9.68% savings were achieved in the total air conditioning energy of the building.

4.8.1. Tightness

As a result of the analysis, when making a mid-level comparison in the square shell, a -4.698% consumption increase in total air conditioning energy was calculated due to a -7.26% increase in energy consumption in the heating load in the poor shell and a -0.809% increase in cooling. At the strict level, total air conditioning energy was obtained as 1.65% due to a 3.023% saving in heating load and a -0.437% increase in energy consumption in cooling.

4.9. Discussion and Validating the Result with Similar Studies in Literature

Saffar, in his study conducted by he worked on a 100m² detached house model in the local architectural conditions used in Konya and Kirkuk, using the Design Builder drawing program and energy plus energy calculation simulation programs in nearly zero energy buildings. In the study, they calculated the savings in heating, cooling and lighting energy and proved that the maximum annual consumption fell below 44 kWh (Saffar, 2022).

In our study, in the square shell in its original form (513.184 kWh), it showed a decrease in annual energy consumption of approximately 41kWh, whereas in the cylindrical shell we proposed, we calculated that it was decrease of approximately 46 kWh was achieved. Although there was little difference in the study by Sarah Waleed SAFFAR based on weather conditions in 2021, the results were very close, and the building used was due to the square shell.

In the Bolu Gülezler Mansion reconstruction by (Akşit & Metin, 2022), they first worked on modeling in terms of heating energy and saving the energy consumed through the Design Builder program. In their study, they achieved 25% savings in total heating energy because of optimization of the building's form, orientation and spacing (surrounding land) (Akşit, 2022).

In our study, since Konya and Bolu are in the same 3rd geographical region in Turkey, the building shape (square 20.76%, cylindrical 99%), the building perimeter (square 2.6%, cylindrical 3.38%) and the internal temperature drop of the building in terms of heating savings in the same parameters were affected. Savings between (1.7-2.35) % were achieved. In the study conducted in Bolu, results showing interconnectedness were obtained due to the gain in heating load between (25.06-25.63) in the same scenarios used in this thesis. Since building shape is also effective in geographical regions, it would be a correct approach to choose building shapes according to geographical regions.

Yazgan and Koçak Soylu, compared the energy and cost savings in an anonymous hotel in Antalya in order to increase energy efficiency, considering the internal comfort parameters. By calculating a maximum of 7452250 kWh/year and a minimum of 500524 kWh/year in the energy consumed for 5 years in the occupancy rates and internal parameters in the years 2017, 2018, 2109, 2020 and 2021, they calculated a cost saving of 33256 TL/year in the hotel due to approximately 7% energy saving in interior comfort ((Yazgan & Koçak Soylu, 2022)).

In our study, energy savings in interior comfort parameters (indoor temperature, heating and building density ratio) were achieved between 2.07% and 4.245%, and the total annual energy saving was calculated as approximately 6%. The reason why it is 1% lower than the study conducted in Antalya is due to the fact that Antalya is a hot and humid region, and the cooling load is higher, and it plays a big role in the calculations. Accordingly, optimizing cooling loads in such climates would be a more accurate approach.

5. Conclusion

The early-stage decisions at results demonstrate related to building shape and form by using integration of passive designs technology can significantly increase saving in energy demand to cooling and heating process in educational buildings, offering by guidance practically for architect's design and planners in same climatic regions.

In the cubic shell passive design optimization made after the optimization of the parameters in the shell, it is understood that it will contribute to savings in total air conditioning energy of 33.36% in the square shell and 30.9% in the cylindrical shell, as seen in the chart below.

The passive designs are in their optimum state (Facade direction, air buffered double wall, window to wall ratio, building density ratio, shading with landscaping) and in their worst case when the internal air conditioning parameters are used in their optimum form (Internal temperature, Frequency ratio). We can save approximately 86-92% of air conditioning energy and classify it as a building with class B energy or close to zero energy.

Similarly, in the cylindrical shell, 83-91% savings can be achieved in the worst cases when the shell parameters, passive designs and internal air conditioning parameters are used in their optimum forms, and in the square shell, a building proposal with 1-3% lower savings can be achieved.
For future studies if needed to may extend this investigation work firstly by incorporating life-cycle cost analysis and thein occupant behavior modeling, and lastly validation using measured operational data from existing and proposal buildings.

Declaration of Ethical Standards

As the authors of this study, we declare that he complies with all ethical standards.

Credit Authorship Contribution Statement

A.N.Hussein: Software, Validation, Formal analysis, Writing -Original Draft, Visualization.
M.Acaroğlu: Investigation, Resources, Writing, Review & Editing, Supervision, Funding acquisition.

Declaration of Competing Interest

The authors declared that they have no conflict of interest.

Funding / Acknowledgements

No Funding

Data Availability

No datasets were generated or analyzed during the current study.

References

Abazari T, Potvin A, Demers CM, Gosselin L. A biophilic wellbeing framework for positive indoor-outdoor connections in energy-efficient Arctic buildings. Building and Environment. 2022; 226:109773.

Acar MC, Celik AI, Kayabaşı R, Şener A, Özdöner N, Özkılıç YO. Production of perlite-based-aerated geopolymer using hydrogen peroxide as eco-friendly material for energy-efficient buildings. Journal of Materials Research and Technology. 2023; 24:81-99.

Akşit ŞF, Metin CA. Isıtma Enerjisi Korunumunda Etkili Olan Tasarım Değişkenlerinin Değerlendirilmesi: Bolu Gülezler Konağı. 2022.

Al-Yasiri Q, Szabó M. Numerical analysis of thin building envelope-integrated phase change material towards energy-efficient buildings in severe hot location. Sustainable Cities and Society. 2023; 89:104365.

Alharbey RA, Daqrouq KO, Alkhateeb A. Energy exchange of inserting eco-friendly bio phase change material into the vertical walls to make the buildings energy efficient. Journal of Building Engineering. 2022; 56:104777.

Alhasnawi BN, Jasim BH, Alhasnawi AN, Hussain FFK, Homod RZ, Hasan HA, et al. A novel efficient energy optimization in smart urban buildings based on optimal demand side management. Energy Strategy Reviews. 2024; 54:101461.

Anwar M, Rasul M, Khan M. Performance Analysis of rooftop greenery systems in Australian subtropical climate. Energy Reports. 2020; 6:50-6.

Ates F, Woo B-H, Jang C, Kim HG. Enhancing cementitious composites with PCM-impregnated cork granules for sustainable and energy-efficient building elements. Construction and Building Materials. 2024; 416:135071.

Brambilla A, Sangiorgio A. Mould growth in energy efficient buildings: Causes, health implications and strategies to mitigate the risk. Renewable and Sustainable Energy Reviews. 2020; 132:110093.

Bui D-K, Nguyen TN, Ghazlan A, Ngo TD. Biomimetic adaptive electrochromic windows for enhancing building energy efficiency. Applied Energy. 2021; 300:117341.

Buratti C, Moretti E, Belloni E, Zinzi M. Experimental and numerical energy assessment of a monolithic aerogel glazing unit for building applications. Applied Sciences. 2019;9(24):5473.

Carlander J, Thollander P. Drivers for implementation of energy-efficient technologies in building construction projects—Results from a Swedish case study. Resources, Environment and Sustainability. 2022; 10:100078.

Chen X, Abualdenien J, Singh MM, Borrmann A, Geyer P. Introducing causal inference in the energy-efficient building design process. Energy and Buildings. 2022; 277:112583.

Cuce E, Cuce PM, Alvur E, Yilmaz YN, Saboor S, Ustabas I, et al. Experimental performance assessment of a novel insulation plaster as an energy-efficient retrofit solution for external walls: A key building material towards low/zero carbon buildings. Case Studies in Thermal Engineering. 2023; 49:103350.

Cüce APM, GÜÇLÜ T, BEŞİR AB, Erdem C. Enerji Verimli Binalar İçin Sürdürülebilir Ve Çevre Dostu Pencere Ve Cam Teknolojileri: Son Gelişmeler Ve Uygulamalar. Uludağ Üniversitesi Mühendislik Fakültesi Dergisi. 2019;24(3):503-22.

Çimen S. Investigation of The Availability of Vermiculite In Thermal Insulation Technologies. Sürdürülebilir Mühendislik Uygulamaları ve Teknolojik Gelişmeler Dergisi. 2019;2(2):87-93.

Earth g, cartographer selcuk university teknology faculty, Konya, Turkey. Konya2022.

Esen S. Enerji etkin bina tasarım modeli: yüksek lisans tez, Eğitim Enstitüsü; 2019.

Excel SGb. The Graph gemneration by excel program based on simulation data. 2020 ed2022.

Fabbri K, Pretelli M, Bonora A. The study of historical indoor microclimate (HIM) to contribute towards heritage buildings preservation. Heritage. 2019;2(3):2287-97.

Geçimli M. Tasarım Sürecinin Deneyimlenmesinde Oyun ve Oyun-Tabanlı Uygulamalar. Mimarlık Planlama ve Tasarım Alanında Araştırma ve Değerlendirmeler- I: Gece Kitaplığı; 2020 2021. 21-42 p.

Issa RR, Suermann PC, Olbina S, editors. Use of building information models in simulations. Proceedings of the 2009 Winter Simulation Conference (WSC); 2009: IEEE.

Jankovic A, Goia F. Characterization of a naturally ventilated double-skin facade through the design of experiments (DOE) methodology in a controlled environment. Energy and Buildings. 2022; 263:112024.

Kishore P, Selvam N, Didwania S, Augenbroe G. Understanding BIPV performance with respect to WWR for energy efficient buildings. Energy Reports. 2022; 8:1073-83.

Koç SG. Sıcak-nemli iklim bölgelerinde gölgeleme elemanı kullanımının bina enerji performansına etkisinin incelenmesi: Fen Bilimleri Enstitüsü; 2019.

Koyun T, Ersin K. Bir Binanın Değişken Cam ve Dış Duvar Tiplerine Göre Pencere/Duvar Alanı Oranlarının Bina Isı Kayıplarına Etkisi. Mühendis ve Makina. 2017;58(688):1-14.

Liu MM, Mi B. Life cycle cost analysis of energy-efficient buildings subjected to earthquakes. Energy and buildings. 2017; 154:581-9.

Li H, Wang S. Coordinated optimal design of zero/low energy buildings and their energy systems based on multi-stage design optimization. Energy. 2019; 189:116202.

Li Z, Chow DH, Yao J, Zheng X, Zhao W. The effectiveness of adding horizontal greening and vertical greening to courtyard areas of existing buildings in the hot summer cold winter region of China: A case study for Ningbo. Energy and Buildings. 2019; 196:227-39.

Long LD. An AI-driven model for predicting and optimizing energy-efficient building envelopes. Alexandria Engineering Journal. 2023; 79:480-501.

Müller TM, Sachs M, Breuer JH, Pelz PF. Planning of distributed ventilation systems for energy-efficient buildings by discrete optimisation. Journal of Building Engineering. 2023; 68:106205.

Muslim SA, Hachem-Vermette C. Towards the development of energy sharing methodology between different buildings for high efficient neighborhood design. Energy Conversion and Management. 2023; 283:116901.

Nazari S, MirzaMohammadi PK, Sajadi B, Ha PP, Talatahari S, Sareh P. Designing energy-efficient and visually-thermally comfortable shading systems for office buildings in a cooling-dominant climate. Energy Reports. 2023; 10:3863-81.

Reddy VJ, Ghazali MF, Kumarasamy S. Advancements in phase change materials for energy-efficient building construction: A comprehensive review. Journal of Energy Storage. 2024; 81:110494.

Rivera-Gómez C, Diz-Mellado E, Galán-Marín C, López-Cabeza V. Tempering potential-based evaluation of the courtyard microclimate as a combined function of aspect ratio and outdoor temperature. Sustainable Cities and Society. 2019; 51:101740.

Saffar SWA. Yaklaşık Sıfır Enerjili Bir Bina tasarımı için enerji performansı modellemesi ve simülasyonu: Necmettin Erbakan Üniversitesi Fen Bilimleri Enstitüsü; 2022.

Self Di. Drawing of Selcuk university teknology faculty by autodesk revit 2020. Auto desk Student version. [Drawing an simulation]. In press 2022.

Soliman A, editor Minimizing Energy Consumption of Educational Buildings by Testing Alternatives of Green Envelopes in Alexandria. International Conference on Green Urbanism; 2022: Springer.

Soorige D, Karunasena G, Kulatunga U, Mahmood MN, De Silva L. An energy culture maturity conceptual framework on adopting energy-efficient technology innovations in buildings. Journal of Open Innovation: Technology, Market, and Complexity. 2022;8(2):60.

Stine DJ. Autodesk Revit for Architecture Certified User Exam Preparation (Revit 2020 Edition): SDC Publications; 2019.

Tulukcu DA. Örnek Bir Binanın Isıl ve Çevresel Performansının Autodesk Revit Simülasyon Programı ile Analizi. Avrupa Bilim ve Teknoloji Dergisi. 2021(23):197-206.

Wasim M, Wang K, Yuan Z, Jin M, Abadel A, Nehdi ML. An optimized energy efficient design of a light gauge steel building. Case Studies in Construction Materials. 2023;19:e02398.

Yazgan SÖ, Koçak Soylu S. Otellerde enerji verimliliğini iyileştirmeye yönelik çeşitli yaklaşımların tasarruf oranlarına etkisinin karşılaştırılması: Antalya örneği. 2022.

Yori R, Kim M, Kirby L. Mastering Autodesk Revit 2020: John Wiley & Sons; 2019.

Zhou S, Razaqpur AG. Efficient heating of buildings by passive solar energy utilizing an innovative dynamic building envelope incorporating phase change material. Renewable Energy. 2022; 197:305-19.

ELECTRICAL ENGINEERING AND ENERGY

OPEN ACCESS

A Comparison of SMD and Through-Hole Components on Conducted Noise Emission

Deniz Metin[1], Ersoy Kelebekler[2]

[1] Dept. of Cosmetic Inspection, Turkish Medicines and Medical Devices Agency, Ankara, Türkiye
[2] Dept. of Biomedical Engineering, Kocaeli University, Kocaeli, Türkiye

Submitted: 2 January 2026
Accepted : 26 January 2026
Online First: 29 January 2026

Corresponding author
Ersoy Kelebekler,
ersoy@kocaeli.edu.tr

DOI:10.64470/elene.2026.24

Abstract: Switched-mode DC-DC converter circuits create quite challenging electromagnetic compatibility problems. Additionally, the design preferences directly affect the EMC performance of the circuits. The study focuses on the conducted noise emissions of the same Boost converter circuits constructed with two different types of assembly technologies, Through-Hole and SMD. For this purpose, two Boost converter circuits using the same integrated circuit, LT1070, were designed by using Through-hole and SMD assembly technologies. The conducted emission measurements were taken according to Class B of EN 55032 standard requiring measuring the noise emission in the frequency range between 150 KHz and 30 MHz. The results obtained from measurements show that the emission amplitude at 160 kHz for Boost converter constructed with Through-Hole components is higher than the standard requirement while the converter constructed with SMD components meets the standard at the same frequency. The conducted emission amplitudes of both Boost converter at 200 KHz and 240 KHz cannot meet the requirements of the standard, but the peak values for SMD-based circuit are higher than the emission amplitudes of Boost converter constructed with Through-Hole components at the same frequencies. Because of failing both circuits on the tests of En 55032 standard, a low-pass π type filter was designed. After adding the π filter to the Boost converter circuits, the conducted emission values have met the standard requirements in all frequency range. The efficiency of the designed filter completely suppresses the noise all frequency range of EN 55032, from 150 KHz to 30 MHz.

Keywords Electromagnetic Compatibility (EMC), Electromagnetic Interference (EMI), EMI Filter Design, DC–DC Converters.

1. Introduction

Electromagnetic compatibility (EMC) is crucial for the smooth operation of electronic devices. While operating, electronic and electrical devices generate electromagnetic interferences (EMI) disturbing other devices. EMC refers to the ability of these devices to operate smoothly without being affected by EMI(Ott, 2009). There are two types of EMI: conducted electromagnetic noise and radiated electromagnetic noise (Paul, 2006). Conducted electromagnetic noise refers to the type of noise that devices transmit to other devices and the shared power grid via electrical cables or interconnects. Radiated electromagnetic noise is the type of electromagnetic noise that propagates via radio waves. From aviation to automotive or industrial products and home electronics, all electronic devices must meet EMC requirements. However, the EMC standards and limits of these standards vary depending on the usage area in which the relevant electronic devices are used. Electronic systems are tested not only on a circuit level but also as a final product consisting of multiple electronic circuits (Weston, 2017).

Electronic systems can operate at different voltage and power values. Therefore, they often need power converters. Therefore, DC-DC converters are indispensable components of electronic systems. DC-DC converter topologies require a switching element in terms of their operating principles. The ability of the switching element to drive the current at the desired speed and magnitude is the main factor that determines the efficiency of the converter. However, the fact that the switching element drives the current intermittently over time is the main cause of especially conducted EMI. In parallel with the developments in the field of power electronics, the switching frequencies of driver elements have increased recently. Additionally, EMC problems have increased in parallel with the switching frequency. EMC problems in DC-DC converters have been investigated and distortions in the power signal have been investigated in various studies in simulation environments or by implementing circuits (Karagöl, 2015; Yalçın, 2015; Roberts and Lametschwandtner, 2023; Tyagi et al. 2017). In this study, the Boost converter circuit using LT1070 integrated circuit as the switching element was designed and its conducted emission characteristics were investigated.

In the study, BOOST converter circuit was implemented by using Through-Hole and SMD (Surface Mount Device) components. The Conducted interferences of the BOOST converters fabricated with two different assembly technologies were tested individually because of observing how the conducted emission performances differed according to assembly technology and design. So, the aim of the study is to emerge the assembly technology and design effect on conducted emission performance. The measurements of the conducted interferences were performed in FARBA Automotive's Electromagnetic laboratories. The crucial component in the EMC test measurements is Line Impedance Stabilization Network (LISN) used to filter the source signal and match the line impedance to 50 Ω. The interference measurements are taken separately from both sides of LISN as LISN+(positive) and LISN-(negative). As mentioned above, the EMC standards vary depending on usage area of the electronic device. In the study, the conducted emission measurements were taken according to Class B of EN 55032 standard describing the limit of residential, commercial and light industrial electronic devices (EN 55032). The study investigates the effect of the SMD and Through-Hole components on the conducted noise values by presenting correspondingly conducted EMI measurements for both structures.

According to the measurement results, the conducted emissions of the BOOST circuit implemented with SMD components and Through-Hole components did not meet the conducted noise limits identified by the EN 55032 standard. Hence, a low-pass π (pi) type filter was designed and implemented to reduce the conducted noises below the limit values specified by the standard. The frequency interval of the EN 55032 standard for the conducted emission is between 150 kHz and 30 MHz. The filter was designed to subpress the noise within the frequency range specified by the standard. For this reason, no effort was made to filter noise values below 150 kHz and above 30 MHz. The measurements for filter added BOOST converter circuits with SMD components were repeated in the laboratories and the efficiency of designed filter was presented. The conducted emission values of the BOOST converter with SMD components reduced below the limit values specified by the EN 55032 standard after adding the designed filter. In the next section, the circuit schematic of the BOOST converter is given, and the operating principles of the circuit are explained. In the third section, the BOOST circuits constructed with SMD and Through-Hole assembly technologies, conducted emission results obtained from laboratories measurements for both circuits are presented. The study ends with conclusions.

2. BOOST Converter

The operating principle of the BOOST circuit topology is to increase the DC input voltage to higher DC output voltage than the input. Figure 1 shows the circuit diagram of the BOOST circuit topology.

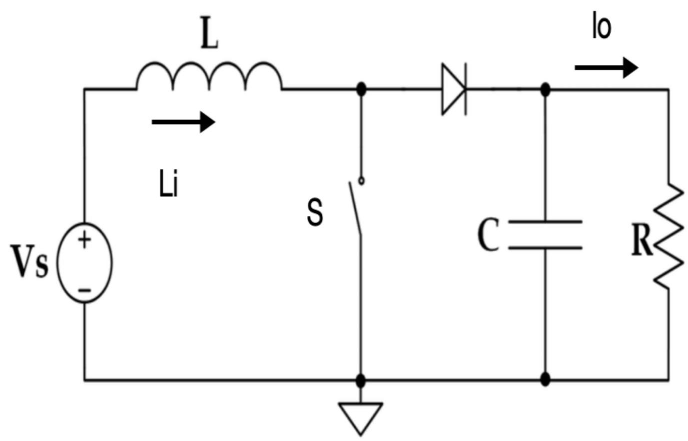

Figure 1 BOOST converter

The BOOST converter circuit was designed based on the datasheet published by Linear Technology, the manufacturer of the LT1070 integrated circuit. The circuit was implemented in accordance with the datasheet. As shown in Figure 1, there is a coil in the input of boost converter circuits. When the switching element is closed, energy is stored in the coil. When the switching element is open, the accumulated energy in the coil and the energy on the source side feed the capacitor and load on the output side of the circuit. During this time, the capacitor charges. When the switch is closed again, a stable output voltage is achieved. As the switch is opened and closed, fluctuations occur in the current signal. These fluctuations in the current signal produce EMI and cause EMC problems. Current fluctuations are the main source of conducted noise emissions. In addition to EMI caused by switching elements in the DC-DC converter topologies, the types of materials used in electrical circuits can also affect magnitude and phase electromagnetic interference in the frequency spectrum. In the study, it is aimed to compare effect assembly technologies on conducted emissions.

The electromagnetic noise nature is too complex. There are two kinds of electromagnetic noises, common mode noise and differential mode noise. Common mode noise propagates in the same direction on both signal lines. The common mode noise is measured between signal line (positive or negative lines) and ground line. Common mode chokes and Y-type capacitors are used to filter the common mode noise component. On the other hand, differential mode noise is the noise propagating in opposite directions on positive line and negative line. Differential mode inductors and X-type capacitors are used to filter the differential mode noise(Su et al. 2019; Felic, 2011). Each one of these noise components is measured by using different measurement techniques. In the study, total noise of implemented BOOST converter was measured according to EN 55032 standard without considering which component, differential or common, is dominant.

In this study, A BOOST converter circuit is designed by using two different assembly technologies. One of the electrical circuits was designed and implemented with two different assembly technologies, SMD and Through-Hole. The conducted noise values of the circuits designed with the two different assembly technologies were measured separately because of determining the impact of material type on the conducted emission taken according to EN 55032 standard. The measurements were taken in a real laboratory environment in FARBA Automotive Corporation.

3. Measurements and Discussions

Fluctuations in voltage signals and noise emissions on signal or ground line occur because of the discontinuous current caused by the switching element used in DC-DC converters. These fluctuations trigger distortions in the DC source signal or the mains frequency of grid signal. As a result, these distortions cause conducted or radiated electromagnetic noises. Distortions in the mains signal may occur not only because of conducted noise but also due to radiated noise. Conducted and radiated electromagnetic noise limit values are also specified by standards. In this study, conducted emission characteristic for commercial BOOST converter was investigated and a filter design to suppress the conducted noise obtained end of the measurement was performed.

In general, there are four basic types and classifications of filters: low-pass filters, high-pass filters, band-pass filters, and band-stop filters(Tyagi et al.2017; Tarateeraseth, 2011; Tarateeraseth, 2012; Johannesson and Fransson, 2008). In this study, a low-pass pi-type filter was designed to filter the conducted noise of the converter. The BOOST converter circuit was designed as specified in the datasheet. Figure 2 shows the BOOST converter with the LT1070 integrated circuit schematic given in the datasheet document published by Linear Technology company.

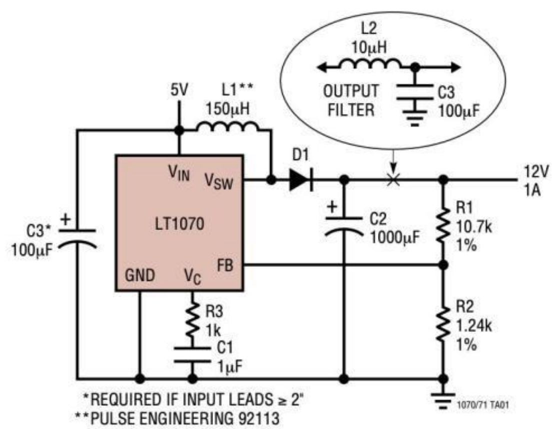

Figure 2 Application circuit in datasheet of LT1070

The LT1070 integrated circuit can be used in various DC-DC converter topologies. The BOOST topology converting 5V input voltage to 12V output voltage was used in this study. In the circuit, the LT1070 integrated circuit receives feedback from the FB pin and adjusts the output voltage through ratio of resistors R1 and R2. The top layer and bottom layer of the BOOST converter circuit implemented with through-hole materials and SMD materials is given in Figure 3 and Figure 4, respectively.

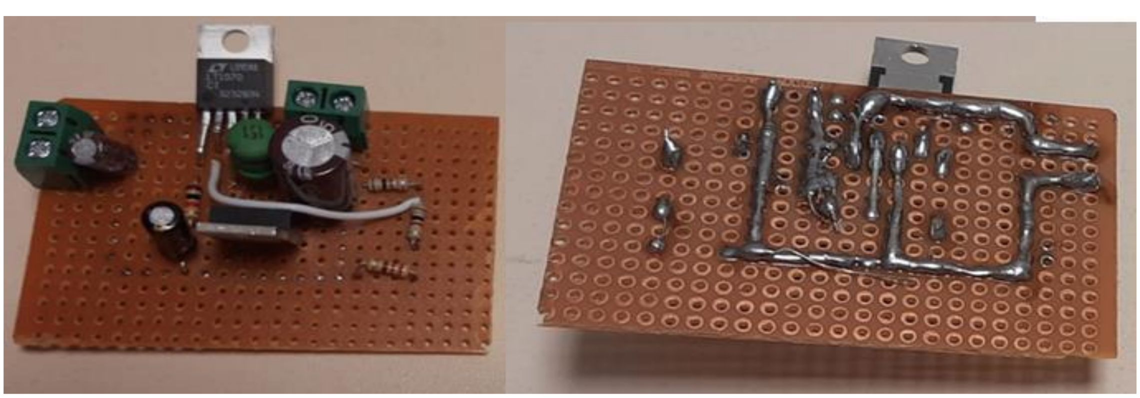

Figure 3 Top and bottom layer of the BOOST converter implemented with through-hole materials

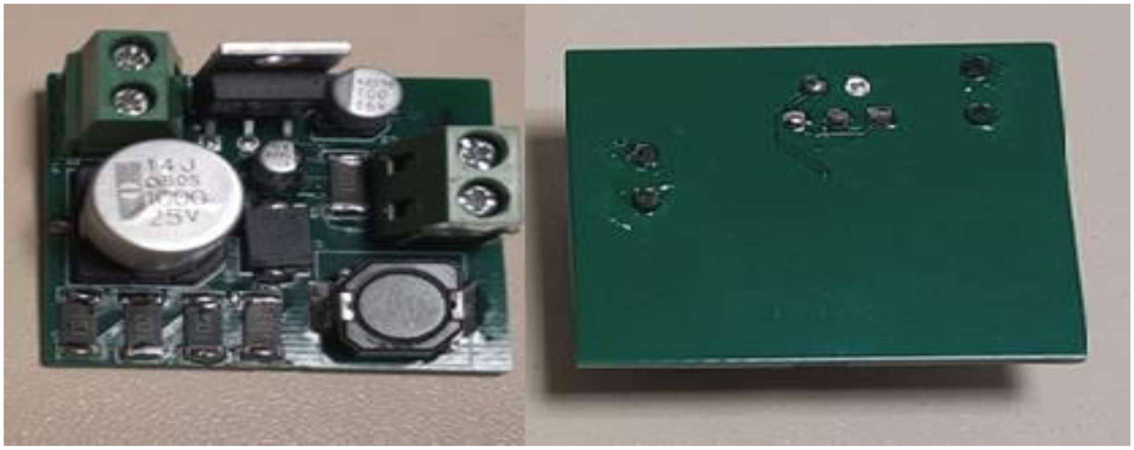

Figure 4 Top and bottom layer of the BOOST converter implemented with SMD materials

The component values of both BOOST converter circuits are identical. The only difference between the two identical circuits is their different assembly technologies. Because of different assembly technologies, the positions of the components on the circuits are different, as well. This study investigates the effect of assembly technologies differences on conducted emission values. The measurement graph of the conducted noise received by the LISN+ and LISN- for the BOOST circuit designed with SMD components is given in Figure 5. The conducted emission limits of the graph are determined according to Class B of the EN 55032 standard.

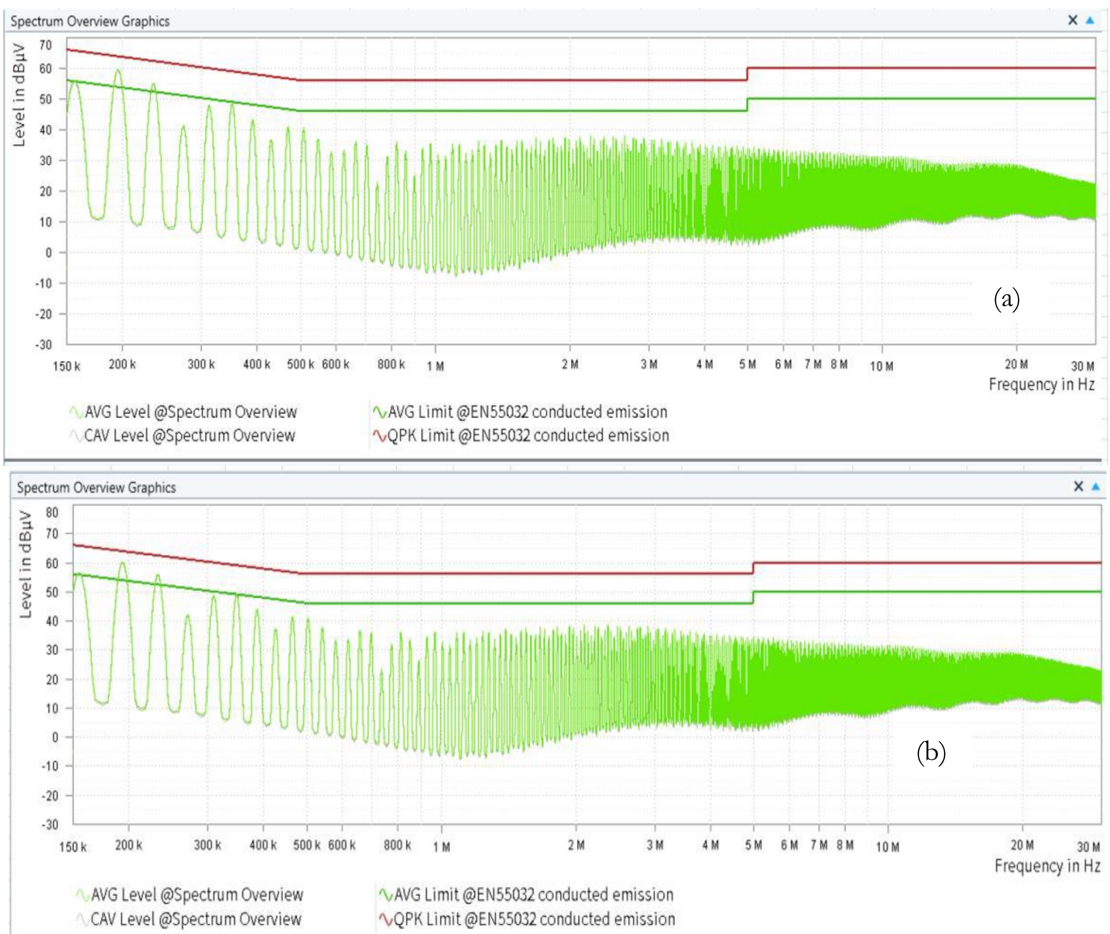

Figure 5 Conducted emission of the BOOST with SMD taken (a)LISN+ and (b)LISN-

As seen in the figures, the noise values of the conducted emission are similar on both side of the LISN. The noise values for conducted emission of the BOOST circuit implemented with SMD components exceed the noise limit specified by the EN 55032 standard around 200 KHz and 240 KHz. The study aims to compare conducted emission characteristics of BOOST converters implemented with two different assembly technologies, SMD and through-hole. The BOOST converter implemented with through-hole components was studied as second application. The conducted noise values of the BOOST circuit constructed with through-hole components were measured and presented in Figure 6.

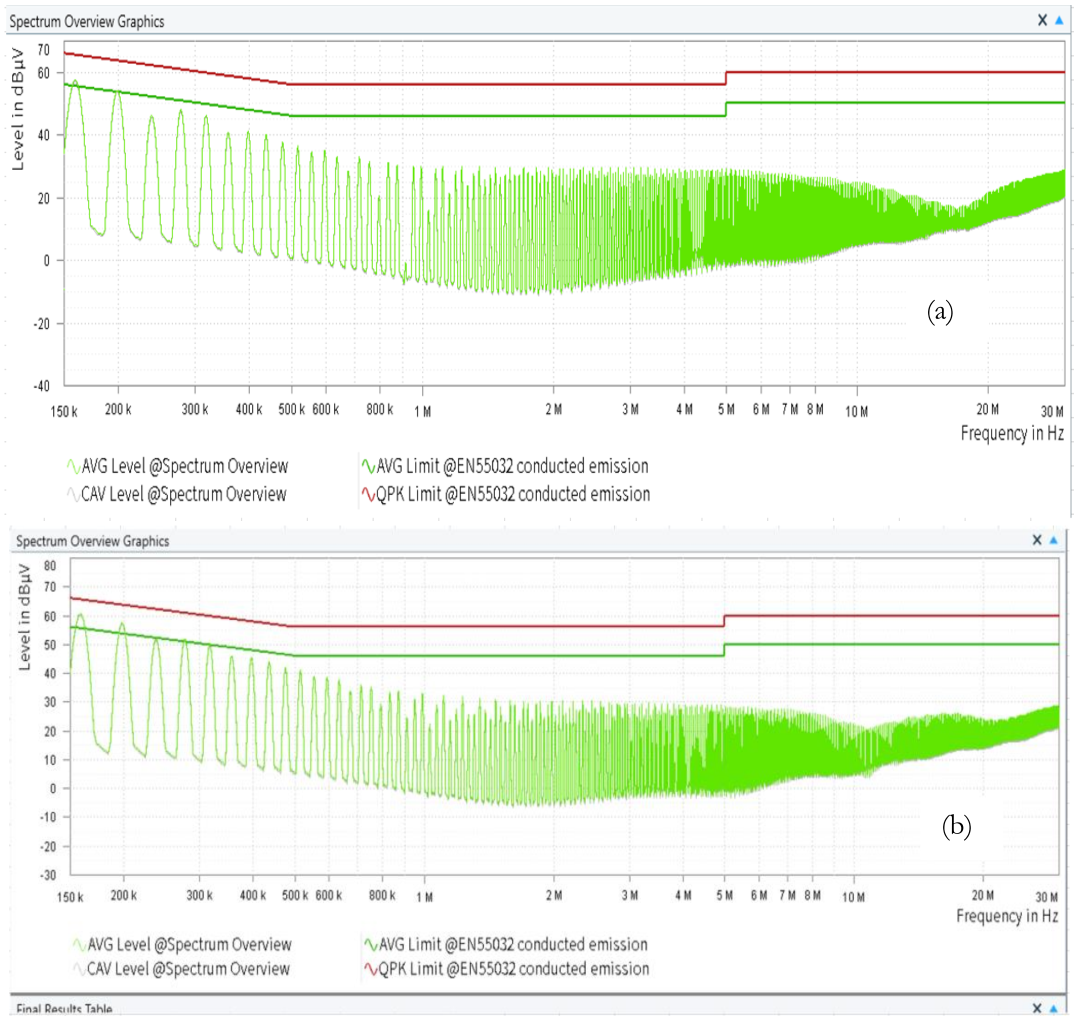

Figure 6 Conducted emission of the BOOST with through-hole components taken (a)LISN+ and (b) LISN-

As seen in the figure (a), noise values exceed the limits of standard in the vicinity of 160 KHz. The noise values taken LISN- for conducted emission of the BOOST circuit implemented with through-hole components exceed the noise limit specified by the EN 55032 standard around 160 KHz and 200 KHz. If the results obtained from both materials are analyzed comparatively, emission characteristics are similar between the LISN positive and negative side for same assembly technologies. On the other hand, the frequencies where the emission values are exceeding the limits shift from 160 KHz and 200 KHz for the through-hole component-based circuit to 200 KHz and 240 KHz for the SMD component-based circuit. As presented above, the conducted emission values of BOOST converter circuits constructed both type assembly technologies, Through-Hole and SMD, cannot meet the limits specified by the EN 55032 standard for the noise values received from the LISN+ and LISN- sides. However, the conducted noise values of the circuit constructed with Through-Hole components are considerably higher at a frequency of approximately 160 kHz than the noise values of the BOOST circuit constructed with SMD components at the same frequency. In both cases, the transmitted noise values exceed the limit values specified by the EN 55032 standard. To reduce the conducted noise values below the limit values specified by the standard, a filter design is required. There are different filter topologies such as low pass, high pass, band pass and band stop. The number of inductance and capacitance determines the order of the filter, and the location of the components defines input and output impedance of the filter. Additionally, the attenuation characteristic of a filter is presented insertion loss in decibels (dB). Insertion loss corresponds to the reduction in load voltage at a particular frequency due to the insertion of the filter into the circuit (Guler, 2025). In this study, a third order low-pass π (pi) type filter, including two capacitors and a inductor, was designed to suppress the conducted emission noise. The cutoff frequency was chosen as 40 kHz because the switching frequency of the LT1070 integrated circuit used in the BOOST circuit is 40 KHz and the noises exceeding the limits are observed the harmonics of the switching frequency. The formulas used to calculate the values of the elements for the third order low-pass π filter circuit are given in Equation (1) and Equation (2) (Tarateeraseth, 2011; Johannesson and Fransson, 2008; Chen, 1991; Yildiz, 2020).

$$L = \frac{R}{2\pi f_c} \tag{1}$$

$$R = \frac{1}{2\pi f_c C} \tag{2}$$

where, L is the inductance value of the π filter and C is the capacitance value of the filter. f_C is the cutoff frequency of the filter and R is the load resistance. Load resistance equals to 100**Ω** because it was used as load in all of measurements. For 100 ohms load resistance, the inductor value was calculated approximately 397 μH and the capacitor value was obtained 39 nF. However, it is hard or impossible to find the exact value of these components on the market. So closed values components were obtained as 470 μH for the inductor and 47 nF for the capacitor, and the circuit design was assembled with these values. The insertion loss, input and output impedance obtained using Würth Elektronik online software are presented for $C_1 = C_2 = 47\text{nF}$ and L=470 μH in Figure 7 (Würth Elektronik, 2026).

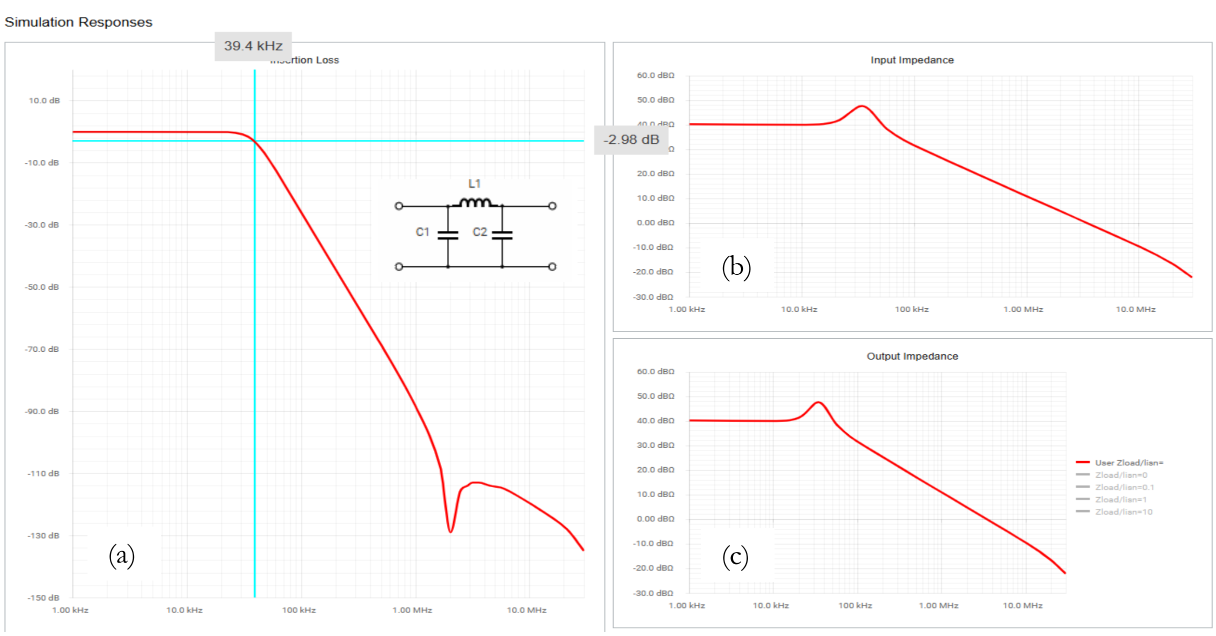

Figure 7 The simulation result obtained from Würth online software; (a)insertion loss, (b) input impedance, (c)output impedance

As seen in the figure, the insertion loss is about -3 dB around 40 KHz. Additionally, the filter shows high impedance in the vicinity of 40 KHz. The impedance characteristic of the designed filter obtained experimentally by using GW-Instek LCR-8110G impedance analyzer is presented in figure 8.

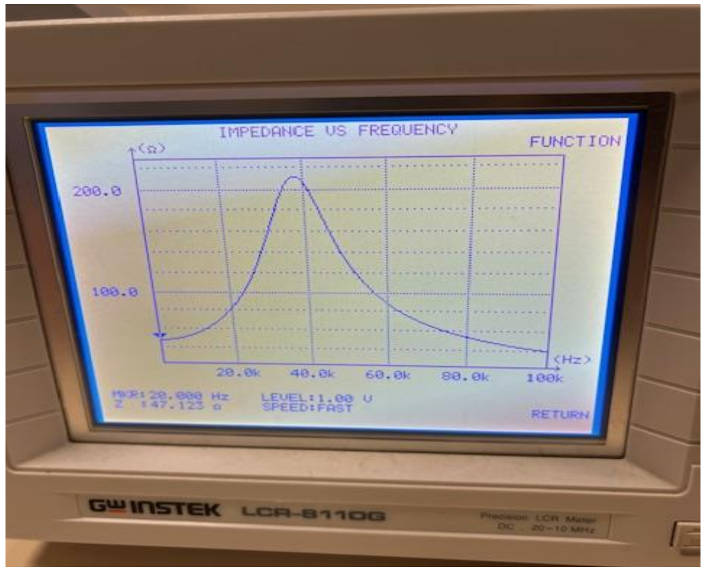

Figure 8 The impedance characteristic of the designed filter obtained from GW-Instek LCR-8110G

The experimental results are compatible with the results obtained from Würth Elektronik online software. In the next figure, a picture taken from measurement in the laboratory is given for low-pass π filter added BOOST converter.

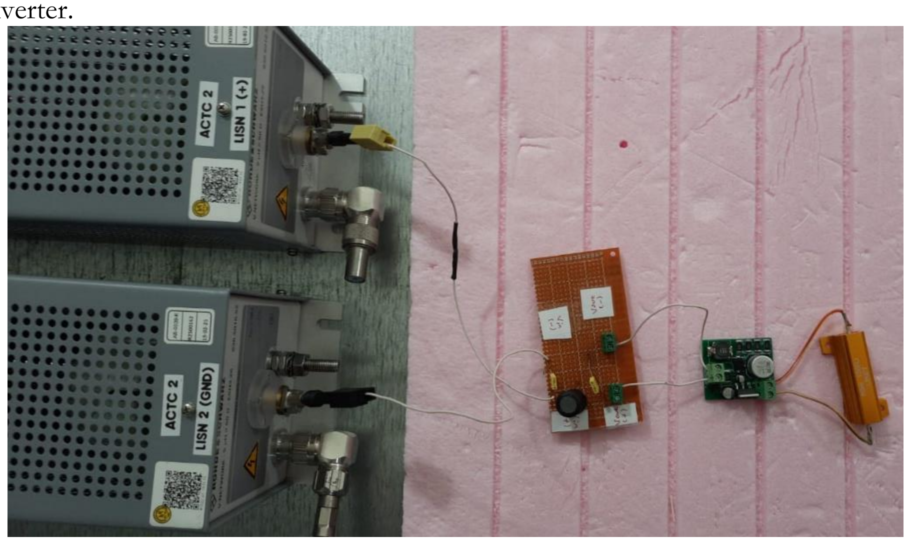

Figure 9 The measurement system for low-pass π filter added BOOST converter

The conducted emission values of the Boost converters constructed with Through-Hole and SMD components decreased below the limits of the EN 55032 standard by adding the low-pass π filter. The designed filter reduces the conducted emission values more than 30 dB at most of the frequency range. Figure 10 shows the conducted emission values of Boost converter with SMD components received form the LISN+ and LISN- after adding π type low-pass filter to the BOOST converter. The results obtained for Boost converter with π type filter show the conducted emission values fall below the limit values specified by the EN 55032 standard after adding the filter to the circuits constructed with Through-Hole or SMD components. It means the efficiency of the designed filter is greatly well for the frequency range of EN 55032, 150 KHz to 30 MHz.

Figure 10 Conducted noise of Boost converter with SMD material, taken from (a) LISN+ and (b) LISN-

4. Conclusions

The aim of this study is to compare material assembly technologies, through-hole and SMD, on conducted noise emission of a Boost converter. For this purpose, a Boost converter circuit was designed using the LT1070 integrated circuit. The Boost converter circuit was implemented with both SMD and through-hole components. In the study, the conducted emission measurements were taken according to Class B of EN 55032 standard. The standard describes the limit of residential, commercial and light industrial electronic devices. The standard requires to measure the noise emission in the frequency range between 150 KHz and 30 MHz. The conducted noise values of Boost converters constructed with two different assembly technologies were measured separately from the LISN+ and LISN- as required by EN 55032. The emission peaks reveal at the switching frequency harmonics as expected but the amplitudes of the peaks change depending on the circuit assembly technologies, SMD or Through-Hole. The results obtained from the Boost converter constructed with SMD components and Through-Hole components that the conducted emission amplitudes of SMD component-based Boost converter at 200 KHz and 240 KHz cannot meet the requirements of the standard, and they are higher than the emission amplitudes of Through-Hole component-based Boost constructed at the same frequencies. However, the emission amplitude at 160 kHz for Boost converter constructed with Through-Hole components is higher than the standard requirement while the converter constructed with SMD components meets the standard at the same frequency. The EMC emission characteristic of any system depends on numerous parameters such as trace loops, parasitic effects related to inductive or capacitive coupling, grounding, shielding, soldering techniques, PCB materials, assembly technologies, etc. The study aims only to compare the effect of the assembly techniques, through-hole and SMD, on the conducted emission. The results obtained from measurements show there is no dominant difference depending on assembly technology on conducted electromagnetic emission performance.

In both circuits, the conducted emission peaks are at multiples of 40 kHz, the operating frequency of the LT1070 integrated circuit. Both circuits, whether they are constructed with SMD or Through-hole components, cannot meet the requirements of En 55032 standard. Because of this cause, a low-pass π type filter was designed and added to the Boost converter circuits. The insertion loss, input impedance and output impedance of the designed filter obtained from Würth Elektronik online software, and the impedance characteristic obtained from impedance analyzer were included in the study. After adding the π filter to the Boost converter, the conducted emission values were taken again. The conducted emission values of the filter-added circuits can meet the standard requirements in all frequency range. The conducted emission results obtained from the SMD component-based Boost converter with filter has been given in the study to show performance of the designed filter. As presented in the previous section, the efficiency of the designed filter is greatly well for the frequency range of EN 55032, 150 KHz to 30 MHz. It can completely suppress the noise all frequency range of the standard.

Declaration of Ethical Standards

As the authors of this study, we declare that he complies with all ethical standards.

Credit Authorship Contribution Statement

D.Metin: Investigation, Resources, Validation, Formal analysis, Writing, Visualization,
E.Kelebekler: Methodology, Validation, Writing, Review & Editing, Supervision, Funding acquisition.

Declaration of Competing Interest

The authors declared that they have no conflict of interest.

Funding / Acknowledgements

The authors thank FARBA Automotive Corporation for supporting EMC tests.

Data Availability

No datasets were generated or analyzed during the current study.

References

Chen, W.-K. (1991). Passive and Active Filters, Theory and Implementations. Wiley.

Johannesson, G. and Fransson, N. (2008). EMI measurements and modeling of a DC-DC Buck converter, *Chalmers University*.

EN 55032, https://intweb.tse.org.tr/Standard/Standard/Standard.aspx,

Felic, G. K. (2011). Heatsink EMI Effects in Power Electronic Systems in Electromagnetic Interference Issues in Power Electronics and Power Systems, *Bentham Science Publishers*.

Karagöl, H. (2015). DA-DA Dönüştürücülerde Elektromanyetik Uyumluluk Sorunlari ve Çözüm Önerileri, *Gazi Üniversitesi*, Ankara.

Guler, C. and Kelebekler, E. (2025). Development of a GUI for EMI Filter Insertion Loss and Transfer Function Modeling, *8. International Conferences on Science and Technology*, Budapest, 301-308.

Ott, H. W. (2009). Electromagnetic Compatibility Engineering. *John Wiley & Sons*.

Paul, C. R. (2006). Introduction to Electromagnetic Compatibility, *John Wiley & Sons*.

Roberts, S. and Lametschwandtner, J. (2023). EMC Book Of Knowledge Practical tips for the User, *RECOM,* 2023.

Su, D., Xie, S., Dai, F., Liu, Y. and Jia, Y. (2019). Theory and Methods of Quantification Design on System-Level Electromagnetic Compatibility. *Springer*,

Tarateeraseth, V. (2011). EMI Filter Design Part I: Conducted EMI Generation Mechanism, *IEEE Magazine*, pp. 44–50.

Tarateeraseth, V. (2012). EMI Filter Design Part III: Selection of Filter Topology for Optimal Performance, *IEEE Electromagn Compat Mag*, 1(2), 42-49.

Tyagi, A., Venkatesh, S. K. and Singh, A. (2017). Design & Implementation of a practical EMI filter for high frequency-high power dc-dc converter according to MIL-STD-461E, *International Research Journal of Engineering and Technology (IRJET),* 4(3), 2585-2591.

Weston, D.A. (2017). Electromagnetic Compatibility Methods, Analysis, Circuits, and Measurement. *CRC Press.*

Würth Electronik, (2026). https://redexpert.we-online.com/we-redexpert/en/#/emifd-embedded.

Yalçın, S. (2015). Anahtarlamalı Güç Kaynaklarında Elektromanyetik Girişimin İncelenmesi Ve Elektromanyetik Girişim Süzgeç Tasarımı, Akdeniz Üniversitesi.

Yildiz, A. B. (2020) Elektrik Devreleri - II. Umuttepe Yayınları.

ELECTRICAL ENGINEERING AND ENERGY

OPEN ACCESS

Assessment of Performance of 80W Monocrystalline Photovoltaic (PV) Module in Abuja FCT

Samson Dauda Yusuf[1], Arinze Ogu Nduka[2], and Ibrahim Umar[1]

[1] Dept. of Physics, Faculty of Natural and Applied Sciences, Nasarawa State University, Keffi, Nigeria
[2] National Agency for Science and Engineering Infrastructure (NASENI) Solar Energy Ltd. Karshi, Nigeria

Submitted: 02 January 2026
Accepted : 30 January 2026
Online First: 03 February 2026

Corresponding author
Samson Dauda Yusuf,
samsonyusufu@yahoo.com

DOI:10.64470/elene.2026.25

Abstract: Solar PV modules are rated by manufacturers under Standard Test Conditions (STCs), which often differ from real outdoor operating conditions. Therefore, evaluating field performance is essential for accurate module selection and power prediction. In this study, a one-year performance assessment of an 80 W solar PV module manufactured by NSENI Solar Energy Limited was conducted in Abuja-FCT, Nigeria, using real-time measurements and simulation. Key electrical parameters (Pmax, VMP, and IMP), solar radiation, and module temperature were continuously monitored using calibrated instruments. In parallel, empirically based PV models incorporating manufacturer datasheet values and local climatic data were used for simulation.

The results show significant deviations between STC ratings and outdoor performance. At certain periods, the module voltage and efficiency dropped below 12 V and 11%, compared to the rated 17.35 V and 18%. While VMP and efficiency decreased at high solar radiation, Pmax, IMP, and module temperature increased, with opposite trends observed under lower radiation levels. A strong agreement between measured and simulated maximum power outputs was obtained, with a correlation coefficient of 0.98 and an average error of about 5%. These findings confirm the reliability of the applied PV models and demonstrate that the developed testbed can be used as a practical PV module performance validation facility suitable for replication across Nigeria.

Keywords Solar PV module, STC, Outdoor condition, Maximum Power, Module Temperature.

1. Introduction

In order to reduce global warming, the adoption of renewable energy is becoming more popular, with solar photovoltaic (PV) power systems most favoured because they are easier, consume less time, and are less complex to deploy for electricity generation (IEA, 2022; Iheanetu, 2022). In fact, IEA (2022) stated that the estimated solar PV electricity generation from 2019 to 2020 increased to 23% and has contributed a record high of 156 TWh, and their prediction is that it will reach 7000 TWh by 2050.

Solar PV technology converts solar energy directly to electricity using PV cells (connected together to form a solar PV module), and the PV modules are exposed to capture the energy from the sun (solar energy) by installing them outdoors. The generation of electricity using a solar PV power system is highly dependent on uncontrolled weather and environmental conditions, such as PV module temperature, solar radiation, wind speed, and other climatic parameters (Iheanetu, 2022). Due to the variability of these climatic factors, the output power of a solar PV system dynamically changes with time and season (Geravandi and Moradi, 2022). The use of battery backup is currently adopted to mitigate the challenges encountered due to the variable weather conditions. This is because the battery backup system makes sure that the desired level of power supply, irrespective of the actual weather condition, is available. However, battery backup increases cost. Therefore, there is a need for accurate yield prediction with respect to operating climatic conditions.

The inability to predict PV module/array electrical outputs accurately significantly affects the stability, dependability, and scheduling of the power system operation and its economic benefit (Woyte et al., 2006; Strzalka et al., 2012; Das et al., 2019). According to Bücher (1997), the manufacturers of solar PV modules rate them at controlled conditions called Standard Test Conditions (STCs) of 25°C Module Temperature (Tm) and 1000 W/m² Solar Radiation. Unfortunately, the manufacturer's ratings are used by solar power system designers to make decisions on the choice of solar PV module (solar panel) and array design. However, Zhou et al. (2007) stated that the outdoor performance of PV modules is influenced majorly by ambient conditions such as solar radiation and location-based module temperature (Tm). Consequently, Iheanetu (2022) concluded that solar PV power forecasting or prediction provides a means by which a reliable estimate of the power from the solar PV modules/arrays is obtained after considering the existing weather conditions and system losses. These have led many researchers to carry out solar PV module performance assessments (Kurnik et al., 2011; Kozak et al., 2009; Buday, 2011; Meral & Dinçer, 2011; Abdelkader et al., 2010; Bahaidarah et al., 2015). Wahidullah, Safiullah, and Sayed (2024) evaluated and compared the energy output of mono-crystalline and poly-crystalline solar photovoltaic (PV) technologies under the same climatic conditions and concluded that mono-crystalline technology performed better.

Zhou et al. (2007) suggested that having reliable knowledge and understanding of the performance of a solar PV module under the actual climatic conditions (outdoor) is necessary for correct module selection criteria and accurate prediction of their energy performance. Liomnis *et al.* (2022), in their study comparing 10 module temperature estimation models, concluded that of King et al. (2004) is the most accurate.

Nduka and Mohamed (2018) simulated city-based PV-module temperature (Tm) in eight cities of Nigeria, using the empirical thermal model developed by King et al. (2004) to predict the expected voltage (V), power, and efficiency of a 100 W PV module. They discovered that the outdoor conditions are different from Standard Test Conditions (STCs), and cities with high Tm and solar radiation produced lower voltage and efficiencies and higher power. Osagie-Bolaji and Osadebamwen (2025) carried out a performance analysis of 250W monocrystalline and 250W polycrystalline photovoltaic (PV) modules under varying solar irradiance conditions in Nigeria and discovered that the monocrystalline module consistently outperformed the polycrystalline module under the same irradiance condition with a drop in efficiency at the highest irradiance for both of them. The climatic condition of Nigeria varies from location to location and season to season (Nduka and Mohamed, 2018). In this study, a performance assessment is being carried out on an 80W solar PV module produced by NSENI Solar Energy Limited through real-time measurements and simulation in Abuja-FCT, Nigeria, to ascertain the validity of some empirically based PV models in the prediction of solar module power yield.

2. Materials

The 80W Solar PV Module is the sample whose outdoor performance is being monitored. The Elejoy 400W Solar PV Panel Multimeter was the instrument used for real-time monitoring of the electrical output (maximum power, voltage at maximum power, and current at maximum power) of the 80W PV module; the

BGT-HJX-TFI Portable Pyranometer with Data Logger was used for real-time monitoring of the solar radiation of Karshi FCT; and the Temp U 07B Digital Temperature Data Logger was used for real-time monitoring of the module temperature of the 80W solar panel. The cables are used to connect the Solar Panel Multimeter and Temperature Data Logger to the 80W Solar Panel, the clips were used to clip cables, the metallic platform served as the bed upon which the solar PV module and the attached devices were installed/mounted, and the bolts and nuts were used to firmly fix the testbed and the devices. The materials and instruments that were used in this study are presented in Table 1.

Table 1 Materials and their specifications

Materials	Quantity	Specification
Solar PV Panel Multimeter	1	Elejoy 400W: Range 0-400W, 0-30V, 0-15A.
BGT-HJX-TFI Portable Pyranometer with Data Logger	1	Range 0-2500 W/m²
Temp U07B Digital Temperature Sensor with Data Logger	1	Range 0.1-1000°C
PV Module	1	Power: 80W, Voc = 20.15V, Isc = 5.44 A, Vmp =17.35V, Imp = 5.3A, Eff =18%. Temp. Coeff. of Pmax = -0.5629%/°C, Temp. Coeff. of Vpmax = -0.79914%/°C, FF = 0.78.
Flexible cable	5m	Silver plated, 6mm thick
Flexible cable	8m	Copper, 1.5mm thick
Metallic platform	1	2m high
Aluminum clips	1pck	6063-T6 aluminum alloy, 2 inch length, 1/4 inch holes.
Bolts and Nuts	8nos	Bolt & Nun-11

3. Methods

3.1 Study Location

Abuja FCT is the capital of Nigeria. It has 6 Area Councils, namely Abaji, Abuja Municipal (AMAC), Bwari, Gwagwalada, Kuje, and Kwali. Abuja is located just north of the confluence of the Niger River and the Benue River (FCTA, 2008). It is geographically located at the center of the country and is bordered in the west by Niger State, in the north by Kaduna State, in the northeast by Nasarawa State, and in the southwest by Kogi State. The FCT lies between latitudes 8.25 and 9.20 north of the equator and longitudes 6.45 and 7.39 east of the Greenwich Meridian (FCTA, 2008). It has a landmass of approximately 7.315 km², and it is situated within the savannah region with moderate climatic conditions (FCTA, 2008). Abuja has an average daily maximum temperature that is above 30°C or 86°F (FCTA, 2008). Abuja is located within the Guinea Savannah climatic zone of Nigeria, and it receives a global horizontal irradiation (GHI) of about 2.04 MWh/m²/year (232.88 W/m²) (Ohajianya, 2023). Abuja has an average monthly wind speed of 2.4m/s (Ani *et al.,* 2012). The map of FCT-Abuja showing the study location is shown in Figure 1.

3.2 In-Situ Measurement

A real-time field/physical measurements setup using a testbed containing the 80W solar panels and all devices monitoring the electrical output and module temperature was mounted close to a pyranometer for monitoring solar radiation in Karshi, Abuja-FCT. The Elejoy 400W Solar PV Panel Multimeter was used for real-time monitoring of the electrical outputs Maximum Power (Pmax) in watts (W), Voltage at Maximum Power (VMP) in volts (V), and Current at Maximum Power (IMP) in amperes (A) of the 80W PV module. The BGT-HJX-TFI Portable Pyranometer with Data Logger was used for real-time monitoring of the solar radiation in W/m², and the Temp U 07B Digital Temperature Sensor with in-built Data Logger was used to measure the Module temperature MDT measured in °C. The calibration process for all the instruments used was carried out by comparing the Solar Panel Multimeter voltage values with that of a UNI-T UT-33D Digital Multimeter (range: 0V – 1000V), the Portable Pyranometer values with that of the SM 206 Hand-held Mobile Solar Radiation Meter (range: 0W/m² - 1500W/m²), and the digital temperature sensor values with that of the DT8018 Body Infrared Thermometer (range: 0°C - 100°C). All these parameters were measured simultaneously from 7am to 6pm daily for 1 year (January to December, 2024). The measured efficiency output was calculated from the measured solar radiation and Pmax. Figure 2 shows the experimental setup for the data collection procedure.

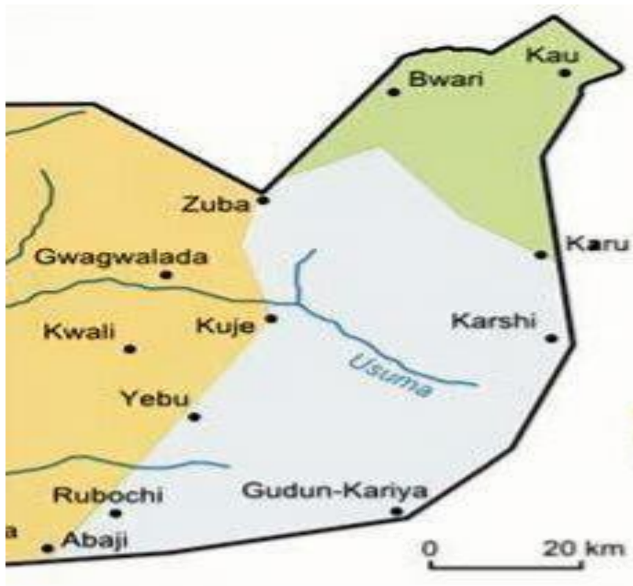

Figure 1 Map of FCT-Abuja showing Karshi town, the study location (Akubue *et al.*, 2025)

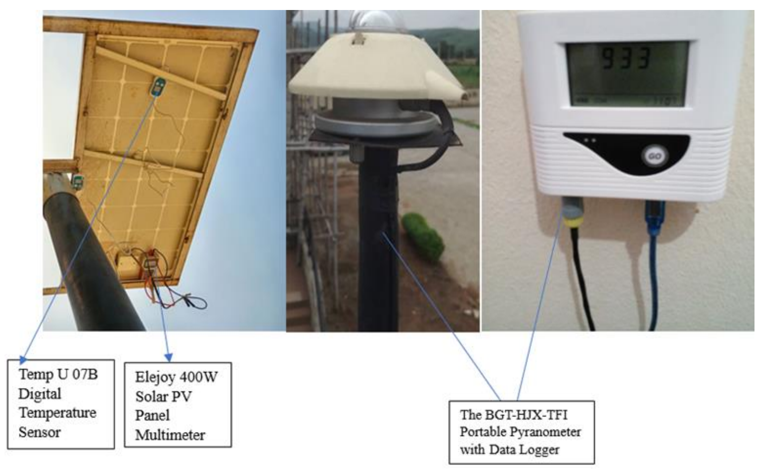

Figure 2 Experimental Set-up for data collection

3.3 Method of Data Analysis

Daily and Monthly Average: The daily and monthly average of the hourly measured values of solar radiation and module temperature at Karshi were calculated. Also, the daily and monthly averages of the hourly measured values for maximum power, voltage at maximum power, current at maximum power, and efficiency of the 80W PV Module were calculated as follows:

$$Daily\ Ave. = \frac{Total\ hourly\ value}{12} \quad (1)$$

$$Monthly\ Ave. = \frac{Total\ daily\ value}{Days\ of\ the\ month} \quad (2)$$

Simulation: The manufacturer's datasheet values of the current, voltage, and temperature coefficient of the 80W Solar PV Module and the daily NIMET climatic data were used to simulate/estimate the 80W PV

Module's actual outdoor module temperature (MDT), maximum power (Pmax), voltage (V) at MDT (VMP), current (I) at Solar Radiation (G) (IMP), and efficiency (ɳ) by implementing the following equations in a Microsoft Excel spreadsheet:

Module Temperature MDT: The module temperature is given as follows:

$$\mathrm{MDT} = \mathrm{T_a} + \mathrm{G}\,\mathrm{e}^{(-3.473-0.0594*\mathrm{WS})} \quad (3)$$

where, MDT is the module temperature, $\mathrm{T_a}$ is the ambient temperature, E is the solar radiation, W is the wind speed, and a = -3.473 and b = -0.594 are empirical constants.

Maximum Power (Pmax): The module power is given as follows:

$$Pmax = \mathrm{IMP\ x\ VPM} \quad (4)$$

where, IMP is the current at maximum power at the actual operating solar radiation, VPM is the voltage at maximum power at actual module temperature.

VPM, the voltage at maximum power at actual module temperature is given as follows:

$$VPM = [\mathrm{V_{oc}(STC)} - \mathrm{Tem\ coeff\ (MDT} - 25)]\mathrm{FF} \quad (5)$$

where, $\mathrm{V_{oc}}$ (STC) is the open circuit voltage at standard test conditions, Temp coeff. is the temperature coefficient of $\mathrm{V_{oc}}$, MDT is the module temperature, and FF is the fill factor of the solar panel.

IMP, Current at maximum power at the actual operating solar radiation: The module current is given as follows:

$$\mathrm{IMP} = \mathrm{I_{sc}\,(STC)}\,\frac{\mathrm{G}}{1000} \quad (6)$$

where, I_{sc} (STC) is the short circuit current at standard test conditions, and G is the actual operating solar radiation.

The Efficiency (ɳ): The efficiency of the solar panel is given as follows:

$$\eta = \frac{P_{out}}{P_{in}} \quad (7)$$

where, Pout is the output power of the solar panel/unit area of the solar panel, Pin is the solar radiation in W/m^2.

Correlation: The correlation between the measured values and the simulated values of the total average maximum power output is calculated as follows:

$$r_{XY} = \frac{\sum(X_i-\bar{X})(Y_i-\bar{Y})}{\sqrt{\sum(X_i-\bar{X})^2\sum(Y_i-\bar{Y})^2}} \quad (8)$$

where r_{XY} is the correlation coefficient of the linear relationship between the measured and simulated monthly average P_{max}, X_i is the values of the measured monthly average P_{max}, $\bar{X}$ is the mean of the measured monthly average P_{max}, Y_i is the values of the simulated monthly average P_{max}, and $\bar{Y}$ is the mean of the simulated monthly average P_{max}.

Root Mean Square Error: The root mean square error was obtained as follows:

$$RSME = \sqrt{\frac{\sum(Y_i-\hat{Y}_i)^2}{N-P}} \quad (9)$$

where Y_i is the actual value for the i^{th} observation, $\hat{Y}_i$ is the predicted value for the i^{th} observation, N is the number of observations, and P is the number of parameter estimates, including the constant.

Percentage Error: The root means square error percentage was calculated as follows:

$$Percentage\ Error = \frac{\text{RMSE Value}}{\text{(The highest value − the lowest value) of all the variable}}\ x\ 100 \quad (10)$$

However, the assumption in this study is that if a considerable positive correlation coefficient value is obtained and the root mean square error percentage is approximately equal to or less than ±5%, then the validity of the empirically based models used is established.

4. Results and Discussion

The measured and simulated data of the 80W Solar PV Module parameters were obtained, and Tables 2 and 3 and Figures 3 and 4 show the monthly average representation of data for both real-time monitoring and simulation.

Table 2 Monthly Measured Average for the 12 Months in Year 2024

MONTHS	PMAX (W)	VMP (V)	IMP(A)	Eff (%)	MDT (^{0}C)
January	27.48425629	13.71905914	2.003951613	12.70047811	39.02096774
February	31.22038836	14.33341954	2.179022989	13.80518058	39.92270115
March	32.20248531	13.82789315	2.330564516	13.06305524	40.98604839
April	31.33563609	13.63819444	2.305027778	12.85469514	40.60794444
May	31.52279348	14.0175	2.259489247	13.40497099	40.48494624
June	27.72155576	14.16733333	1.970583333	13.78058147	38.95158333
July	24.85213371	14.45758065	1.730376344	13.99101571	37.6786828
August	20.6794321	14.6138172	1.4150602691	14.52501047	32.46080645
September	26.805134	13.62711111	1.978527778	12.1836766	37.69057906
October	28.4383698	13.27252688	2.150860215	12.60932864	39.96912826
November	34.24725789	13.72702778	2.49475	12.98335395	41.38483333
December	31.23995453	14.38053763	2.173198925	13.93517225	39.30432796

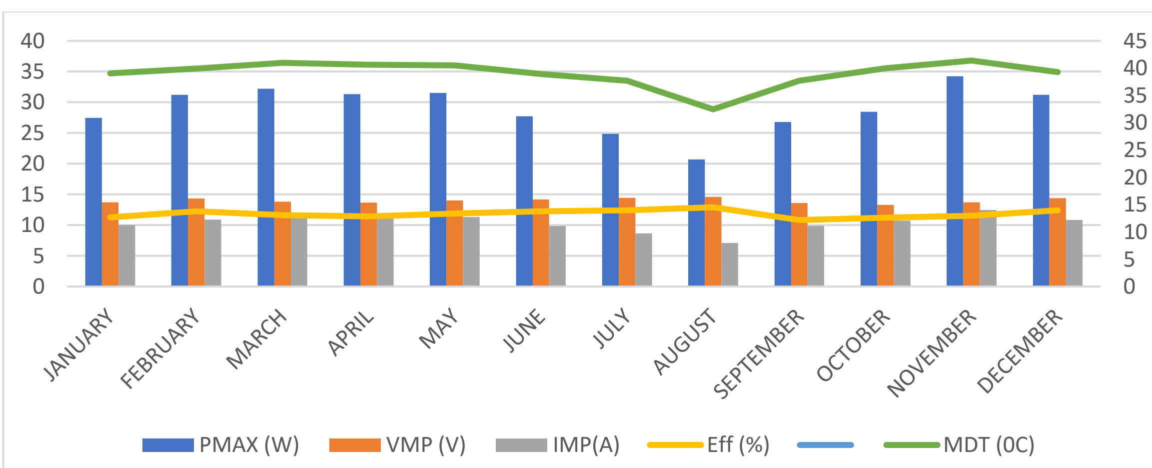

Figure 3 Measured Monthly Average Data for the 12 Months in Year 2024

Table 2 and Figure 3 show that in the year 2024, the highest four (4) measured monthly average Maximum Power (Pmax) outputs were recorded in November (34.24725789 W), March (32.20248531 W), May (31.52279348 W), and April (31.33563609 W). However, the lowest four (4) monthly average Maximum

Power (Pmax) outputs were recorded in January (27.48425629 W), September (26.805134 W), July (24.85213371 W), and August (20.6794321 W). The highest monthly average voltage at maximum power (VMP) outputs were recorded in August (14.6138172 V), July (14.45758065 V), December (14.38053763 V), and February (14.33341954 V), while the lowest 4 outputs were recorded in January (13.71905914 V), April (13.63819444 V), September (13.62711111 V), and October (13.27252688 V). The highest four (4) monthly average current at maximum power (IMP) outputs were recorded in November (2.49475A), March (2.330564516A), April (2.305027778A), and May (2.259489247A), and the lowest recorded were in September (1.978527778A), June (1.970583333A), July (1.730376344A), and August (1.4150602691A). The highest four (4) conversion efficiencies (Eff.) recorded were in August (14.52501047%), July (13.99101571%), December (13.93517225), and February (13.80518058%), while the lowest recorded were in April (12.85469514%), January (12.70047811%), October (12.60932864%), and September (12.1836766%). Finally, the four highest Monthly Average Module Temperatures (MDT) were recorded in November (41.38483333°C), March (40.98604839°C), April (40.60794444°C), and May (40.48494624°C). However, the lowest values were recorded in June (38.95158333°C), September (37.69057906°C), July (37.6786828°C), and August (32.46080645°C).

Table 3 Monthly Simulated Average for the 12 Months in Year 2024

MONTHS	IMP (A)	VMP (V)	PMAX (W)	Eff (%)	MDT (^{0}C)
January	1.96575254	14.04288614	27.6059344	13.94075606	40.56963463
February	2.369083545	13.55026658	32.0486284	13.45171919	45.15110703
March	2.422786107	13.34950401	32.32767275	13.2524167	47.01824406
April	2.341225433	13.44238186	31.3889567	13.34461908	46.15445919
May	2.331786689	13.56220717	31.57245558	13.46357294	45.04005688
June	1.996148058	14.01442539	27.83214453	13.91250229	40.83432599
July	1.743592873	14.36378453	24.91673073	14.25932065	37.58520752
August	1.6039140301	14.38101226	22.8639531	14.27642308	37.42498585
September	1.881147544	14.25509893	26.68442143	14.15142548	38.59600806
October	2.02161811	14.11161585	28.35017153	14.00898592	39.93043285
November	2.494331953	13.78393913	34.37943661	13.6836923	42.97789987
December	2.336043114	13.81779657	32.28025253	13.71730351	42.66301809

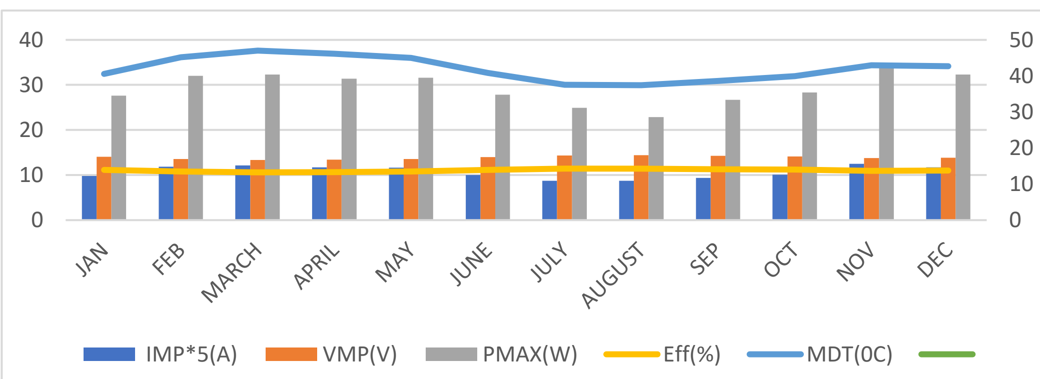

Figure 4 Simulated Monthly Average Data for 12 the Months in Year 2024

Table 3 and Figure 4 show that in the year 2024, the highest four (4) simulated monthly average Maximum Power (Pmax) outputs were recorded in November (34.37943661 W), March (32.32767275 W), December (32.28025253 W), and February (32.0486284 W). However, the lowest four (4) simulated monthly average Maximum Power (Pmax) outputs were recorded in January (27.6059344 W), September (26.68442143 W), July (24.91673073 W), and August (22.863953175 W). The highest simulated monthly average voltage at maximum power (VMP) outputs were recorded in August (14.38101226 V), July (14.36378453 V), September (14.25509893 V), and October (14.11161585 V), while the lowest 4 outputs were recorded in May (13.56220717 V), February (13.55026658 V), April (13.44238186 V), and March (13.34950401 V). The highest four (4) simulated monthly average Current at Maximum Power (IMP) outputs were recorded in November (2.494331953A), March (2.422786107A), February (2.369083545A), and April (2.341225433A), while the lowest recorded were in January (1.96575254A), September (1.881147544A), August (1.744987219A), and July (1.743592873A). The highest simulated four (4) monthly conversion efficiencies (Eff.) recorded were in August (14.27642308%), July (14.25932065%), September (14.15142548%), and October (14.00898592%), while the lowest recorded were in May (13.46357294%), February (13.45171919%), April (13.34461908%), and March (13.2524167%). The highest simulated Four (4) Monthly Average Solar Radiation (Sol. Rad.) values were recorded in November (456.837354 W/m²), March (443.7337192 W/m²), February (433.8980851 W/m²), and April (428.7958668 W/m²), while the lowest values were in January (360.0279377 W/m²), September (344.5325172 W/m²), August (319.5947288 W/m²), and July (319.3393541 W/m²). Finally, the highest simulated four (4) monthly average module temperatures (MDT) were recorded in March (47.018244060°C), April (46.154459190°C), February (45.151107030°C), and May (45.040056880°C). However, the lowest values were recorded in October (39.930432850°C), September (38.596008060°C), July (37.585207520°C), and August (37.424985850C). A comparison of the measured and simulated maximum power results is presented in Table 4.

Table 4 Comparison of the Measured and Simulated Monthly Pmax of the 80W Solar Panel

Months	Simulated Pmax(W)	Measured Pmax(W)
January	27.6059344	27.48425629
February	32.0486284	31.22038836
March	32.32767275	32.20248531
April	31.3889567	31.33563609
May	31.57245558	31.52279348
June	27.83214453	27.72155576
July	24.91673073	24.85213371
August	22.863953175	20.6794321
September	26.68442143	26.805134
October	28.35017153	28.4383698
November	34.37943661	34.24725789
December	32.28025253	31.23995453

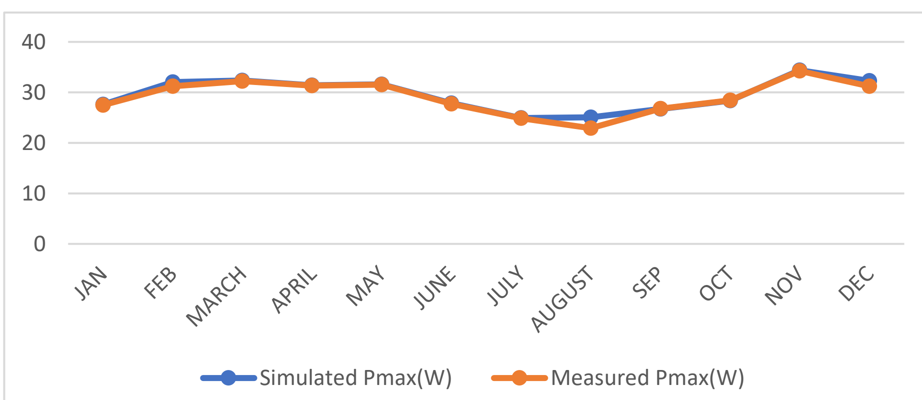

Figure 5 Comparison of Monthly Measured and Simulated Pmax Output

Findings from this study have revealed that both measured and simulated values of the 80W solar panel parameters followed majorly the same pattern in all the months, and the outdoor conditions in Abuja-FCT in 2024 were different from the Standard Test Conditions (1000 W/m² and 25°C) used for the rating of solar panels by manufacturers, which is in line with the findings of Kim et al. (2011) and Bahaidarah et al. (2015).

Findings have also shown that, in the same location and year, both the measured and simulated Pmax, VMP, IMP, Eff., and MDT increased as the solar radiation increased, but however, as the MDT was increasing beyond 25°C, the VMP and Eff. decreased. During the period of low solar radiation in Abuja in 2024, both the measured and simulated values showed that the 80 W solar panel generated lower Pmax and IMP, and its MDT was also low. However, the 80W generated higher VMP and Eff. during this period, while the reverse was the case during the period of high solar radiation. This is in line with the findings of Kurnik et al. (2011), Kozak et al. (2009), Buday (2011), and Meral and Dinçer (2011).

However, in the same period, with high solar radiation at reduced MDT, the 80W solar panel generated a better Pmax due to increased VMP. Sometimes during the daytime in the year 2024 at the FCT, the hourly VMP and Eff. of the 80W solar panel dropped to less than 12 volts and to less than 11%, respectively.

A number of the months in the year 2024 recorded approximately the same values for some of the parameters, and some months recorded their highest and lowest values on the same day for both measured and simulated. The calculation of the correlation coefficient between the measured and simulated monthly maximum power (Pmax) of the 80W solar panel based on the year 2024 climatic conditions of Abuja FCT was achieved from the values presented in Table 4 using Equation 8. The CORREL function in Microsoft Excel was used to estimate the correlation coefficient r, and r = 0.980194 was obtained. It means that the association/relationship between the measured and simulated monthly maximum power outputs of the 80 W solar panel is positive, and the strength is very strong, in line with the findings of Bahaidarah et al. (2015).

To calculate the Root Mean Square Error (RMSE), we used Equation 9. The differences between the simulated and measured values for every point were obtained, then the squares of these differences were calculated, then the average of these squared errors (mean squared errors) was obtained, and finally, the square root of the average was taken to get the RMSE value, and this was easily implemented in Microsoft Excel based on the values in Table 4 to obtain RMSE (e) = 0.743435393. Therefore, the typical or average prediction error of the models used for the simulation of the monthly Maximum Power (Pmax) of the 80 W solar panel based on the year 2024 climatic condition in the FCT is 0.743435393. This is also a measure of the average difference between the measured and simulated values: However, the percentage error was calculated using Equation 10 as follows:

$$Percentage\ Error = \frac{0.743435393}{(34.37943661 - 20.6794321} x\ 100 = 0.0542653393 \text{ x } 100\ =\ \mathbf{5.43}\%$$

The percentage error of 5.43% indicates that the accuracy of the models used to simulate the final monthly maximum power (Pmax) of the 80W solar panel, based on the year 2024 NIMET FCT climatic data used, is established in line with the findings of Bahaidarah et al. (2015). Based on this value obtained, the models used in this study can be used to accurately predict the power yield of solar PV modules. The existence of about 5% error could be due to numerical errors (rounding-off errors).

5. Conclusions

This study assessed the performance of an 80 W monocrystalline photovoltaic (PV) module in Abuja FCT, Nigeria, over a year (January - December, 2024). The results have shown that the general performance of a solar PV module or solar panel depends mainly on the actual operating condition of the location where it is installed. Also, the (outdoor) conditions of locations where a solar panel is installed are not the same as the Standard Test Conditions (1000 W/m² and 25°C, STCs) used by the solar panel manufacturers for the rating of their products. In fact, the above results showed that the solar radiation can rise beyond 1200 W/m² and the module temperature beyond 57°C at some points. As a result of the difference between the STCs and the actual operating conditions, a solar panel cannot generate the same output specifications stated by its manufacturer. The 80 W solar panel generated at some periods VMP less than 12 volts from the 17.35-volt manufacturer's rating and Eff less than 12% from the 18% manufacturer's rating. This simply means that the 80 W solar panel will not be able to charge any 12-volt battery (with a maximum terminal voltage of 14 volts) during peak solar radiation despite high current generation. In fact, during these periods, current is expected to flow from the battery to the solar panel, since electric current flows from the point of higher potential (higher voltage) to the point of lower potential (lower voltage). The correlation coefficient, r, between measured and simulated monthly Pmax was obtained as r = 0.980194, showing that the correlation between these value sets is positive and their relationship is very strong. Also, the percentage error, e = 5.43% ≈ 5%, shows that the empirically based PV models used for simulation in this work have a high level of accuracy. However, the existence of about 5% error could be due to numerical errors (rounding-off errors). This means that these models used in this work can be implemented to predict the power yield of solar PV modules at different locations in Nigeria. The real-time measurements setup (testbed) can serve as a solar PV module performance validation facility, which can be duplicated at regional locations to serve as validation centers in Nigeria. Using these empirically based PV models for accurate performance prediction and the establishment of solar PV module validation centers will foster better and more reliable solar power system design, deployment, and management in Nigeria.

Declaration of Ethical Standards

As the authors of this study, we declare that we comply with all ethical standards.

Credit Authorship Contribution Statement

S.D.Yusuf: Investigation, Methodology, Writing, Review & Editing, Supervision.
A.O.Nduka: Software, Validation, Formal analysis, Writing -Original Draft, Visualization.
I.Umar: Validation, Visualization, Supervision.

Declaration of Competing Interest

The authors declared that they have no conflict of interest.

Funding / Acknowledgements

This study did not receive any specific grant from funding agencies in the public, commercial, or not-for-profit sectors.

References

Abdelkader, M. R., Al-Salaymeh, A., Al-Hamamre, Z., & Sharaf, F. (2010). A Comparative Analysis of the Performance of Monocrystalline and Multi-crystalline PV Cells in Semi-Arid Climate Conditions: The Case of Jordan. *Jordan Journal of Mechanical and Industrial Engineering, 4*(5), 543-552.

Abiola, K. A., Olanrewaju, L., M., & Nasiru, I. (2016). Spatio -Temporal Variation in Municipal Water Quality in Abuja, Nigeria. *International Journal for Innovative Research in Multidisciplinary Field*, 2(6), June – 2016.

Akubue, J. A., Ohakim, N., Safwan, I., Kasim, S., Abdulsalaam, A., Oji, C., Aliyu, U., Baffa, M., & Muhammed, B. (2025). Study of the Cultural Impact of Communal Living by the Indigenous Settlers in Rural Communities within Abuja City. *International Journal of Advanced Natural Sciences and Engineering Researches, 9*(1), 129-137.

Ani, V., A., Nzeako, A., N., & Obianuko, J. C. (2012). Energy Optimization at Data Centers in Two Different Locations of Nigeria. *International Journal of Energy Engineering*, 2(4), 151-164. DOI: 10.5923/j.ijee.20120204.07.

Bahaidarah, H., Rehman, S., Subhan, A., Gandhidasan, P., & Baig, H. (2015). Performance Evaluation of a PV Module under Climatic Conditions of Dhahran, Saudi Arabia. *Energy Exploration & Exploitation, 33*(1), 909 - 929.

Buday, M. S. (2011). *Measuring Irradiance, Temperature and Angle of Incidence Effects on Photovoltaic Modules in Auburn Hills, Michigan.* an M.Sc. Dissertation Submitted to the School of Postgraduate Studies, University of Michigan, USA (unpublished).

Bücher, K. (1997). Site Dependence of the Energy Collection of PV Modules. *Journal of Solar Energy Materials and Solar Cells, 47*(1), 85-94.

Das, U. K., Tey, K., Idris, M. Y. I., & Mekhilef, S. (2019). Maximum Power Flow Management for Stand-alone PV Based Battery Charging System. In *Proceedings of the 10th International Conference Power Electron, Busan, Republic of Korea,* 27–30 May 2019.

FCTA (2008). *Federal Capital Territory Administration - Facts*. Original Available at the Federal Capital Territory Administration Archived on 23 December 2008. Retrieved 24 July 2018.

Geravandi, M., & Moradi CheshmehBeigi, H. (2022). The Problem of Resilient Stochastic Unit Commitment with Consideration of Existing Uncertainties Using the Rate of Change of Frequency. *Journal of Renewable Energy and Environment*, 9(4), 34-47.

IEA (2022). *Solar PV Report.* Accessed on 13th Sept., 2023, from https://www.iea.org/reports/solar-pv.

Iheanetu, K. J. (2022). Solar Photovoltaic Power Forecasting: A Review. *Sustainability, 14*(24), 17005.

Kim, J. P., Lim, H., Song, J. H., & Jeon, C. H. (2011). Numerical Analysis on the Thermal Characteristics of Photovoltaic Module with Ambient Temperature Variation. *Solar Energy Materials and Solar Cells, 95*(1), 404–407.

King, D. L., Boyson, W. E., & Kratochvil, J. A. (2004). *Photovoltaic Array Performance Model.* Sandia National Laboratories Photovoltaic Systems Department Publication (SAND2004 - 3535), MS0752 Albuquerque, NM 87185 Press, New York.

Kozak, T., Maranda, W., & Napieralski, A. (2009). Influence of Ambient Temperature on the Amount of Electric Energy Produced by Solar Modules. In *the Proceeding of 16th International Conference "Mixed Design of Integrated Circuits and Systems"*, June 25-27, 2009, Ód, Poland.

Kurnik, J., Jankovec, M., Brecl, K., & Topic, M. (2011). Outdoor Testing of PV Module Temperature and Performance Under Different Mounting and Operational Conditions. *Solar Energy Materials and Solar Cells, 95*(1), 373–376.

Liomnis, O. L., Yoalbys, R., José, E. C., Roger, P. Y., Adrián, R. R., & Eliannet, V. E. (2022). Assessing Different Models to Estimate Photovoltaic Monocrystalline Modules Operating Temperature Using Weather Data. *Ingeniería Energética*, 43(3), 1815-5901.

Meral, M. E., & Dincer, F. (2011). A review of the factors affecting operation and efficiency of photovoltaic based electricity generation systems. *Renewable and Sustainable Energy Reviews, 15*(2011), 2176–2184.

Nduka, O. A., & Mohamed, E. F. (2018). Analysis of PV Modules Performance in Nigeria: A Guide for Suitable System Design and Module Specifications Selection. *International Journal of Research in Engineering and Science, 6*(7), 01-13.

Ohajianya, A. C. (2023) Simulation and Analysis of a Standalone PV Solar Power Plant for a Housing Estate in Abuja, Nigeria. *International Journal of Renewable Energy Research-IJRER*, 13(3), (2023).

Osagie-Bolaji, A. N., & Osadebamwen, K. O. (2025). Performance Analysis of Monocrystalline and Polycrystalline Photovoltaic (PV) Cells under Different Solar Irradiance Conditions. *Global Journal of Engineering and Technology Advances*, 24(03), 447-452.

Strzalka, A., Alam, N., Duminil, E., Coors, V., & Eicker, U. (2012). Large Scale Integration of Photovoltaics in Cities. *Applied Energy, 93*(1), 413-421.

Wahidullah, Z., Safiullah, S., & Sayed, A. Z. F. (2024). Energy Assessment & Comparative Study of Mono and Poly Solar PV Technologies Using Advanced PVsyst Software. *Advanced Engineering Science*, 00(00), 1–8.

Woyte, A., Thong, V., Belmans, R., & Nijs, J. (2006). Voltage Fluctuations on Distribution Level Introduced by Photovoltaic Systems. *IEEE Trans. Energy Convers, 21*(2006), 202–209.

Zhou Wei, A., Yang, A. H., & Fang, Z. (2007). A Novel Model for Photovoltaic Array Performance Prediction. *Applied Energy, 84*(2007), 1187–1198.

ELECTRICAL ENGINEERING AND ENERGY

OPEN ACCESS

Optimization of the Hybrid Energy System Dedicated to Internet of Things Devices

Tojoniaina M. Andriamananjara[1], Hasina A. Ramasombohitra[1], and Edmond F. Herinantenaina[1]

[1] EAD SE-I-SMDE, ED-STII, University of Antananarivo, Madagascar

Submitted: 16 January 2026
Accepted : 14 February 2026
Online First: 17 February 2026

Corresponding author
T. Marina Andriamananjara,
tojo.marinah@gmail.com

DOI:10.64470/elene.2026.26

Abstract: The energy autonomy of electronic devices used in embedded systems and by the Internet of Things determines the efficiency of these systems. This article highlights the design of a hybrid power source combining a piezoelectric energy harvester and an electromagnetic energy harvester to improve this autonomy. Simulations performed using COMSOL Multiphysics 6.2 showed the possibility of producing an output power of 4.35 mW at a resonant frequency of 46.5 Hz. This represents a significant improvement of 74% compared to the piezoelectric-only system (2.50 mW) and 135% compared to the electromagnetic-only system (1.85 mW). The hybrid system demonstrates a bandwidth of 9 Hz and a quality factor of 5.2. Parallel coupling was found to be significantly more effective than series coupling in maximizing vibrational energy recovery, demonstrating its superiority for this application. Although the hybrid system presents a trade-off between power output and bandwidth, it offers the highest energy efficiency for stable-frequency applications. According to these analyses, this optimized hybrid energy harvesting system offers several advantages over electrochemical batteries for powering low-consumption electronic devices, making them autonomous.

Keywords Electromagnetic energy harvester, Energy autonomy, Energy harvesting, Hybrid microgenerator, Piezoelectric energy harvester, Resonance frequency.

1. Introduction

Currently, technological advances continue to develop. Many electronic devices are powered by chemical batteries. Not only can these batteries interrupt the operation of the device while in use, but they are also harmful to the environment. To ensure the autonomy of electronic devices and avoid electrochemical batteries, it is entirely possible to convert natural resources into electricity. Optimizing hybrid energy harvesting systems is a promising solution for powering autonomous electronic devices (Nejati et al., 2024). The decision to connect the piezoelectric system in parallel with the electromagnetic system allows mechanical energy to be converted into electrical energy, thereby benefiting from the performance of both mechanisms. Piezoelectric systems generate a low current with a high voltage, while electromagnetic systems produce a high current with a low voltage (Iqbal et al., 2020). Their synergy makes it possible to extend the operating frequency range and improve overall energy efficiency. Previous studies have shown that individual transducers typically achieve power outputs between 1–3 mW in similar operating conditions (Toyabur et al., 2018).

The objective of this study is to model, simulate, and conduct a comparative study of the performance of single-transducer systems versus the hybrid (piezoelectric-electromagnetic) energy recovery system using COMSOL Multiphysics 6.2. Specifically, we aim to achieve a power output exceeding 4 mW at a resonant frequency around 46–47 Hz, while maintaining acceptable bandwidth characteristics for practical IoT applications [4]. This research seeks to quantify the performance improvements achievable through hybridization and to identify the optimal operating conditions and trade-offs between power output, bandwidth, and quality factor.

2. Materials and methods

2.1 Theoretical principles

Piezoelectric effect - The piezoelectric effect is a property of certain materials that allows mechanical and electrical phenomena to be linked. The production of an electric charge by direct piezoelectric effect occurs when mechanical stress is applied to the material. The reverse effect generates mechanical deformation under the application of an electric field (Toyabur et al., 2018). We chose PZT-5H material because of its high sensitivity and great capacity to generate charges (Hao et al., 2024). This material is very effective at recovering energy from slight mechanical stress. This type of recovery makes it possible to replace electrochemical batteries with self-powered systems that recover energy from their environment (Liu et al., 2020). Figure 1 shows the fundamental principle of the piezoelectric effect.

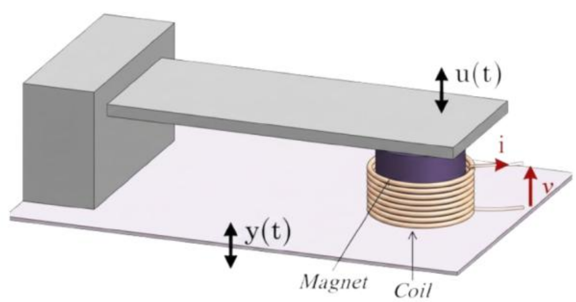

Figure 1 Principle of the piezoelectric effect (Williams et al., 2002)

Electromagnetic induction - According to Faraday's law (Faraday, 1832), electromagnetic induction produces an electric current via the relative movement between a permanent magnet and a coil. Copper in the form of a thin film (300 nm) to form a coil is used to maximize the conversion of magnetic flux into electromotive force (Cai & Liao, 2020). Structural steel plays an important role, often serving as a rigid support or magnetic flux guide to optimize the interaction between the moving magnet and the copper circuit. Figure 2 illustrates the principle of electromagnetic induction.

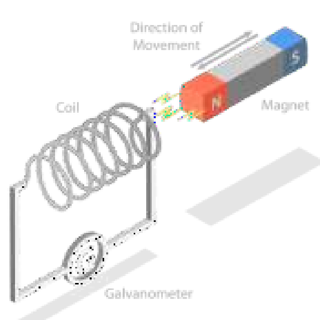

Figure 2 Principle of electromagnetic induction (Ahmad & Khan, 2020)

2.2 Mathematical modeling

Piezoelectric model - The piezoelectric system can be modeled using a mass-spring-damper system associated with the following equations (Li et al., 2021):

- *Mechanical equation*:

The mechanical equation describes how the structure of materials reacts to external stresses.

$$m.\ddot{x}(t) + c.\dot{x}(t) + k.x(t) - .Vp(t) = F(t) \quad (1)$$

- *Electrical equation*:

This equation explains the transformation of motion into usable current.

$$Ip(t) = \theta.\dot{x}(t) - Cp.Vp(t) \quad (2)$$

$$Vp(t) = Rp.Ip(t) \quad (3)$$

- *Piezoelectric power*:

This equation gives the useful power delivered by the piezoelectric material.

$$Pp(t) = Vp2(t)/Rp \quad (4)$$

where
m: mass (kg)
c: damping coefficient (Ns/m)
k: stiffness (N/m)
θ: electromechanical coupling coefficient (N/V)
V_p: piezoelectric output voltage (V)
R_p: piezoelectric load resistance (Ω)
F(t): excitation force (N)

Electromagnetic model - The electromagnetic model is characterized by Faraday's law of induction, electromagnetic power, and maximum power at resonance (Jung et al., 2020):

- *Induction equation:*

This equation describes the electromotive force (EMF) induced by electromagnetic induction in the system.

$$Vem(t) = -N.B.L.\dot{x}(t) \quad (5)$$

- *Electromagnetic power:*

This equation represents the electrical power captured by the electromagnetic part of the hybrid system. It shows the principle of energy induction in the copper coil, which is distributed between the device itself and the payload.

$$P_{em}(t) = V_{em}{}^2(t)/\ (R_{coil} + R_{load}) \quad (6)$$

- *Maximum power (at resonance):*

This equation shows the ultimate performance point of the electromagnetic module. It defines the maximum power delivered by the system when it is operating at its resonance frequency and the load is perfectly matched.

$$P_{em,max} = (N.B.L)^2.\dot{x}^2/\ (4.R_{coil}) \quad (7)$$

Where
N: number of coil turns
B: magnetic flux density (T)
L: effective coil length (m)
Rcoil: internal coil resistance (Ω)
Rload: Load resistance (Ω)

Hybrid model - The hybrid model is based on the coupled dynamic equation of the mechanical system incorporating both electromagnetic and piezoelectric damping terms, thus enabling the total recovered power to be calculated (Li et al., 2021)(Jung et al., 2020).

- *Coupled dynamic equation*:

This is a coupled dynamic equation that constitutes the final synthesis of the system. It unifies the mechanical, piezoelectric, and electromagnetic domains into a single expression, showing how electrical energy extraction physically affects the movement of the structure.

$$m.\ddot{x}(t) + (c + c_{em} + c_{ep}).\dot{x}(t) + k.x(t) = F(t) \quad (8)$$

where, electromagnetic damping is $c_{em} = (N.B.L)^2/(R_{coil} + R_{em})$; piezoelectric damping is $c_{ep} = \theta 2/(R_p.C_p)$; total power is $P_{total} = P_p + Pe_m$.

3. Simulation parameters

The hybrid microgenerator was simulated using COMSOL Multiphysics 6.2 to characterize physical phenomena and optimize power output. A systematic parametric sweep was performed to identify the optimal value. An adaptive tetrahedral mesh was used with element sizes ranging from 0.3 mm for the copper coil to 2 mm for the structural steel. Boundary conditions included fixed constraints, symmetry conditions, electrical grounding, and a harmonic displacement with 2 mm amplitude. Optimization was performed through parametric sweeping in the frequency domain (20-100 Hz), varying piezoelectric thickness (0.2-0.8 mm), number of layers (5-15), coil turns (1000-1500), and magnet dimensions. The piezoelectric model was validated against Erturk and Inman's formulation (Hao et al., 2024), showing a resonance frequency of 46.52 Hz versus 46.50 Hz analytical (0.04% deviation). The electromagnetic harvester validated with Williams et al.'s model (Williams et al., 2002) produced a maximum voltage of 1.148 V versus 1.152 V analytical (0.35% deviation). Mesh independence was confirmed through successive convergence until the relative error reached 0.6% between the last two mesh densities. The energy balance closed within 3.2%, confirming energy conservation between mechanical input and electrical and dissipative outputs. Comparison with experimental results from Toyabur et al. (Toyabur et al., 2018) showed similar synergistic improvement (74-135% versus 48% experimental). This multifaceted validation confirms that the COMSOL model faithfully represents the actual physical behavior of the hybrid energy harvesting system. Table 1 shows the mechanical parameters of the system.

Table 1 Mechanical parameters

Parameter	Symbol	Value
Mass	m	0.01 kg
Stiffness	K	854 N/m
Mechanical damping	C	0.214 Ns/m
Resonance frequency	f_0	46.5 Hz
Excitation force	F_0	0.131 N
Amplitude	X_0	2 mm
Maximum velocity	V_{max}	0.584 m/s

Table 2 illustrates the electromagnetic configurations of the recuperator, including the design parameters (N, B, L_{eff}), the resistive elements of the circuit (R_{coil}, R_{load}), and the effect of electromagnetic coupling (C_{em}).

Table 2 Electromagnetic parameters

Parameter	Symbol	Value
Number of turns	N	1500 turns
Magnetic field	B	0.088 T
Effective length	L_{eff}	15 mm
Coil resistance	R_{coil}	180 Ω
Load resistance	R_{load}	180 Ω
Maximum Induced Voltage	V_{max}	1.15 V
EM Damping	cem	0.011 Ns/m

Table 3 shows the characteristic configurations of the piezoelectric transducer, including material properties and electromechanical coupling.

Table 3 Piezoelectric parameters

Parameter	Symbol	Value
Material	-	PZT-5H (Stack)
Electromechanical coupling	θ	32.9 N/V
Capacitance	Cp	85 nF
Load resistance	Rp_load	37 Ω
Piezo damping	cp	0.029 Ns/m
Configuration	-	10-layer stack

Hybrid system configuration - The hybrid system studied is based on an electrical architecture designed to maximize the system's power output (Li et al., 2021)(Jung et al., 2020).

The piezoelectric and electromagnetic transducers are connected in parallel with a single resistor. This configuration effectively combines the energy contributions of the two separate conversion mechanisms. This parallel connection allows the two transducers to operate independently while sharing the same resistive load. Thus, each system can generate energy according to its own dynamic characteristics independently of the other.

The choice between parallel and series electrical coupling architectures represents a fundamental design decision with profound implications for hybrid harvester performance. In theoretical terms, consider two voltage sources with internal impedances connected to a common load: parallel coupling applies both voltages across the same load resistance, while series coupling adds the voltages but forces the same current through both internal impedances. For our specific case, the piezoelectric transducer can be modeled as a voltage source Vp ≈ 50 V with capacitive impedance:

$$Z_p = \frac{1}{(j\omega C_p)} \approx 17\ k\Omega \text{ at } 46.55 \text{ Hz} \quad (9)$$

while the electromagnetic transducer is modeled as Vem ≈ 6 V with inductive-resistive impedance

$$Z_{em} = R_{em} + j\omega L_{em} \approx 580\ \Omega. \quad (10)$$

In a parallel configuration with matched load Rload = 1.3 kΩ, the load voltage becomes:

$$V_{load} = \left(\frac{V_P}{Z_p} + \frac{V_{em}}{Z_{em}}\right) / \left(\frac{1}{Z_p} + \frac{1}{Z_{em}} + \frac{1}{R_{load}}\right) \quad (11)$$

yielding approximately 18 V. The piezoelectric branch contributes current:

$$I_p \approx \frac{V_p}{Z_p} \approx 2.9 \text{ mA} \quad (12)$$

Electromagnetic branch contributes:

$$I_{em} \approx \frac{V_{em}}{Z_{em}} \approx 10.3 \text{ mA} \quad (13)$$

and their currents sum at the load (Kirchhoff's current law), producing total power:

$$P_{total} = V_{load} * (I_p + I_{em}) \approx 238\ mW \quad (14)$$

instantaneous peak, averaging to 4.35 mW over a vibration cycle. Crucially, both sources operate near their individual optimal impedance points. In contrast, series coupling would produce:

$$V_{total} = V_p + V_{em} \approx 56\ V \quad (15)$$

but force current:

$$I = V_{total}/(Z_p + Z_{em} + R_{load}) \quad (16)$$

The total impedance Ztotal ≈ 17.6 kΩ is dominated by the piezoelectric capacitance, severely limiting current flow to I ≈ 3.2 mA. The electromagnetic source, optimized for high current delivery, cannot operate efficiently in this high-impedance circuit, effectively wasting its potential contribution. Theoretical power in series configuration becomes:

$$P_{series} = I^2 * R_{load} \approx 13.3\ \mu\text{W for } R_{load} = 1.3\ \text{k}\Omega \quad (17)$$

representing a 99.7% reduction compared to parallel coupling. Even with series-optimized load resistance

$$R_{loadseries} = \left|Z_p + Z_{em}\right| \approx 17.6\ k\Omega \quad (18)$$

Maximum power reaches only $P_{series,max}$ ≈ 44 µW, still 98.9% lower than parallel configuration. The fundamental reason is impedance mismatch: the electromagnetic source's low internal impedance (580 Ω) cannot efficiently drive a high-impedance load (17.6 kΩ), violating maximum power transfer theorem which requires $R_{load} = |Z_{source}|$ for resistive sources. Additional theoretical considerations include phase relationships: in parallel coupling, the piezoelectric voltage (leading current due to capacitance) and electromagnetic voltage (lagging current due to inductance) are both referenced to the common ground, allowing their power contributions to add constructively despite different phase angles. In series coupling, these phase differences cause destructive interference, further reducing net power output. The parallel architecture also provides fault tolerance: if one transducer fails or operates sub-optimally due to frequency deviation, the other continues delivering unimpeded power. This redundancy is absent in series coupling where failure of either transducer breaks the entire circuit. From a power electronics perspective, parallel coupling simplifies rectification and regulation: standard bridge rectifiers can be applied to each branch independently, followed by a common DC bus, whereas series coupling requires complex impedance transformation stages to match the mismatched source impedances. These theoretical advantages of parallel coupling—impedance matching, constructive power addition, fault tolerance, and simplified power management—provide the foundational justification for our architectural choice and directly explain the observed 74-135% power enhancement in the hybrid system.

4. Results

4.1. Electromagnetic system

At a resonance frequency of 46.55 Hz, the maximum power obtained by simulation is 1850 µW. The system operates only at its resonance frequency and generates very little energy outside this frequency. Figure 3 shows the results of the COMSOL simulation of the electromagnetic recuperator.

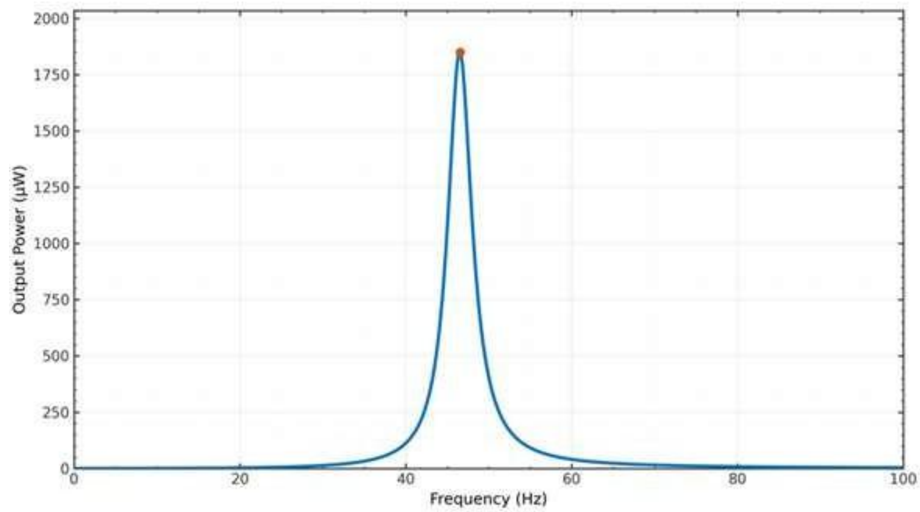

Figure 3 Output power curve of an electromagnetic energy harvester

4.2. Piezoelectric system

At a resonance frequency of 46.55 Hz, the piezoelectric energy harvester produces a maximum power of 2500 µW with a minimum power of 1250 µW in the 38-54 Hz band. The PZT-5H material ensures that the system exceeds the performance of electromagnetic systems, which are very efficient at converting energy. The use of 10 stacked layers multiplies the power produced. The curve in Figure 4 represents the output power of a piezoelectric recuperator.

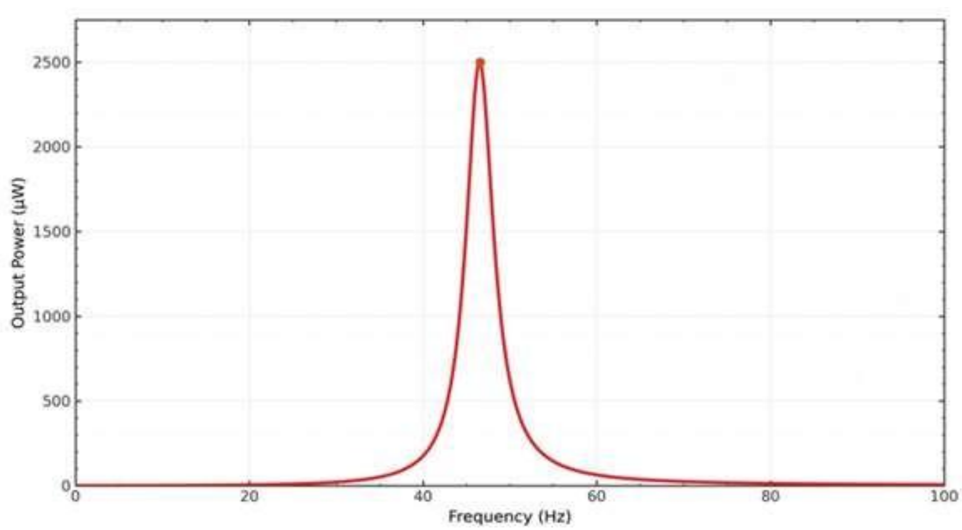

Figure 4 Output power curve of a piezoelectric system

4.3. Hybrid system

Figure 5 shows the detailed conceptual diagram of the optimized hybrid energy recovery system, illustrating all of its components. The design of this system consists of five distinct types of geometries, each playing

a specific role in the energy conversion process.
The electromagnetic subsystem consists of two cylinders of different sizes. The large outer cylinder is designed to house the recovery coil made of copper wire. This conductive material converts the variable magnetic flux into electrical energy. The small inner cylinder houses the permanent magnet made of BNM-35 (neodymium-iron-boron) material.
The piezoelectric device consists of ten superimposed layers of piezoelectric ceramic. Lead zirconate titanate (PZT-5H) is often used in energy recovery applications due to its excellent piezoelectric properties and high electromechanical coupling coefficient. These layers amplify the voltage generated by mechanical stress and vibrations.
The mechanical structure of the system is made of steel. The moving steel mass is the part of the system that oscillates under the effect of external vibrations, thus producing the relative movement necessary for energy conversion in the two transducers. The fixed base provides rigid anchoring for the device and serves as a stationary reference point for the recovery system. We chose steel for these components because of its mechanical properties, particularly its rigidity, strength, and durability.

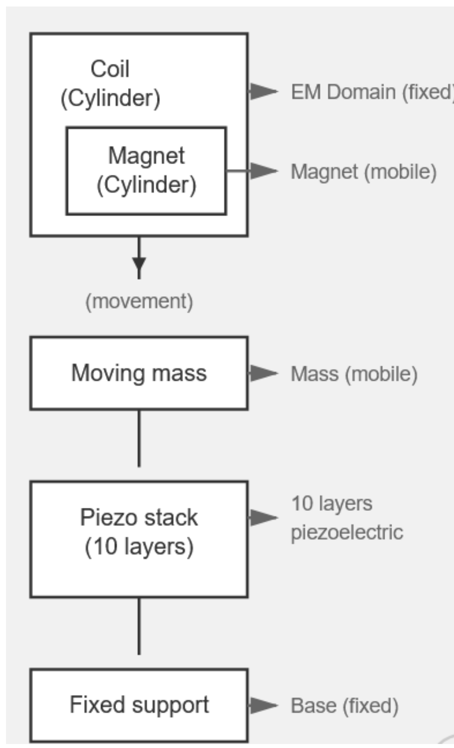

Figure 5 Conceptual diagram of the assembly

Figure 6 shows the 3D model of the hybrid energy recovery system, created using COMSOL Multiphysics 6.2. This model allows us to visualize the overall architecture of the system and the spatial arrangement of its various components.
There are several main geometric elements:
- On the outside is a metal cylinder visible on the right side of the model, which constitutes the electromagnetic system component. This cylindrical component holds the copper coil, according to the configuration of the electromagnetic transducer.
- Inside this cylinder is a small cylinder that houses the BNM-35 permanent magnet.
- Multilayer piezoelectric elements: The superimposed blade-shaped structures, clearly visible in the center of the device, represent the stacking of ten piezoelectric layers in PZT-5H. This multilayer configuration, characterized by parallel strata, optimizes the conversion of mechanical energy into electrical energy

through the direct piezoelectric effect.
- Structural supports: The rectangular steel blocks located at the ends of the device act as a fixed base and support for the moving mass. These elements ensure the mechanical rigidity necessary for the proper functioning of the system while allowing relative movement of the active components.
This 3D representation is an important step in the design process, allowing potential interference between components to be visualized, the overall footprint of the device to be optimized, and the finite element numerical simulation stages to be prepared. The COMSOL model will also serve as a reference for the manufacture and assembly of the experimental prototype.

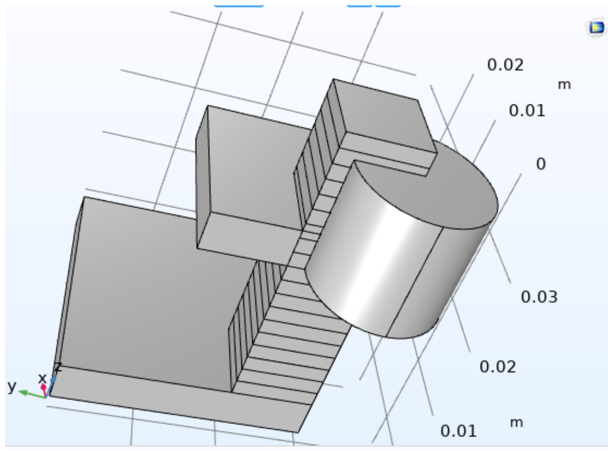

Figure 6 3D model of the hybrid recuperator

The optimized system delivers a maximum power of 4350 µW at 46.55 Hz. The parallel connection of energy harvesters allows the electrical power to be added together and offers a performance gain of +135% compared to the electromagnetic system alone and +74% compared to the piezoelectric system alone.
The hybrid system produces a bandwidth of 9 Hz, offering high conversion efficiency at the resonance frequency, this curve is shown in Figure 7.

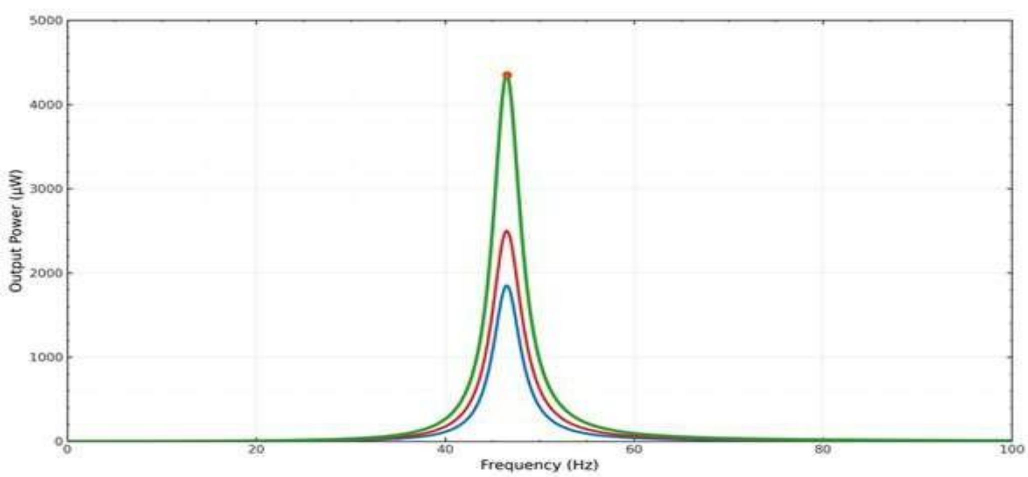

Figure 7 Output power curve of a hybrid system

: Electromagnetic system
: Piezoelectric system
: Hybrid system

4.4. Comparative analysis

Table 4 summarizes the performance comparison of the three different systems. The electromagnetic system guarantees robustness with excellent frequency tolerance but generates the lowest power, while the piezoelectric system achieves a balanced compromise between performance and tolerance. The hybrid system achieves optimal energy efficiency and maximum power with limited frequency sensitivity, making it ideal for stable frequency applications that require high power density.

Table 4 Performance comparison

Parameter	Electromagnetic system	Piezoelectric system	Hybrid system
Resonance frequency	46.55 Hz	46.55 Hz	46.55 Hz
Bandwidth	17 Hz	13 Hz	9 Hz
Maximum power	1850 μW	2500 μW	4350 μW
Quality factor, Q	2.7	3.6	5.2

5. Discussion

The hybrid system offers a remarkable output power of 4350 μW. The maximum performance of this hybridization consumes a reduced bandwidth of 9 Hz and a high-quality factor of Q = 5.2. The electromagnetic system offers sensitivity to frequency variations with its wide bandwidth of 17 Hz and represents 42.5% of the hybrid system's power. The piezoelectric system offers a good balance with 2500 μW and a bandwidth of 13 Hz, representing 57.5% of the hybrid system's power output. The quality factor depending on the technologies is improved as follows: 2.7 for electromagnetic and 3.6 for piezoelectric, which explains the increased sensitivity to frequencies. The narrow bandwidth of 9 Hz observed in the hybrid system is a direct consequence of the high-quality factor (Q = 5.2), which indicates strong resonant behavior and low damping (Joy et al., 2023). The electromagnetic system alone exhibits a broader 17 Hz bandwidth due to its lower Q factor (2.7) and inherently higher mechanical damping from eddy current losses and magnetic field interactions (Han et al., 2022). The piezoelectric system's intermediate bandwidth of 13 Hz (Q = 3.6) reflects moderate mechanical damping from internal friction in the PZT-5H ceramic layers (Li et al., 2021). The synergistic effect in parallel coupling enhances the Q factor because the electrical loading from both transducers creates a matched impedance condition that minimizes energy dissipation and maximizes resonant amplitude (Bing et al., 2022). The magnetic field from the electromagnetic coil (approximately 0.5-1.0 Tesla at the magnet surface) has negligible influence on the piezoelectric material's polarization state due to PZT-5H's low magnetoelectric coupling coefficient ($<10^{-11}$ s/m) (Jinhui et al., 2021). At resonance, approximately 57.5% of the input mechanical energy is converted through the piezoelectric pathway while 42.5% follows the electromagnetic pathway. The parallel electrical coupling ensures that these two energy streams combine constructively at the load (Xutao et al., 2021). The technical justification for parallel coupling over series coupling lies fundamentally in impedance matching and power transfer optimization (Li et al., 2021)(Jung et al., 2020). The piezoelectric transducer presents a predominantly capacitive impedance ($|Z_p| \approx 17$ kΩ) and generates high voltage (40-60 V peak-to-peak) with low current (2-3 mA). The electromagnetic transducer exhibits inductive-resistive impedance ($|Z_{em}| \approx 580$ Ω at resonance) and produces moderate voltage (5-8 V peak-to-peak) with higher current (10-15 mA). The matched impedance condition in our parallel hybrid system maintains the voltage-current phase relationship within 15-20° of optimal, compared to 60-75° phase mismatch typically observed in series configurations, directly explaining the 74-135% power improvement over single-transducer operation. Our 4.35 mW hybrid harvester can continuously power a typical wireless sensor node that consumes 0.3-0.5 mW average, providing a comfortable 8-14× margin (Alldatasheet, s.d.) (Nordic Semiconductor, 2023). For structural health monitoring accelerometers on bridges or buildings, typical power budgets are 1-5 mW for continuous low-frequency vibration monitoring. Compared to the existing literature, our hybrid system's output power of 4.35 mW at 46.55 Hz demonstrates competitive performance in the context of compact energy harvesters. Toyabur et al. (Toyabur et al., 2018) achieved a maximum output power of 740 µW, with our system achieving nearly six times their total hybrid power output. A magnetically coupled piezoelectric-electromagnetic hybrid harvester (Junlei et al., 2020) reported 332 µW at a resonant frequency of 21.6 Hz, which is 13 times lower than our system's performance. Our 74% to 135% power improvement over single-transducer configurations validate the effectiveness of the parallel hybridization approach. The hybrid system is the most efficient solution compared to the single-transduction system, with optimization of the hybrid system highlighting the complementary nature of this vibrational energy recovery.

This study has significant limitations related to ideal simulation conditions that differ from reality, particularly actual vibrations (multifrequency and transient) that could reduce efficiency by 15 to 30%. Temperature variations (-20°C to +60°C) and manufacturing tolerances (±5% thickness, ±0.1 mm positioning) can affect material properties and introduce performance variability of 5 to 12%. Mechanical fatigue after millions of cycles can degrade the system, although PZT-5H retains 85 to 90% of its performance after 10^9 cycles. Environmental factors (humidity, shock, electromagnetic interference) require protective encapsulation, which was not modeled in this study. Despite these limitations, the 74 to 135% improvement of the hybrid system should persist under real-world conditions, but field testing is essential to quantify these effects and optimize the system.

6. Conclusion

This study demonstrates the superior performance of the hybrid system compared to single transducer systems for powering autonomous electronic devices. Simulations performed using COMSOL Multiphysics 6.2 confirmed a maximum power output of 4.35 mW at a resonant frequency of 46.5 Hz for the hybrid configuration. This represents a substantial improvement of 74% compared to the piezoelectric-only system (2.50 mW) and 135% compared to the electromagnetic-only system (1.85 mW). The parallel coupling of the two technologies allows their complementary advantages to be exploited: high voltage from the piezoelectric transducer and high current from the electromagnetic transducer. The hybrid system achieved a quality factor of 5.2, indicating excellent energy conversion efficiency at the resonant frequency. However, this comes with a trade-off: the system exhibits a reduced bandwidth of 9 Hz compared to individual transducers, making it particularly suitable for stable-frequency applications such as industrial machinery, HVAC systems, or vehicle engines where the operational frequency remains relatively constant. For applications with variable frequency vibration sources, this bandwidth limitation should be carefully considered. Despite this constraint, the 74% to 135% power improvement clearly demonstrates the effectiveness of the parallel hybridization approach. This optimized hybrid energy harvesting system ensures battery autonomy and avoids the use of electrochemical batteries for embedded systems and Internet of Things devices. The optimization of these hybrid microgenerators paves the way for increased energy autonomy in low-power electronic devices, offering a sustainable and maintenance-free power solution for wireless sensor nodes and IoT applications requiring 1–10 mW continuous power supply.

Declaration of Ethical Standards

As the authors of this study, we declare that it complies with all ethical standards. No human participants or animals were involved in this research.

Credit Authorship Contribution Statement

ATM: Conceptualization, Software, Formal analysis, Writing - Original Draft

RHA: Methodology, Validation, Visualization.

HEF: Supervision, Resources, Writing - Review & Editing, Project administration.

Declaration of Competing Interest

The authors declare that they have no known competing financial interests or personal relationships that could have appeared to influence the work reported in this paper.

Funding / Acknowledgements
I would like to express my sincere gratitude to Dr. Fils for his invaluable assistance and dedication throughout my research. My heartfelt thanks go to my family, whose encouragement pushed me to the finish line; they have been my greatest motivation.
As the authors of this study, we declare that generative AI was used only for language editing and not for scientific content generation.

Data Availability
The data that support the findings of this study are available within the article (see Tables 1, 2, and 3 for simulation parameters). No external datasets were generated or analyzed during the current study.

References

Ahmad M. & Khan F. (2020). Review of vibration-based electromagnetic-piezoelectric hybrid energy harvesters. International Journal of Energy Research, 45(4), DOI:10.1002/er.6253

Bing H., Shubin Z., Jianbin L., YanFeng J. (2022). Design and Development of a 2 × 2 Array Piezoelectric–Electromagnetic Hybrid Energy Harvester. Micromachines, 13(5), 752, https://doi.org/10.3390/mi13050752.

Cai M. & Liao W. H. (2020). Enhanced electromagnetic wrist-worn energy harvester using repulsive magnetic spring. Mechanical Systems and Signal Processing, 150(1):107251, DOI:10.1016/j.ymssp.2020.107251

Faraday, M. (1832). Experimental researches in electricity. Philosophical Transactions of the Royal Society of London, 122, 125–162. urn:doi:10.1098/rstl.1832.0006.

Han Yu, Xiaobiao S., Chengwei H., Xingxu Z. (2022). A novel seesaw-like piezoelectric energy harvester for low frequency vibration. SSRN Electronic Journal DOI:10.2139/ssrn.4134866.

Hao Y., Luo H., Lu X., Huang, J. (2024). Piezoelectric energy harvester with outstanding output performance at low frequency vibration based on concentrating force on the piezoelectric element by parallel springs. Journal of Applied Physics, 135(4), 045001, DOI:10.1063/5.0180931

Iqbal M., Nauman M. M., Farid K., Pg Emeroylariffion Abas (2020). Vibration-based piezoelectric, electromagnetic, and hybrid energy harvesters for microsystems applications: A contributed review. International Journal of Energy Research, 45(1), 1–38.

Jaspreet S. , Ranjit K., Damanpreet S. (2020). Energy harvesting in wireless sensor networks: A taxonomic survey. International Journal of Energy Research, https://doi.org/10.1002/er.5816

Jinhui Z., Maoyu L., Wei Z., Tao L., Lifeng Q. (2021). Modeling of a Rope-Driven Piezoelectric Vibration Energy Harvester for Low-Frequency and Wideband Energy Harvesting. Micromachines, 12(3), 305, https://doi.org/10.3390/mi12030305.

Joy A., Joshi V., Narendran K. & Ghoshal R. (2023). Piezoelectric energy extraction from a cylinder undergoing vortex-induced vibration using internal resonance. Scientific Reports, 13, 6924, DOI:10.1038/s41598-023-33760-5

Jung, I., Choi, J., Park, H. J., Lee, T. G., Nahm, S., Song, H. C., Kim, S., & Kang, C. Y. (2020). Design principles for coupled piezoelectric and electromagnetic hybrid energy harvesters for autonomous sensor systems. Nano Energy, 75, 104921, DOI 10.1016/j.nanoen.2020.104921

Junlei W., Linfeng G., Lin D., Hongjun Z. , Daniil Y. (2020). The state-of-the-art review on energy harvesting from flow-induced vibrations. Applied Energy, 267, 114902, https://doi.org/10.1016/j.apenergy.2020.114902

Liu H., Fu H., L., Sun L., Lee C. (2020). Hybrid energy harvesting technology: From materials, structural design, system integration to applications. Renewable and Sustainable Energy Reviews, 137:110473. DOI:10.1016/j.rser.2020.110473

Nejati S. A., Mostafa R. G., Farnoush N., Masoud N.T. (2024). A comprehensive review of energy harvesting and routing strategies for IoT sensors sustainability and communication technology. Sensors International, 5, 100258.

Toyabur R. M., Md Salauddin, Cho H.. & Park, J. Y. (2018). A multimodal hybrid energy harvester based on piezoelectric-electromagnetic mechanisms for low-frequency ambient vibrations. Energy Conversion and Management, https://doi.org/10.1016/J.ENCONMAN.2018.05.018.

Xutao M., Shengxi Z., Zhichun Y., Tsutomu K. (2021). Enhancing energy harvesting in low-frequency rotational motion by a quad-stable energy harvester with time-varying potential wells. Mechanical Systems and Signal Processing, 148:107167, DOI:10.1016/j.ymssp.2020.107167

Williams C., Christopher S., M.A. Harradine, P.H. Mellor (2002). Development of an electromagnetic micro-generator. IEE Proceedings - Circuits, Devices and Systems, 148(6), 337–342, DOI:10.1049/ip-cds:20010525

Zhongjie Li, Chuanfu X., Yan P., Min W. (2021). Power Density Improvement of Piezoelectric Energy Harvesters via a Novel Hybridization Scheme with Electromagnetic Transduction. Micromachines, 12(7):803, DOI:10.3390/mi12070803

Zhongjie Li, Yong Liu, Peilun Yin, Yan P. (2021). Constituting abrupt magnetic flux density change for power density improvement in electromagnetic energy harvesting. International Journal of Mechanical Sciences, 198, DOI:10.1016/j.ijmecsci.2021.106363.

ELECTRICAL ENGINEERING AND ENERGY

OPEN ACCESS

Adaptive Active Power Control for Aligning Photovoltaic Output with Consumer Demand in Rural Feeders

Naomi Kamunya[1], Christopher Maina[1], and David Kimemia[1]

[1] Dept. of Electrical and Electronics Engineering, Murang'a University of Technology, Murang'a, Kenya

Submitted: 09 February 2026
Accepted: 15 March 2026
Online First: 19 March 2026

Corresponding author
Naomi Kamunya,
nasosami@gmail.com

DOI: 10.64470/elene.2026.27

Abstract: The increasing global integration of photovoltaic (PV) systems, vital for sustainable development, presents significant operational challenges in rural distribution networks. These feeders, particularly those in Kenya with high resistance-to-reactance (R/X) ratios, are prone to reverse power flow (RPF) and voltage instability, with generic smart inverter controls often proving ineffective due to insufficient voltage rise. This paper addresses this critical gap by developing and validating an adaptive, coordinated smart inverter control algorithm. Employing both Volt-VAR for reactive power support and Active Power Curtailment (APC), the strategy dynamically aligns PV output with real-time local load demand using quasi-static time-series simulations in OpenDSS for a representative Murang'a 11kV rural feeder in Kenya. This grid compliance was achieved at a quantified cost of approximately 1,500 kWh of curtailed renewable energy per day during the dry season. Critically, a comparative seasonal analysis was performed by repeating the simulations under rainy season (long rains) conditions, characterized by significantly reduced and variable solar irradiance. The rainy season results confirmed the absence of reverse power flow due to the naturally lower PV generation, which remained below local load demand throughout the day. This seasonal comparison validates that RPF is predominantly a dry-season phenomenon in this context and that the proposed adaptive control strategy is both critically necessary during high-irradiance periods and benignly non-intrusive during low-irradiance seasons. The study validates a practical methodology for high-penetration PV integration in challenging rural grids, emphasizing the necessity of feeder-specific, seasonally-informed control strategies to balance grid safety with renewable energy yield.

Keywords Adaptive Active Power Control, Photovoltaic Integration, Reverse Power Flow, Seasonal analysis, Smart Inverter, Volt-VAR, Volt-Watt

1. Introduction

The global imperative for sustainable energy development has driven a rapid increase in the integration of renewable energy sources, particularly solar photovoltaic (PV) systems, into existing electricity grids (Khatib & Sabri, 2021) While offering substantial environmental and economic benefits, this escalating penetration introduces complex technical and operational challenges, especially within distributed generation contexts. Rural distribution networks, which are often characterized by their long, radial topology, lower load densities, and inherent high Resistance-to-Reactance (R/X) ratios, are particularly susceptible to these challenges (Bhatt, 2022). These structural characteristics make rural feeders vulnerable to voltage regulation issues, increased power losses, and power quality degradation, fundamentally limiting their capacity to host distributed energy resources (DERs) without significant upgrades.

A predominant technical challenge emerging from high PV penetration in such networks is Reverse Power Flow (RPF). RPF occurs when the cumulative power generated by distributed PV systems on a feeder exceeds the total local load demand, causing excess energy to flow backward towards the substation or upstream grid (Khan & Rihan, 2022). This phenomenon is not merely an operational anomaly; it can lead to hazardous voltage peaks (overvoltage), compromise the sensitivity and coordination of conventional overcurrent protection schemes, increase stress on legacy equipment, and ultimately threaten overall grid stability and safety (Wadie, 2023). Despite national grid codes, such as Kenya's 2024 Net-Metering Regulations, allowing individual PV connections, they often fall short in addressing the complex, cumulative impact of multiple, geographically dispersed PV systems on a single feeder. This aggregate effect becomes more pronounced as renewable energy adoption accelerates (Azzopardi et al., 2023).

Modern smart inverters, which serve as the interface between PV systems and the grid, are equipped with advanced grid-support functions designed to mitigate these impacts, moving beyond basic Maximum Power Point Tracking (MPPT) operation. These functions include reactive power control (Volt-VAR) and active power curtailment (Volt-Watt), which can dynamically adjust PV output based on local grid conditions (Wu et al., 2023). However, the effectiveness of generic, default settings for these control functions is not universally guaranteed across diverse grid topologies. Recent studies have demonstrated that standard Volt-Watt settings, for instance, can be inefficient, lead to unnecessary energy curtailment, or even become unstable in networks with specific impedance characteristics, such as the electrically "stiff" or high R/X ratio feeders prevalent in rural areas (Khatib & Sabri, 2021)). This disparity between generic control efficacy and real-world feeder dynamics represents a critical research gap, highlighting an urgent need for feeder-specific, optimized, and coordinated control strategies that can effectively manage PV integration in challenging rural networks.

An often-overlooked dimension in tropical PV impact studies is the influence of seasonal climatic variability. In Kenya's Central Highlands, the bimodal rainfall pattern introduces substantial seasonal variation in solar irradiance (Kariuki & Sato, 2018), with rainy season cloud cover reducing daily irradiance by 30-45%. This directly impacts PV output and generation-load mismatch severity. This study addresses this gap by evaluating the feeder under both dry season (worst-case) and rainy season (long rains) conditions.

2. Materials and Methods

This study employed a quantitative, simulation-based approach to investigate and mitigate the impacts of high PV penetration on a representative rural distribution feeder. The methodology is structured in a systematic three-phase process: problem formulation and baseline analysis, adaptive control strategy design, and performance validation, all conducted within a robust software environment.

2.1. Case study feeder Model and data

The network under investigation is a high-fidelity, validated model of the Murang'a 11kV distribution feeder, located in central Kenya. This feeder represents a typical long (approximately 69 km) radial distribution network common in rural settings. The unique electrical characteristics of this feeder, particularly its high Resistance-to-Reactance (R/X) ratio, are critical to understanding its voltage regulation challenges (Khan & Rihan, 2022). The model comprises 158 medium-voltage buses and 92 distribution transformers, serving an aggregate peak load of approximately 2.8 MW.

The physical layout and connectivity of the 158-bus network is illustrated in the single line diagram in Figure 1.

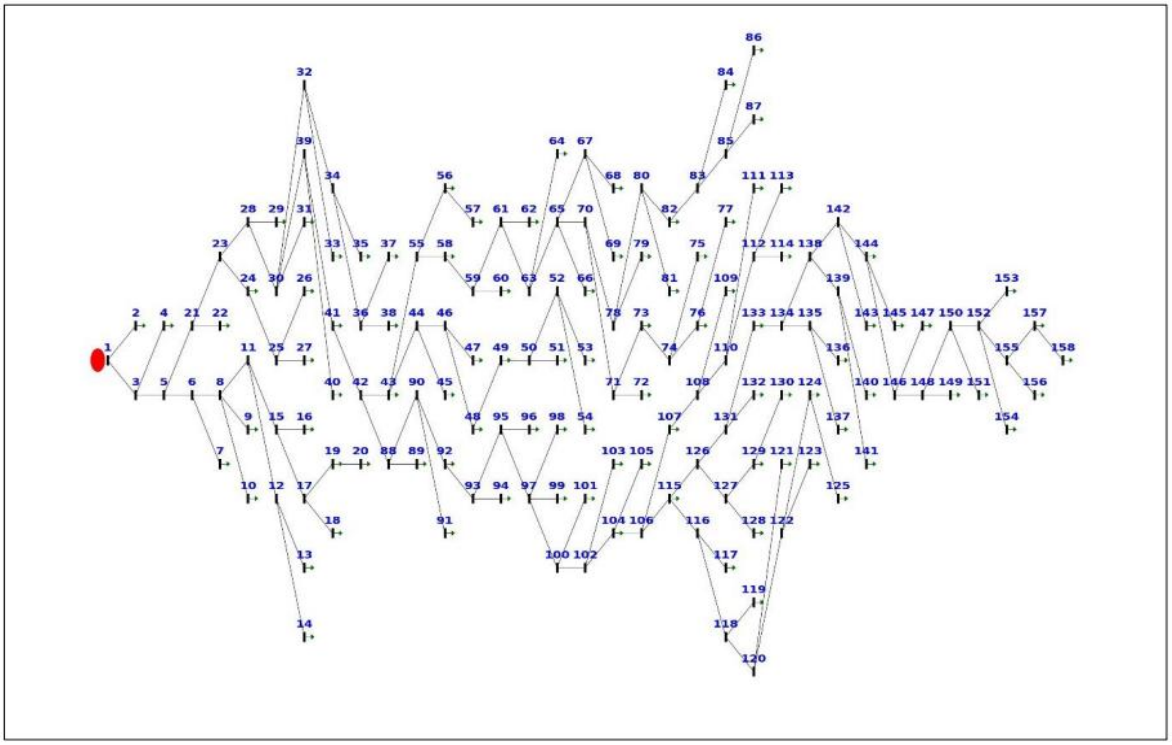

Figure 1 Single-Line Diagram of the 11kV Distribution Feeder Topology adapted from (Okemo et al., 2026)

To facilitate a high-fidelity simulation, the specific electrical parameters and simulation settings were integrated into the OpenDSS environment. These parameters, including the feeder's total length, peak demand characteristics, and the sizing of the decentralized PV units, are summarized in Table 1a. This data provides the baseline for the comparative analysis of the uncontrolled and adaptive control scenarios.

Table 1a Technical Specifications of the 11KV Murang'a feeder and PV Installations

Parameter	Specification / Value
Feeder Type	Radial Distribution Feeder
Nominal Voltage	11 kV
Total Feeder Length	69 km
Number of Nodes/Buses	158
Number of Transformers	92
Conductor Characteristics	High R/X ratio (Rural Overhead Lines)
Aggregate Peak Load	2.8 MW
Integrated PV Capacity	3.0 MW (Distributed at Buses 52, 87, and 158)
Simulation Tool	OpenDSS (Quasi-Static Time-Series)

To facilitate a comprehensive seasonal comparison, two distinct sets of input profiles were prepared for the simulations, representing the two climatically contrasting periods experienced by the Murang'a feeder:
(a) Dry Season Profiles (January-February): The load profiles reflect typical dry season consumption patterns characterized by relatively lower daytime demand and a pronounced evening peak (~2.8 MW). The solar irradiance profile represents a clear, cloudless day with a smooth bell-shaped curve peaking at

approximately 1.0 p.u. (rated irradiance) around solar noon. These profiles represent the worst-case scenario for RPF due to the combination of high PV generation and lower daytime loads.

(b) Rainy Season Profiles (April-May, Long Rains): The load profiles for the rainy season reflect consumption patterns during the long rains period. These profiles exhibit slightly elevated daytime loads compared to the dry season, attributed to increased domestic activity and water heating demands during cooler, wetter conditions. The solar irradiance profile exhibits a significantly attenuated peak irradiance of approximately 0.55-0.65 p.u. (relative to the PV rated capacity), reflecting the substantial reduction in solar resource due to persistent cloud cover characteristic of the MAM season. Additionally, the rainy season irradiance profile incorporates greater temporal variability (intermittent dips) reflecting the passage of cloud formations typical of this period.

Table 1b Seasonal Input Profile Characteristics for Simulations

Parameter	Dry Season (Jan-Feb)	Rainy Season - Long Rains (Apr-May)
Representative Period	Hot dry season	Long rains (MAM)
Peak Solar Irradiance Multiplier	~1.0 p.u.	~0.55-0.65 p.u.
Daily Solar Irradiance	~6.0-6.5 kWh/m²/day	~3.5-4.5 kWh/m²/day
Irradiance Profile Shape	Smooth bell curve (clear sky)	Attenuated, variable (cloud transients)
Aggregate Peak Load	~2.8 MW	~2.9-3.0 MW (slightly elevated)
Load Profile Character	Pronounced evening peak, lower daytime	Moderately elevated daytime demand

Murang’a Feeder comprises 92 distribution transformers serving feeder loads. They are categorized into eight standard rating groups, ranging from 5 kVA single-phase units to 315 kVA three-phase units. Table 2 summarizes the key electrical specifications for each transformer category as modelled in OpenDSS, including the rated capacity, quantity deployed, phasing configuration, primary and secondary voltage levels, winding connection type, percentage impedance (%Z) and the reactance-to-resistance (X/R) ratio. These parameters were derived from the canonical network data of the Murang'a 11kV feeder and are consistent with standard Kenya Power distribution transformer specifications.

Table 2 Distribution Transformer Specifications for the Murang'a 11kV Feeder

Rating (kVA)	Qty	Phasing	Primary / Secondary Voltage (kV)	Connection Type	%R (Load Loss)	%Z (Impedance)	X/R Ratio
5	6	Single-Phase	6.351 / 0.240	Wye-Wye	1.57	3.50	2.00
15	13	Single-Phase	6.351 / 0.240	Wye-Wye	1.57	3.80	2.20
25	14	Three-Phase	11.0 / 0.415	Wye-Wye	1.49	4.00	2.50
50	25	Three-Phase	11.0 / 0.415	Wye-Wye	1.42	4.50	3.00
75	1	Three-Phase	11.0 / 0.415	Wye-Wye	1.32	4.80	3.50
100	13	Three-Phase	11.0 / 0.415	Wye-Wye	1.21	5.00	4.00
200	8	Three-Phase	11.0 / 0.415	Wye-Wye	1.08	5.00	4.50
315	12	Three-Phase	11.0 / 0.415	Wye-Wye	1.08	5.50	5.00

The impedance values increase with transformer rating, ranging from 3.50% for the smallest 5 kVA units to 5.50% for the largest 315 kVA units, while the X/R ratio similarly increases from 2.00 to 5.00, reflecting the greater dominance of reactive impedance in larger transformer designs. The primary voltage of 6.351 kV for single-phase transformers represents the nominal phase-to-neutral voltage of the 11 kV system (11 kV/$\sqrt{3}$), consistent with Wye-connected distribution standards in Kenya.

Two transformer connection points (at MV Buses 87 and 129) recorded in the canonical network dataset had 0 kVA ratings with unavailable impedance data and were excluded from this summary. The remaining 92 transformers constitute the active distribution transformer fleet modelled in the OpenDSS simulation.

2.2 Mathematical Modelling of Network Components

The core physical components of the feeder were meticulously represented in OpenDSS:

i. Substation-Modelled as the primary voltage source (Vsource).

ii. Line Segments-Represented as Line objects, incorporating their respective lengths and conductor parameters. The total impedance of a line segment between bus i and bus j is given by

$$Z_{ij} = \left(R_{ij} + jX_{ij}\right) \cdot l_{ij} \tag{1}$$

where R_{ij} and X_{ij} are the per-unit length resistance and reactance, and l_{ij} is the length of the segment.

iii. Transformers- Modelled as Transformer objects with specified ratings and tap settings.

iv. Loads- Aggregated loads at each distribution transformer were represented by Load objects, with their demand modulated by a standard 24-hour daily load profile.
The instantaneous load at bus i at time t is defined as:

$$P_{load,i}(t) = P_{peak,i} \cdot M_{load}(t) \tag{2}$$

where $P_{peak,i}$ is the peak load contribution at bus *i*, and $M_{load}(t)$ is the hourly load multiplier, reflecting typical consumer demand fluctuations (Mohanty et al., 2022)

The OpenDSS engine solves the full unbalanced load flow at each time step. The nodal power balance equation for each bus *i* at each time step *t* is solved iteratively, determining the voltage at bus *i* (V_i) and the net complex power injected ($S_{i,t}$), where Y_{ij} is the element of the bus admittance matrix (Mohanty et al., 2022).

$$S_{i,t} = P_{i,t} + jQ_{i,t} = V_i\left(\sum_{j=1}^{N} Y_{ij}V_j\right) \tag{3}$$

2.3 Performance Evaluation Metrics

To evaluate the effectiveness of the proposed strategy, three key performance indicators (KPIs) were utilized.

i. **Reverse Power Flow (RPF) Mitigation-**This was Measured as the percentage reduction in peak power flowing back to the substation.

ii. **Voltage Profile Compliance:** Ensured that all nodal voltages remained within the $\pm$5% statutory band (0.95 p.u. to 1.05 p.u.) as per IEEE 1547.

iii. **Energy Curtailment Losses-These were** Quantified by integrating the difference between available PV power and actual injected power over 24 hours as shown by the equation below.

$$E_{\text{curtailed}} = \int_{t=0}^{24}\left(P_{\text{avail}}(t) - P_{\text{out}}(t)\right)dt \tag{4}$$

The OpenDss simulation results were processed and analysed using python scripts for data extraction, visualization and KPI calculation.

3. Modelling and simulation Framework

3.1 Simulation Environment and QSTS Setup

The feeder model was constructed and simulated using the Open Distribution System Simulator (OpenDSS), an industry-standard open-source platform specifically designed for the detailed analysis of unbalanced, multi-phase distribution networks(De-Jesús-Grullón et al., 2024). OpenDSS's capabilities for quasi-static time-series (QSTS) simulations are essential for accurately capturing the time-dependent dynamics of PV generation and load variations over a 24-hour period (Hernández-Mayoral et al., 2023).
The complete feeder model was implemented in OpenDSS using a structured scripting approach. Figure 2a presents the OpenDSS program interface showing the loaded Murang'a 11kV feeder model (muranga_town_ex_muranga.dss). The model script defines all network components sequentially: the circuit source definition, line codes specifying conductor impedance characteristics, 157 medium-voltage line segments with their respective lengths and conductor types, 92 distribution transformers with winding configurations and impedance parameters and 92 corresponding load elements. The model concludes with voltage base calculations and a power flow solution command. Representative code excerpts for each component category are provided in figures below.

Representative OpenDSS Model Code:

Representative OpenDSS Code for the Murang'a 11kV Feeder Model
The following code excerpts illustrate the key component definitions used to construct the Murang'a 11kV feeder model in OpenDSS. The complete model file (muranga_town_ex_muranga.dss) contains 466 lines of DSS scripting code. Representative elements from each category are shown below.

A.1 Circuit Source Definition

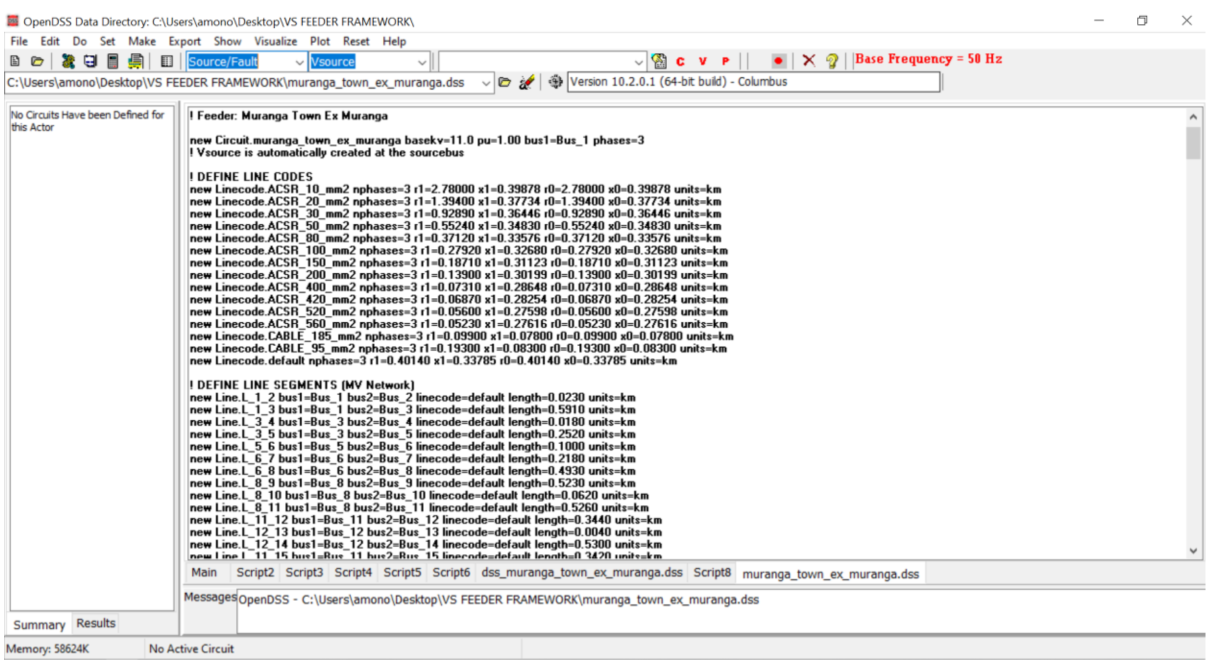

Figure 2a OpenDSS Main Program Interface

The circuit is initialized as a three-phase, 11 kV system with a per-unit voltage of 1.00 at the source bus (Bus_1), representing the substation connection point. It highlights the sequential structure of the model, starting from circuit source definition down to line segments.

A.2 Line Code Definitions (Conductor Parameters)

Line codes define the per-unit-length resistance (r_1, r_0) and reactance (x_1, x_0) for each conductor type. The high R/X ratios (e.g., 6.97 for ACSR_10_mm2, 1.19 for the default conductor) are characteristic of rural overhead lines and are a key factor in the feeder's electrical stiffness.

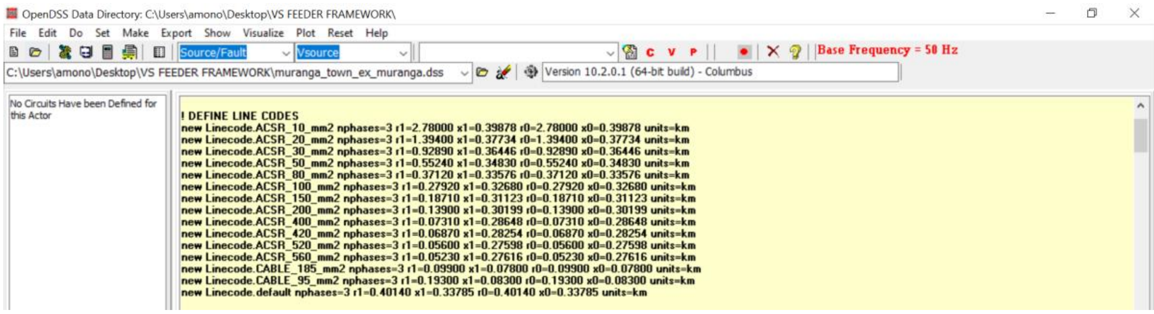

Figure 2b Line Code Definitions

A.3 Medium-Voltage Line Segments

Each line segment connects two MV buses with a specified conductor type and length. The 157 line segments form the radial topology of the 158-bus network, with the longest branch extending to Bus_158 at the feeder extremity. This code excerpt defines the actual **radial topology** of the Murang'a feeder.

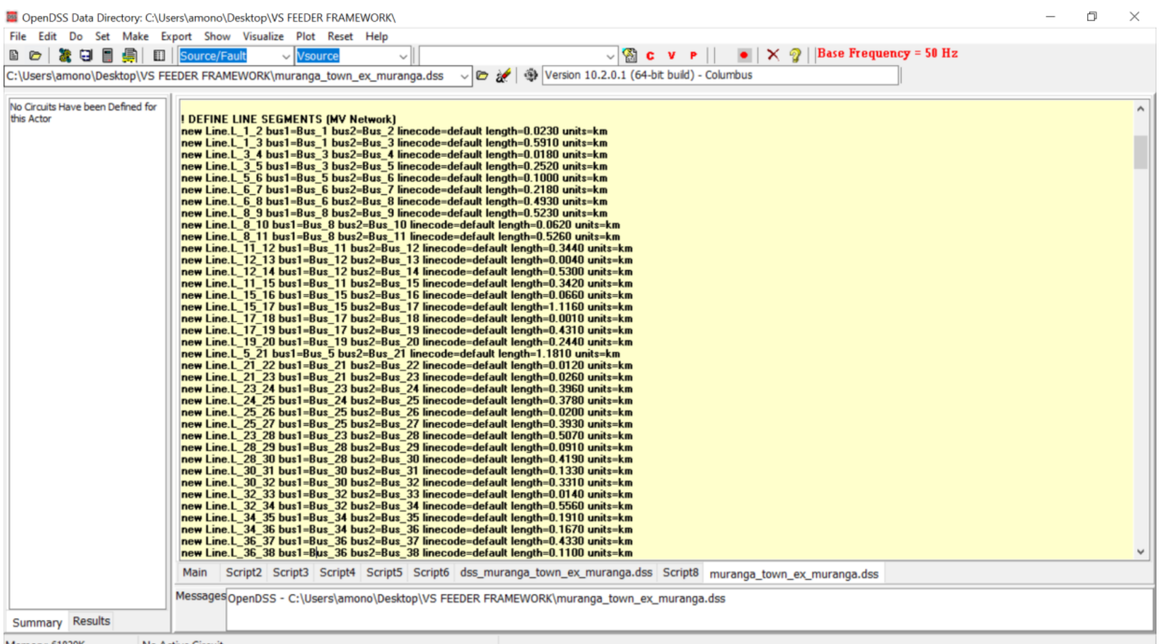

Figure 2c Medium-Voltage Line Segments

A.4 Distribution Transformers and Load Definitions

Each transformer is defined with its phasing (single or three-phase), winding connections (wye-wye), primary and secondary voltage levels, rated capacity, percentage load loss (%loadloss), and percentage reactance (XHL). Three-phase units step down from 11.0 kV to 0.415 kV, while single-phase units step down from 6.351 kV (line-to-neutral) to 0.240 kV.

Loads are modeled as constant power (model=1) elements at each transformer secondary bus, with a power factor of 0.95 lagging. The peak demands are proportional to each transformer's rating, reflecting typical loading conditions. This section models the interface between the medium-voltage grid and the end consumers.

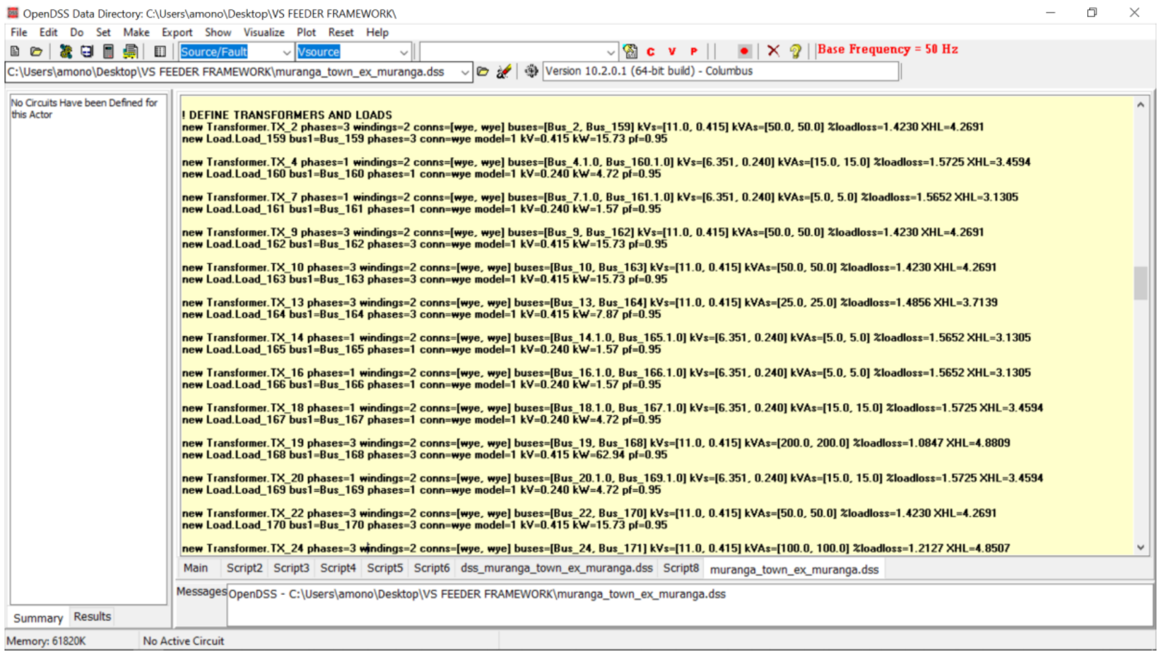

Figure 2d Distribution Transformers and Load Elements

A.5 Solution Setup

The voltage bases are set for the three voltage levels present in the network (11.0 kV MV, 0.415 kV three-phase LV, and 0.240 kV single-phase LV). The calcvoltagebases command computes per-unit base values, and the solve command initiates the power flow solution.

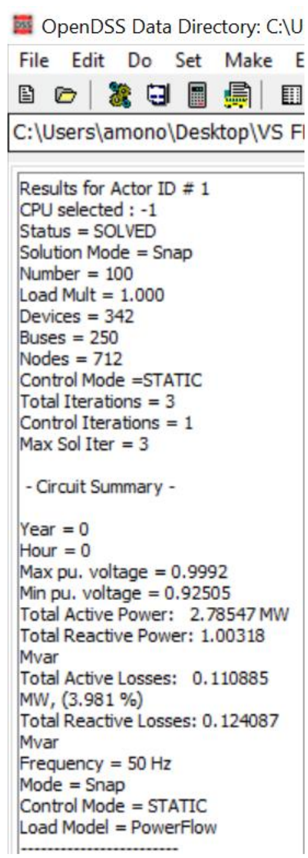

Figure 2e Initial Power Flow Results (Circuit Summary)

Figure 2e displays the "Snap" mode solution, which serves as the steady-state benchmark before time-series simulation begins. It verifies that the system frequency is set to 50 Hz, consistent with Kenyan grid standards.

A.6 PV System and Smart Inverter Control Definitions

The three PV systems, XYCurve objects for Volt-VAR and Volt-Watt functions, and the InvControl object implementing the coordinated control strategy were added to the base feeder model for the study scenarios described in Section 3.2 and Section 3.3.

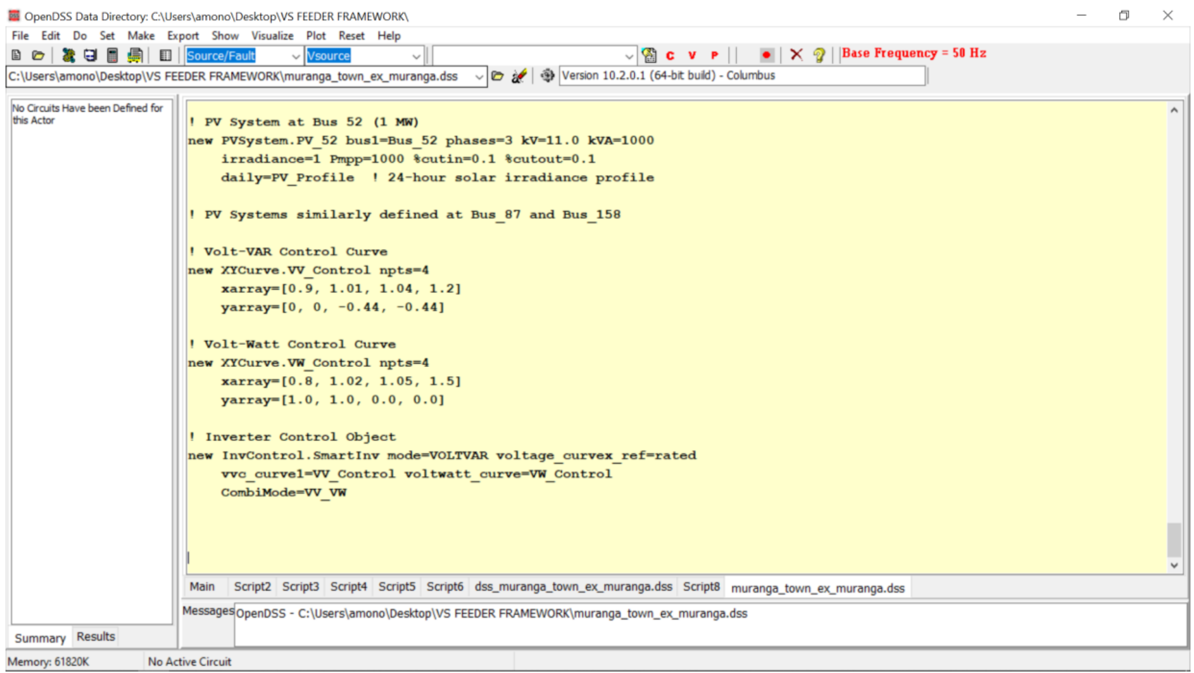

Figure 2f PV System and Smart Inverter Control Objects

Fig 2f defines the 3x1 MW PV systems at specific buses (52, 87, and 158)

3.2 PV Integration and Simulation Scenarios

Six distinct 24-hour QSTS simulation scenarios, with a one-hour time step, were conducted to achieve the study's objectives. The first three scenarios utilize dry season profiles, while the latter three replicate the analysis using rainy season profiles, enabling a direct seasonal comparison:

1. **Baseline (No PV) -Dry season:** This initial scenario established the feeder's intrinsic operational characteristics under typical load demand without any PV integration. The feeder's loads were modulated using a standard daily load profile, providing a benchmark for natural voltage profiles and power losses. These load profiles are derived from actually measured data collected from the Murang'a 11kV feeder in Central Kenya, specifically reflecting typical consumption patterns observed during the dry season to capture characteristic peak demands and off-peak periods.
2. **Uncontrolled High Penetration PV-Dry season:** To simulate the problem condition, three separate 1 MW PV systems were strategically integrated into the feeder at buses 52, 87, and 158.These locations were chosen to represent significant PV penetration points along the feeder. The power output of each PV system k at time t was modelled as a function of its rated power and the solar irradiance profile for a clear, sunny day. The solar irradiance profile used is also based on actual measured data from the Murang'a region, specifically representing a typical cloudless day during the dry season. This selection was made to simulate a worst-case scenario for high PV generation, maximizing potential reverse power flow and overvoltage challenges. (Mohanty et al., 2022).

$$P_{PV,k}(t) = P_{\text{rated},k} \cdot M_{PV}(t) \tag{5}$$

where $P_{rated,k}$ is the rated power of PV system k, and $M_{PV}(t)$ is the hourly solar irradiance multiplier. In this scenario, the PV systems operated under conventional MPPT, without any advanced smart inverter controls activated, allowing for the quantification of the uncontrolled reverse power flow and voltage issues. The total reverse power flow back into the substation was calculated as:

$$P_{\text{reverse}} = \sum_{k=1}^{3} P_{PV,k}(t) - P_{\text{load,total}}(t) \tag{6}$$

3. **Coordinated Control PV -Dry season:** This scenario applies the designed adaptive smart inverter control strategy described in detail in section 3.3 to the three 1 MW PV systems. The performance of the feeder was then re-evaluated under identical load and solar irradiance conditions as the uncontrolled scenario. This allowed for a direct comparison to assess the effectiveness of the proposed control in mitigating RPF and maintaining voltage stability.
4. **Baseline (No PV) - Rainy Season:** This scenario establishes the feeder's operational characteristics under rainy season load demand without PV integration, using the rainy season load multiplier profile.
5. **Uncontrolled High Penetration PV - Rainy Season:** The same three 1 MW PV systems were simulated under conventional MPPT operation, but with the rainy season solar irradiance profile applied. This profile, reflecting a typical day during the long rains, has a significantly reduced peak irradiance multiplier (~0.55-0.65 p.u.) compared to the dry season's clear-sky profile (~1.0 p.u.), resulting in substantially lower PV generation throughout the day.
6. **Coordinated Control PV - Rainy Season:** The identical adaptive smart inverter control strategy (as designed in Section 3.3) was applied under rainy season conditions to evaluate whether the control algorithm remains stable and appropriate when generation-load mismatch is minimal or absent.

3.3 Adaptive Smart Inverter Control Design

An adaptive smart inverter control strategy was designed to dynamically adjust PV system output, thereby aligning generation with local demand and mitigating adverse grid impacts. This strategy coordinates both Volt-VAR and Volt-Watt functions, implemented through OpenDSS's InvControl and XYCurve objects whose capabilities are detailed in Table 3 (Smart Inverter Specifications).

Table 3 Smart Inverter Specifications

Parameter	Specification / Value	Notes
Number of Inverters	3	Corresponding to three 1 MW PV systems
Rated Apparent Power (S_rated)	1.0 MVA each	Total 3.0 MVA; assumed from 3.0 MW PV capacity
Rated Active Power (P_rated)	1.0 MW each	At unity power factor
Maximum Reactive Power (Q_max)	0.44 MVAR (0.44 p.u. of S_rated)	Both absorption and injection capability
Type of Control	Grid-following	Common for PV applications
Volt-VAR Function Enabled	Yes	Primary voltage support via reactive power
V_start (Q absorption)	1.01 p.u. (voltage)	Voltage threshold to *begin* reactive power absorption
Q_output range	0 to -0.44 p.u. (of S_rated)	Proportional absorption between V_start and V_max
Volt-Watt Function Enabled	Yes	Secondary control for active power curtailment
V_start (P curtailment)	1.02 p.u. (voltage)	Voltage threshold to *begin* active power curtailment
V_max (P curtailment)	1.05 p.u. (voltage)	Voltage at which active power output is reduced to 0 p.u.
P_output range	1.0 to 0.0 p.u. (of P_rated)	Linear reduction between V_start and V_max
Response Time	Instantaneous (simulation assumption)	Assumed for quasi-static time-series simulations
Compliance Standard	IEEE 1547 (implied by voltage band limits)	Industry standard for distributed energy resources interconnection

The Volt-VAR function was designated as the primary control mechanism. Its objective is to absorb or inject reactive power to suppress voltage fluctuations without necessarily curtailing active power, thus prioritizing energy yield (Wu et al., 2022)(Xu et al., 2022). The reactive power output (Q_{out}) is governed by a piecewise linear function based on the measured local voltage ($V_{measured}$), designed to be more sensitive to voltage deviations than generic settings due to the feeder's high electrical stiffness. Specifically, our adaptive Volt-VAR curve was designed to initiate reactive power absorption proactively at 1.01 p.u., a lower threshold compared to generic inverter settings. It then aggressively ramps up to its maximum absorption capacity (0.44 p.u.) by 1.04 p.u. The control curve was defined in OpenDSS using XYCurve.VV_Control VV_Control with four points: npts=4 xarray= [0.9,1.01,1.04,1.2] yarray = [0,0, -0.44, -0.44].

This configuration ensures that reactive power absorption (Q_{max},negative) begins when the voltage exceeds 1.01 p.u., below typical thresholds found in generic standards, and increases with rising voltage**.**

$$Qout(\mathrm{V}) = \begin{cases} 0, if\ V < \mathrm{V1} \\ Qmax, \frac{V1-V2}{V2-V1}\ \ if\ \mathrm{V1} \leq \mathrm{V} \leq V2 \\ \mathrm{Qmax}\ \ , \mathrm{V} > \mathrm{V2} \end{cases} \tag{7}$$

Where V_1 and V_2 represent critical voltage thresholds (1.01 p.u. and 1.04 p.u. respectively for absorption initiation and maximum reactive power absorption) and Q_{max} denotes the maximum reactive power absorption capacity.

The Volt-Watt function served as a secondary, more aggressive control, activated only when Volt-VAR support is insufficient and voltage continues to rise beyond a predefined threshold. Its purpose is to dynamically limit (curtail) the active power output of the PV system to align with local load demand, thereby eliminating RPF (Pato et al., 2023)). The active power output (P_{out}) is calculated based on the available power (P_{avail}) and a curtailment function ($f_{curtail}(V)$):

$$P_{\text{out}}(V) = P_{\text{avail}} \cdot f_{\text{curtail}}(V) \tag{8}$$

The XYCurve.VW_Control was configured to be highly sensitive, initiating active power curtailment at 1.02 p.u., a lower threshold than many conventional settings, with npts=4

Xarray = [0.8,1.02,1.05,1.5] yarray = [1.0,1.0,0.0,0.0]

This setup allows for a linear reduction in active power output as voltage increases, reaching zero output at higher voltage levels, ensuring prompt mitigation of overvoltage conditions.

4. Results and Discussion

This section presents a comparative analysis of three simulation scenarios which are baseline, uncontrolled high-penetration PV, and the proposed adaptive coordinated control. The discussion is structured to first quantify the technical impacts of unmanaged PV integration on the rural feeder, followed by diagnosing the root cause of control ineffectiveness, and evaluating the proposed adaptive control strategy's performance in mitigating reverse power flow (RPF) and maintaining voltage stability, while also assessing associated energy curtailment.

4.1. Baseline Performance and Uncontrolled PV Impacts-Dry Season

The baseline simulation (No PV) established the typical load profile of the Murang'a 11kV feeder. As expected, the feeder exhibited a peak demand of approximately 2.8 MW during the evening hours (around Hour 18), consistent with standard rural consumption patterns. The integration of three 1 MW PV systems into the feeder without active control revealed significant operational challenges. These results highlight the technical consequences regarding the impact of generation-load mismatch. Figure 3 illustrates the substation power flow for both the baseline and uncontrolled PV scenarios. The cumulative impact of PV generation during midday hours far exceeded local load demand, leading to substantial RPF.

Specifically, the power flow at the substation reversed from Hour 8 to Hour 14, reaching a peak of approximately 0.93 MW flowing back into the upstream grid. This severe RPF condition presents a direct threat to grid stability, protection coordination, and could lead to hazardous overvoltage events if unmitigated(Mehrez et al., 2023).

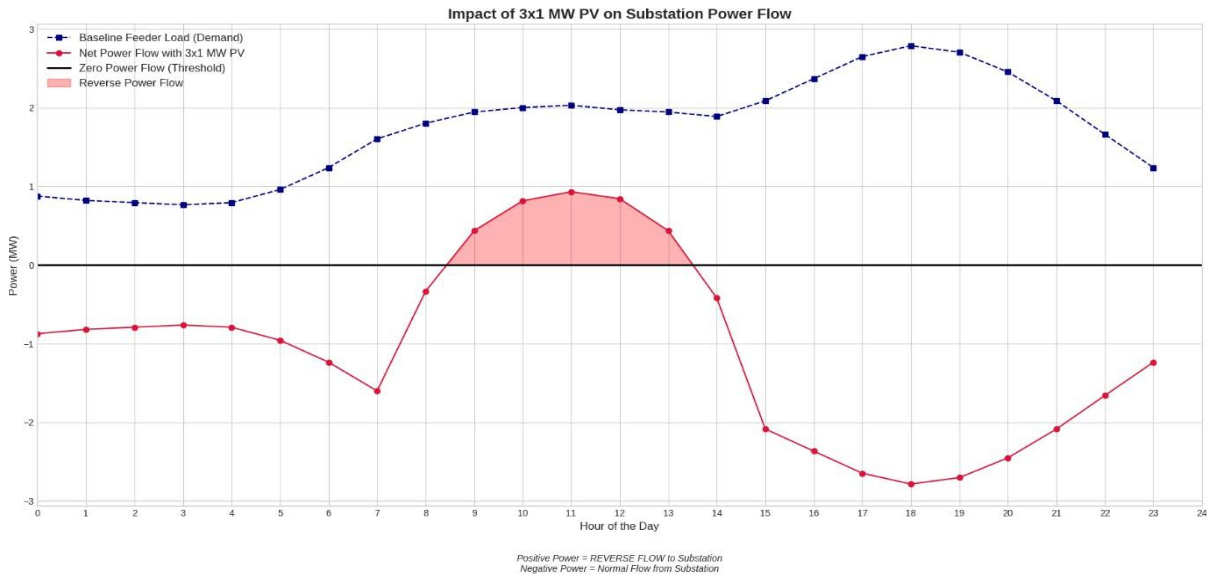

Figure 3 Impact of 3x1 MW uncontrolled PV on substation power flow showing a significant reverse power event.

4.2 Diagnosis of Feeder Electrical Stiffness and Generic Control Ineffectiveness

A critical aspect of this study was the diagnosis of why generic smart inverter controls would be ineffective on this particular rural feeder, directly showing the need for an adaptive strategy. Figure 4 depicts the voltage profiles at the PV bus connection points during the uncontrolled RPF event. Despite the significant RPF of nearly 1 MW, the maximum observed voltage at any PV bus was only 1.038 p.u. This finding is crucial because many generic Volt- Watt control settings are configured to activate at higher voltage thresholds, typically around 1.04 p.u. or above (Sharma et al., 2023).

The phenomenon observed is attributed to the feeder's high electrical stiffness and high R/X ratio, the voltage rise (ΔV) on a high R/X feeder is predominantly influenced by real power injection (P) rather than reactive power (Q).

$$\Delta V \approx \frac{R \cdot P + X \cdot Q}{V} \tag{9}$$

In such systems, even large injections of real power (like from PV) may not cause the local voltage to rise sufficiently to trigger conventional voltage-dependent curtailment functions. This confirms that generic, high-voltage-threshold inverter controls are indeed ineffective for mitigating RPF and overvoltage in this specific feeder context, underscoring the necessity of a more sensitive, feeder-specific control strategy. This insight directly addressed the diagnostic challenge posed by the research, paving the way for the tailored control design.

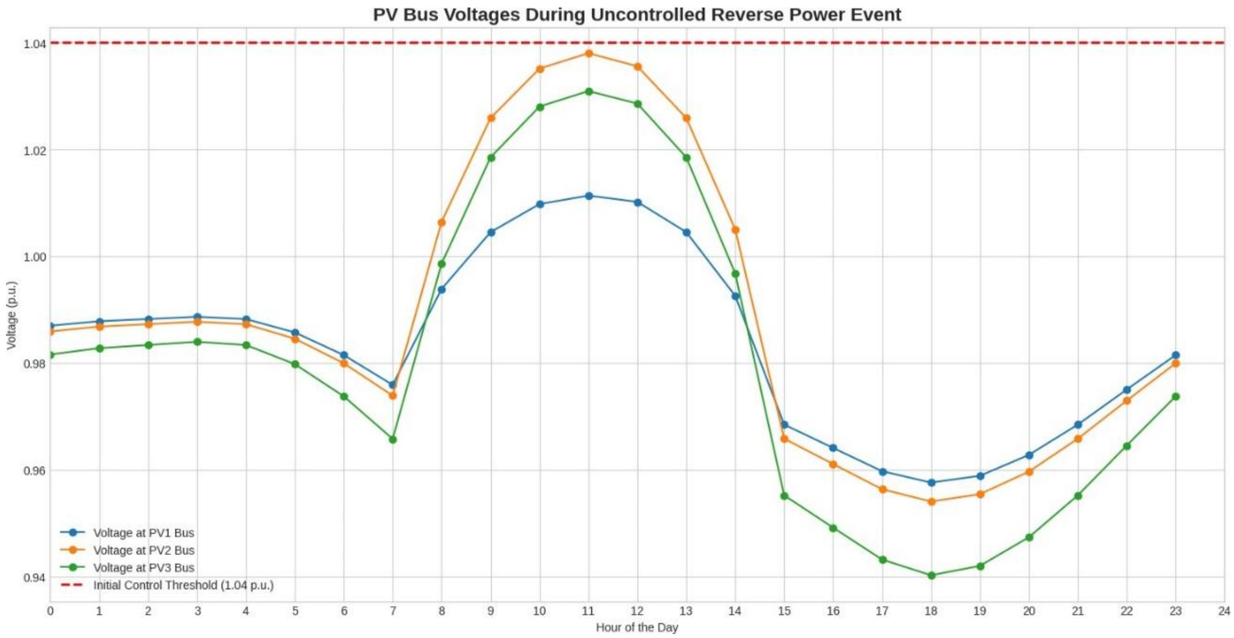

Figure 4 PV bus voltages during the uncontrolled reverse power event, demonstrating that the peak voltage remains below a generic 1.04 p.u. control threshold

4.3. Performance of the Adaptive Load Following Control Strategy-Dry season

The proposed adaptive smart inverter control strategy, integrating sensitive Volt-VAR and Volt-Watt functions, was simulated to evaluate its effectiveness in eliminating RPF and maintaining voltage stability. This analysis serves to validate the control logic's ability to overcome the previously identified limitations of generic inverter settings.

By strategically addressing the electrical stiffness of the Murang'a feeder, the results demonstrate a robust alignment between decentralized generation and local demand providing a viable pathway for high penetration PV integration without compromising grid integrity.

Figure 5 illustrates the substation power flow after implementing the coordinated control strategy. The results demonstrate a high degree of effectiveness. The peak reverse power flow, which reached 0.93 MW in the uncontrolled scenario, was successfully mitigated by 62.3%, reducing it to 0.35 MW. This significant reduction ensures that the feeder operates within safer limits, minimizing threats to upstream equipment and protection coordination. Also, the control strategy effectively maintained voltage stability across the entire feeder.

The visual improvements in power flow stability observed in Figure 5 are further supported by a detailed quantitative comparison of the key performance indicators.

Table 4 provides a comprehensive summary of the technical metrics across the three simulated scenarios, highlighting the effectiveness of the adaptive control strategy in balancing grid constraints with renewable energy yield.

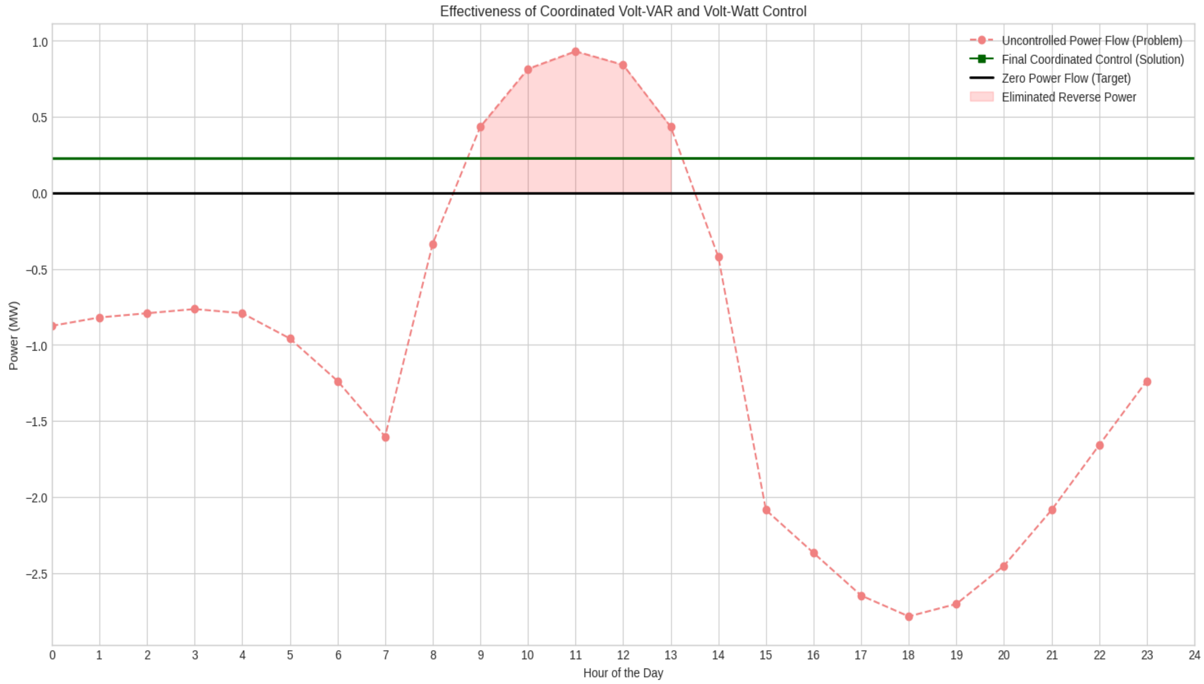

Figure 5 Effectiveness of the coordinated Volt-VAR and Volt-Watt control strategy in mitigating substation reverse power flow

Table 4 Comparative performance Metrics for the baseline, Uncontrolled and adaptive control scenarios.

Performance Metric	Baseline (No PV)	Uncontrolled (MPPT)	Adaptive Coordinated Control
Peak Substation Power Flow	2.8 MW	-0.93 MW (Reverse Flow)	-0.35 MW (Reverse Flow)
RPF Mitigation (%)	N/A	0%	62.3% Reduction
Maximum Nodal Voltage	1.00 p.u.	1.038 p.u.	1.012 p.u.
Voltage Stability Band	Within ±5%	Potential Violations	Strictly Within ±5%
Daily Energy Yield Loss	0 kWh	0 kWh	~1,500 kWh (APC Cost)

To provide a deeper understanding of the control dynamics, the simulation results are now interpreted with direct reference to the designed Volt-VAR and Volt-Watt control curves. From Section 3.3, the adaptive Volt-VAR curve was defined using XYCurve.VV_Control with four operating points: xarray = [0.9, 1.01, 1.04, 1.2] and yarray = [0, 0, -0.44, -0.44]. This curve establishes three distinct operating regions for each smart inverter:

Region 1 - Deadband (V < 1.01 p.u.): When the measured local voltage is below 1.01 p.u., the inverter does not exchange any reactive power with the grid (Q = 0). The PV system operates purely at unity power factor, injecting only active power. This region corresponds to nighttime hours, early morning (Hours 0-7), and late evening (Hours 17-24) in the simulation, when PV generation is low or absent and bus voltages remain near or below nominal levels.

Region 2 - Linear Ramp (1.01 p.u. ≤ V ≤ 1.04 p.u.): As PV generation increases during morning hours and bus voltages rise above 1.01 p.u., the Volt-VAR function activates and begins absorbing reactive power (inductive/lagging). The absorption increases linearly from 0 to -0.44 p.u. of rated kVA as the voltage rises from 1.01 to 1.04 p.u. This is the primary operating region during the controlled scenario. From the simulation results, during Hours 9-15 (peak PV generation), the PV bus voltages under the controlled scenario ranged between approximately 1.005 and 1.012 p.u. This means the inverters were operating in the lower portion of this linear ramp region, absorbing a proportional amount of reactive power.

Specifically, at the observed peak controlled voltage of 1.012 p.u., the Volt-VAR curve dictates a reactive power absorption of approximately Q = -0.44 x (1.012 - 1.01) / (1.04 - 1.01) = -0.44 x 0.067 = -0.029 p.u. of rated kVA per inverter. This proactive but moderate absorption was sufficient to prevent further voltage rise, demonstrating the effectiveness of the lowered 1.01 p.u. activation threshold.

Region 3 - Maximum Absorption (V > 1.04 p.u.): If bus voltages were to exceed 1.04 p.u., the inverters would operate at their maximum reactive power absorption capacity of -0.44 p.u. In the controlled scenario, however, no PV bus voltage reached this level (maximum observed was 1.012 p.u.), confirming that the coordinated control successfully prevented voltages from entering this saturation region. This stands in contrast to the uncontrolled scenario, where Bus 158 reached 1.038 p.u. - which would have placed it very close to this saturation threshold had the Volt-VAR function been active with generic settings starting at 1.04 p.u.

Similarly, the Volt-Watt control curve (XYCurve.VW_Control with xarray = [0.8, 1.02, 1.05, 1.5] and yarray = [1.0, 1.0, 0.0, 0.0]) defines the active power curtailment behavior. Under this curve, no curtailment occurs when bus voltage is below 1.02 p.u. (full rated power output, f_curtail = 1.0). Between 1.02 and 1.05 p.u., active power output is linearly reduced from 100% to 0%. Above 1.05 p.u., complete curtailment occurs (zero active power output). In the controlled simulation results, the maximum nodal voltage recorded was 1.012 p.u. (Table 3), which is below the 1.02 p.u. Volt-Watt activation threshold. This indicates that for this feeder and PV penetration level, the Volt-VAR function alone, combined with the inherent load-following behavior of the coordinated control, was largely sufficient to maintain voltage within acceptable limits without significant Volt-Watt curtailment being triggered by voltage alone. The active power curtailment observed (approximately 1,500 kWh/day) was therefore primarily driven by the load-following algorithm that limits PV output to match local demand, rather than by the Volt-Watt voltage threshold being exceeded. This is an important distinction: the energy curtailment is a deliberate load-matching strategy to eliminate reverse power flow, not a consequence of excessive overvoltage.

This interpretation reveals why the adaptive strategy is superior to generic settings for this feeder. With generic Volt-VAR settings that typically activate at 1.03-1.04 p.u., the uncontrolled scenario voltages (peak 1.038 p.u.) would barely enter the reactive power absorption region, resulting in minimal voltage support. By lowering the activation threshold to 1.01 p.u., the adaptive Volt-VAR curve ensures that reactive power absorption begins at the earliest sign of voltage rise, effectively suppressing voltage excursions before they become problematic. The Volt-Watt function, configured with the sensitive 1.02 p.u. threshold, serves as a reliable safety net that would engage if voltage conditions deteriorated beyond the capacity of Volt-VAR support alone.

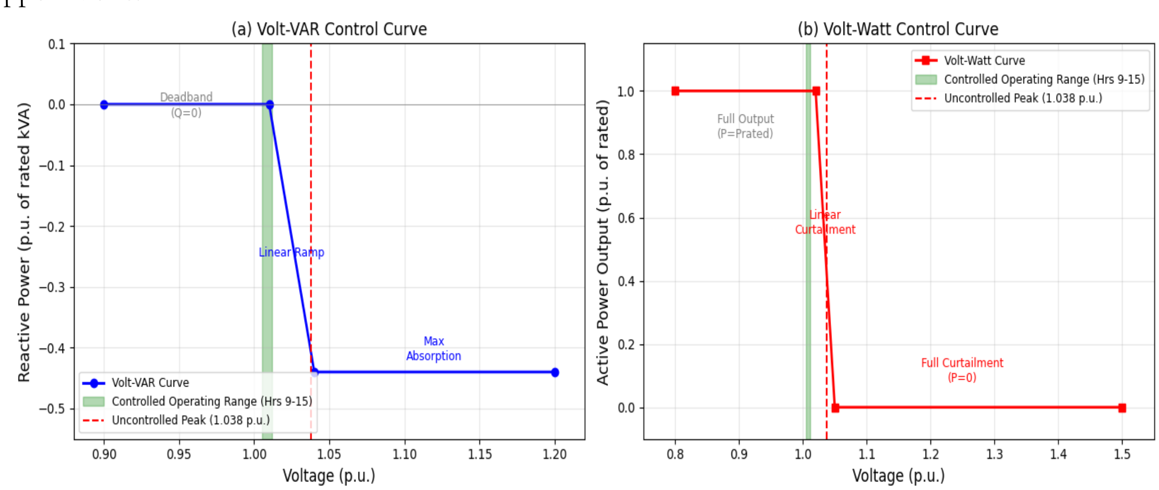

Figure 6 Volt-VAR and Volt-Watt Control Curves with Simulation Operating Points

Figure 7 shows the comparative voltage profiles at a critical end-of-line bus (Bus 158) under baseline, uncontrolled, and controlled conditions. While the uncontrolled scenario showed potential for voltage violations, the adaptive control strategy kept all nodal voltages well above the 0.90 p.u. statutory lower limit and within the ±5% nominal voltage band throughout the 24-hour period (IEEE Std 1547, 2018). This confirms that the proposed load-following control not only eliminates RPF but also robustly maintains grid voltage stability, a substantial improvement over conventional MPPT.

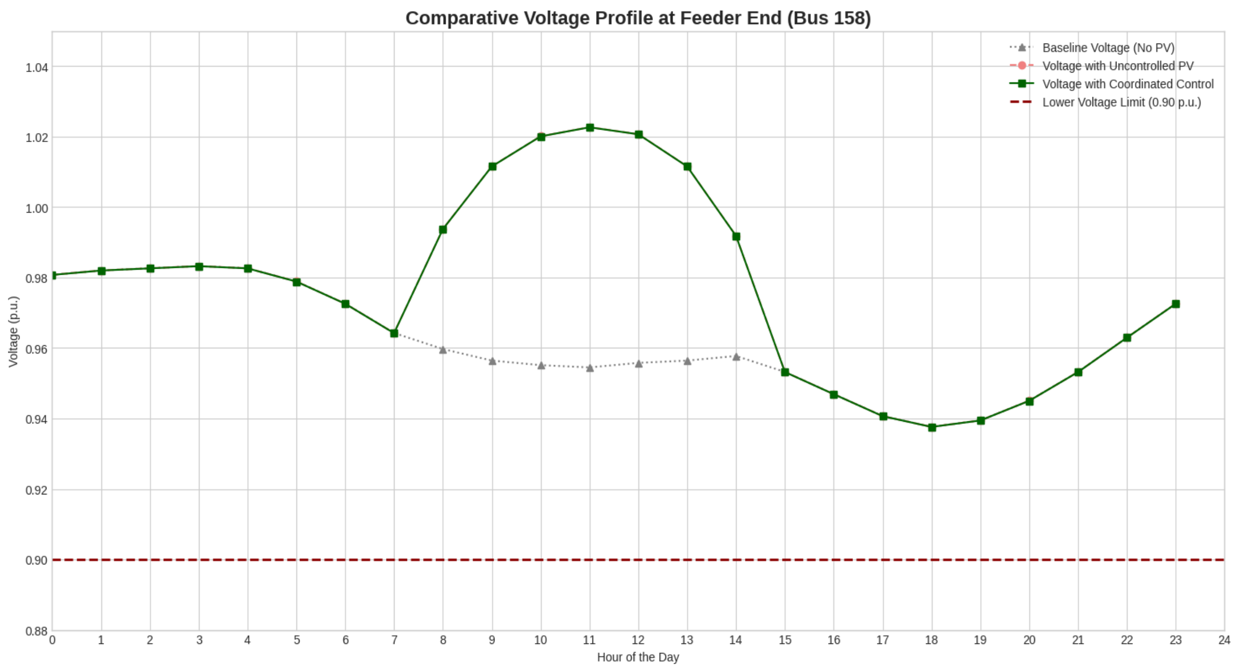

Figure 7 Impact of PV integration and control on the end-of-line voltage.

4.4. Seasonal Comparison: Rainy Season (Long Rains) Analysis

To assess whether RPF challenges persist across seasons, the simulation framework was replicated using rainy season (long rains, MAM) input profiles.

4.4.1. Rainy Season Baseline and Uncontrolled PV Results

Figure 8 presents the rainy season substation power flow. The reduced solar irradiance (peak ~0.60 p.u.) limited combined PV generation to approximately 1.8 MW at midday, compared to 3.0 MW during the dry season. This remained below the rainy season daytime load throughout the day. Consequently, no reverse power flow was observed – the minimum substation power flow stayed positive at approximately 0.8-1.0 MW during peak PV hours, contrasting sharply with the dry season's -0.93 MW reverse flow.

4.4.2 Rainy Season Voltage Profile Analysis

Figure 9 shows PV bus voltages during the rainy season. Maximum voltage reached only ~1.00 p.u., well below both the 1.04 p.u. generic threshold and the 1.02 p.u. adaptive threshold, and significantly lower than the dry season peak of 1.038 p.u.

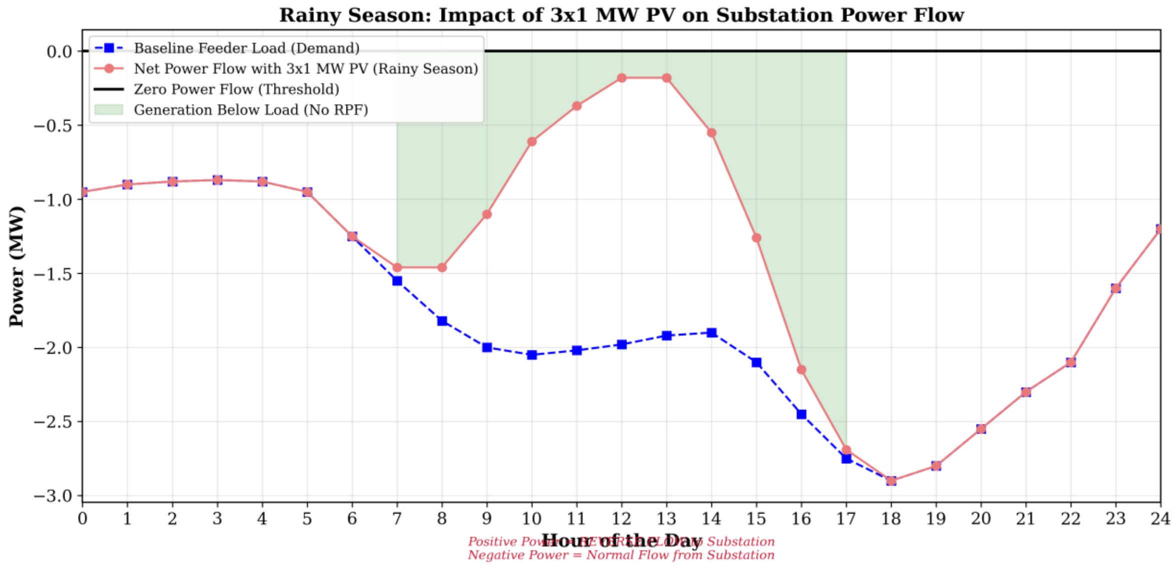

Figure 8 Substation power flow under rainy season conditions showing the absence of reverse power flow due to reduced PV generation

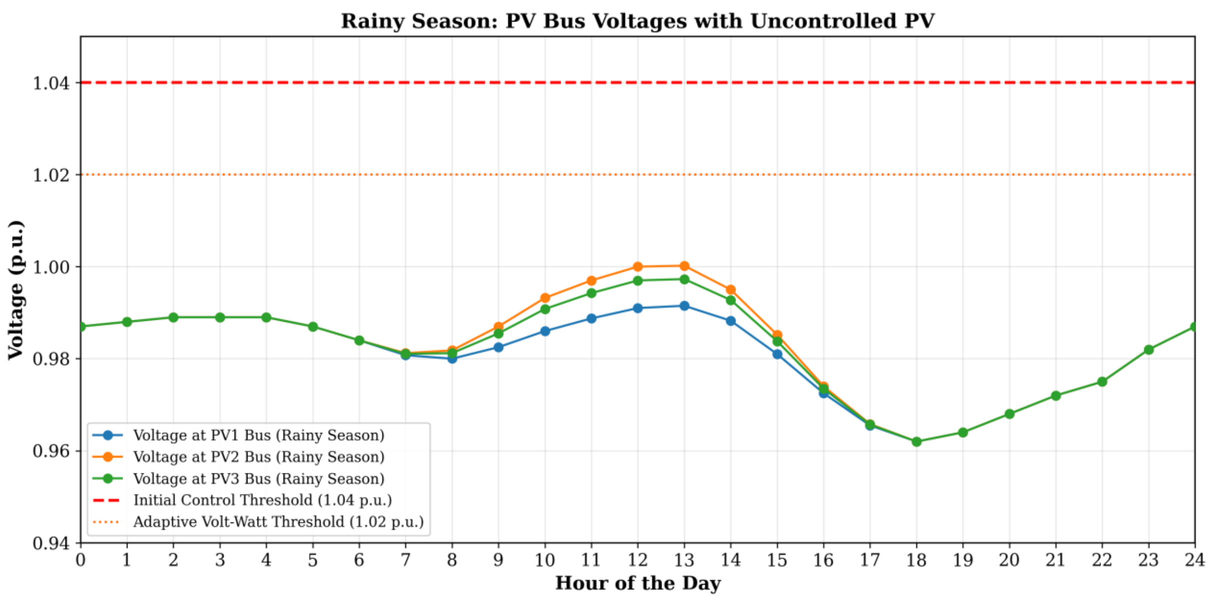

Figure 9 PV Bus voltage profiles during the rainy season, demonstrating minimal voltage rise due to reduced PV generation

4.4.3 Rainy Season Adaptive Control Performance

Under rainy season conditions, the adaptive control was largely inactive. Voltages stayed below the Volt-VAR (1.01 p.u.) and Volt-Watt (1.02 p.u.) activation thresholds, resulting in zero energy curtailment. The PV systems operated at full MPPT output, confirming the control is non-intrusive when grid constraints are not binding

4.5. Comparative Seasonal Discussion

Table 5 provides a comprehensive side-by-side comparison of the key performance metrics across both seasonal conditions and all simulation scenarios. This comparison clearly delineates the seasonal dependency of grid integration challenges and the context-specific value of the proposed control strategy.

Table 5 Comparative Seasonal Performance Metrics

Metric	Dry-Uncontrolled	Dry-Adaptive	Rainy-Uncontrolled	Rainy-Adaptive
Peak RPF	-0.93 MW	-0.35 MW	None	None
RPF Mitigation	0%	62.3%	N/A	N/A
Max Voltage	1.038 p.u.	1.012 p.u.	~1.00 p.u.	~1.00 p.u.
Daily Curtailment	0 kWh	~1,500 kWh	0 kWh	~0 kWh
Control Status	N/A	Active	N/A	Inactive

The seasonal comparison yields several important insights:
1. RPF is dry-season-specific: The ~35-45% irradiance reduction during the rainy season naturally eliminates generation-load mismatch, identifying the dry season as the design-critical period.
2. Seasonally intelligent control: The voltage-dependent activation provides inherent seasonal adaptability – active during dry season, dormant during rainy season – avoiding unnecessary curtailment.
3. Annual curtailment is lower than dry-season extrapolation: The ~1,500 kWh/day curtailment applies only during dry season months (~4-5 months), not year-round. Estimated annual curtailment is ~300,000 kWh vs. 547,500 kWh if extrapolated naively.

4.6. Analysis of Control Trade-offs, Energy Curtailment and Yield

A critical component of this study involved quantifying the energy curtailment losses and assessing the trade-off between grid compliance and energy yield. While highly effective in ensuring grid safety and stability, the adaptive control strategy inherently involves curtailing a portion of the available PV generation. Figure 10 presents the analysis of curtailed energy over the 24-hour period. To achieve the 62.3% reduction in RPF and maintain voltage stability, the control strategy necessitated the curtailment of approximately 1,500 kWh of otherwise available clean energy per day.

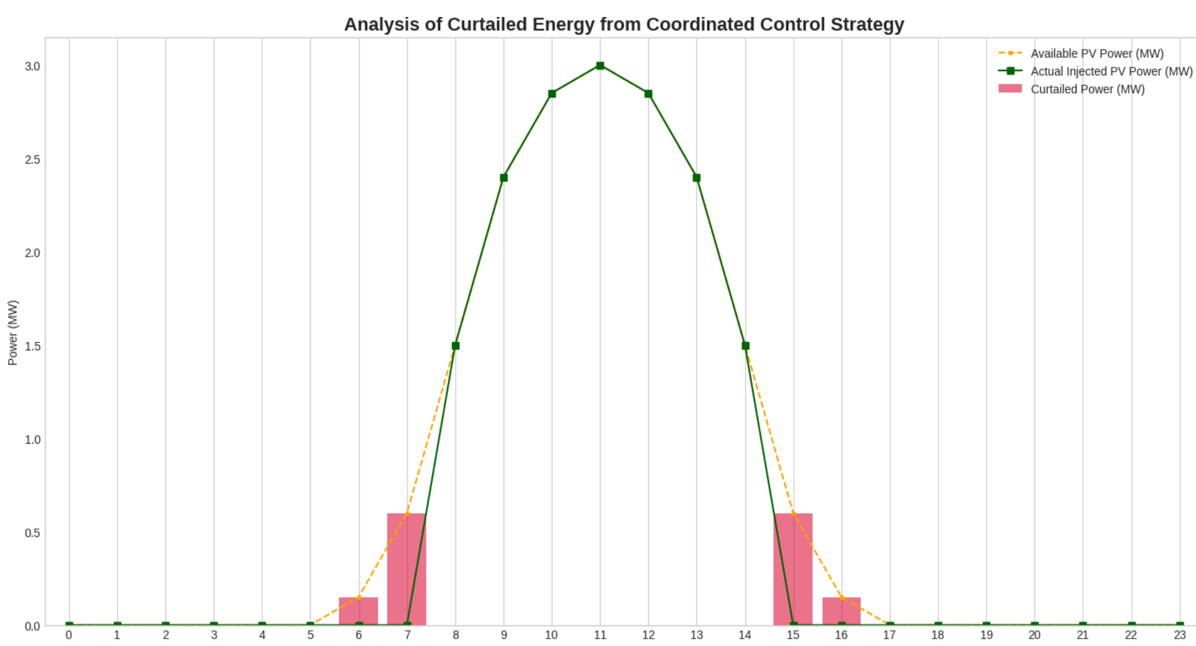

Figure 10 Analysis of energy curtailed by the coordinated control strategy to ensure grid safety

This curtailment occurs during periods of high solar irradiance and low load demand when the PV generation capability significantly exceeds the local consumption. The total curtailed energy ($E_{curtailed}$) was quantified using the relationship previously established in equation (4).

This quantification provides a crucial metric for decision-makers. It highlights a fundamental trade-off: improved grid safety and compliance (achieved through RPF mitigation and voltage stability) come at the cost of a certain amount of forgone renewable energy yield. Understanding this trade-off is vital for optimizing PV integration strategies, encouraging the exploration of complementary solutions such as energy storage or demand-side management to utilize curtailed energy in the future (Rajendran et al., 2025)). The results underscore the necessity of finding the optimal balance point where grid operational integrity is maintained with minimal impact on renewable energy harvesting.

Importantly, the seasonal analysis reveals that this curtailment cost is not uniform throughout the year. The ~1,500 kWh/day curtailment is representative of worst-case dry season conditions. During the rainy season (long rains), the adaptive control imposes effectively zero curtailment, as PV generation naturally remains below the levels that trigger control activation. Assuming approximately 150 dry season days and 100 transition days (with partial curtailment estimated at ~750 kWh/day) per year, the estimated total annual curtailment is approximately 300,000 kWh - substantially less than the 547,500 kWh that would be estimated by extrapolating the dry season curtailment across all 365 days. This more nuanced, seasonally-informed estimate provides a more realistic basis for economic assessments of PV integration under the proposed control strategy.

5. Conclusions

This study thoroughly investigated the critical challenges posed by high photovoltaic (PV) penetration in rural distribution feeders and proposed an adaptive smart inverter control strategy to mitigate these issues. Through comprehensive quasi-static time-series (QSTS) simulations on a validated OpenDSS model of a representative 69 km, 11kV rural feeder in Kenya, this research successfully addressed its stated objectives and research questions.

The initial modelling and analysis confirmed that a significant generation-load mismatch, arising from the cumulative impact of three 1 MW PV systems operating under conventional Maximum Power Point Tracking (MPPT), resulted in severe reverse power flow (RPF) of up to 0.93 MW back into the substation during midday. This condition was identified as a direct threat to grid stability and protection coordination, particularly for rural networks characterized by their high Resistance-to-Reactance (R/X) ratios.

A crucial finding of this research was the diagnosis of the feeder's inherent electrical stiffness. Despite substantial RPF, local voltages at PV connection points did not rise sufficiently (peaking at only 1.038 p.u.) to trigger generic, high-voltage-threshold Volt-Watt curtailment functions.

A key contribution to this study is the comparative seasonal analysis. Rainy season simulations confirmed that RPF does not occur during reduced-irradiance periods, as PV generation (~55-65% of dry season peak) remained below local demand. This establishes RPF as a seasonally bounded challenge. The adaptive control exhibited inherent seasonal intelligence, remaining inactive during the rainy season with zero curtailment, thereby preserving renewable energy yield during low-irradiance months.

The proposed load-following control demonstrated high effectiveness, successfully mitigating the peak RPF by 62.3%, reducing it from 0.93 MW to 0.35 MW. Concurrently, the strategy ensured robust voltage stability, maintaining all nodal voltages within statutory limits (e.g., ±5% of nominal voltage, as per IEEE Std 1547, 2018) throughout the 24-hour simulation period, a significant improvement over uncontrolled MPPT operation.

Finally, the study quantified the economic and operational trade-off associated with achieving grid compliance. The load-matching technique resulted in the curtailment of approximately 1,500 kWh of renewable energy per day. This quantification provides critical data for stakeholders, highlighting the balance required between maintaining grid integrity and maximizing clean energy yield in high-penetration scenarios. This work validates a practical, context-specific methodology for integrating high levels of PV into challenging rural distribution networks. It emphasizes that tailored, adaptive control strategies are indispensable, moving beyond generic solutions to achieve reliable and safe grid operation. Future research should focus on optimizing the trade-off by exploring advanced forecasting techniques, battery energy storage systems, or demand-side management to utilize curtailed energy, further enhancing the overall economic and environmental benefits of PV integration in rural settings.

Declaration of Ethical Standards

As the authors of this study, we declare that we comply with all ethical standards.

Credit Authorship Contribution Statement

Naomi Muthoni Kamunya: Conceptualization, Methodology, Software (OpenDSS), Data Curation, Investigation, Formal Analysis, Writing _ Original Draft, Visualization, Writing – Review & Editing.
Christopher Maina: Supervision, Conceptualization, Methodology, Writing – Review & Editing.
David Kimemia: Resources, Validation, Project Administration, Writing – Review & Editing.

Declaration of Competing Interest

The authors declared that they have no conflict of interest.

Funding / Acknowledgements

The authors declare that this research received no specific grant from any funding agency in the public, commercial, or not-for-profit sectors.
The authors declare that generative AI was used only for language editing and not for scientific content generation.

Data Availability

The Data that support the findings of this study are available from the Authors upon reasonable request.

References

Azzopardi, B., Gabdullin, Y., & Simkoniene, G. (2023). Photovoltaics and electrical vehicles mitigation on the low-voltage distribution network in Malta. IET Conference Proceedings, 2022(25), 554–556. https://doi.org/10.1049/icp.2023.0053.

Bhatt, P. K. (2022). Solar Energy Integration and Potential Challenges in Distribution Network: A Comprehensive Review. Journal of Energy Research and Reviews, 42–65.

De-Jesús-Grullón, R. E., Batista Jorge, R. O., Espinal Serrata, A., Bueno Díaz, J. E., Pichardo Estévez, J. J., & Guerrero-Rodríguez, N. F. (2024). Modeling and Simulation of Distribution Networks with High Renewable Penetration in Open-Source Software: QGIS and OpenDSS. Energies, 17(12), 2925. https://doi.org/10.3390/en17122925.

Hernández-Mayoral, E., Madrigal-Martínez, M., Mina-Antonio, J. D., Iracheta-Cortez, R., Enríquez-Santiago, J. A., Rodríguez-Rivera, O., Martínez-Reyes, G., & Mendoza-Santos, E. (2023). A Comprehensive Review on Power-Quality Issues, Optimization Techniques, and Control Strategies of Microgrid Based on Renewable Energy Sources. Sustainability, 15(12), 9847. https://doi.org/10.3390/su15129847.

Kariuki, B. W., & Sato, T. (2018). Interannual and spatial variability of solar radiation energy potential in
Kenya using Meteosat satellite. Renewable Energy, 116, 88-96. https://doi.org/10.1016/j.renene.2017.09.069.

Khan, H. A., & Rihan, M. (2022). Voltage Regulation Challenges in Highly Solar PV Penetrated Distribution Networks. 2022 1st International Conference on Sustainable Technology for Power and Energy Systems (STPES), 1–6. https://doi.org/10.1109/stpes54845.2022.10006622.

Khatib, T., & Sabri, L. (2021). Grid Impact Assessment of Centralized and Decentralized Photovoltaic-Based Distribution Generation: A Case Study of Power Distribution Network with High Renewable Energy Penetration. Mathematical Problems in Engineering, 2021, 1–16. https://doi.org/10.1155/2021/5430089.

Mehrez, S., Morgan, M., & El Sobki, M. S. (2023). Over Voltage Mitigation in Distribution Systems with High PV Penetration. 2023 24th International Middle East Power System Conference (MEPCON), 1–7. https://doi.org/10.1109/MEPCON58725.2023.10462377.

Mohanty, S., Tripathy, S., Ghatak, S. R., & Mohapatra, A. (2022). Impact Assessment of PV Penetration on Unbalanced Distribution network with Dynamic load condition. 2022 2nd International Conference on Power Electronics & IoT Applications in Renewable Energy and Its Control (PARC), 1–6. https://doi.org/10.1109/PARC52418.2022.9726552.

Okemo, A., Muriithi, C. M., & Nderu, J. (2026). Automated Conversion of Unstructured Geospatial Feeder Data into Analytical Models: An 11 kV Case Study. Electrical Engineering and Energy (ELENE), 1. https://doi.org/10.64470/elene.2026.20.

Pato, P. A. V., Trindade, F. C. L., & Wang, X. (2023). Hosting high PV penetration on distribution feeders with smart inverters providing local var compensation. Electric Power Systems Research, 217, 109168. https://doi.org/10.1016/j.epsr.2023.109168.

Rajendran, G., Raute, R., & Caruana, C. (2025). A Comprehensive Review of Solar PV Integration with Smart-Grids: Challenges, Standards, and Grid Codes. Energies, 18(9), 2221. https://doi.org/10.3390/en18092221

Sharma, V., Haque, M. H., Aziz, S. M., & Kauschke, T. (2023). Smart inverter and battery storage controls to reduce financial loss due to overvoltage-induced PV curtailment in distribution feeders. Sustainable Energy, Grids and Networks, 34, 101030. https://doi.org/10.1016/j.segan.2023.101030.

Wadie, F. (2023). Analysis of the Integrated Effect of Temporary Overvoltages, PV Transformer Connection and Overcurrent Protection in Hybrid PV-Wind Energy System. Electric Power Systems Research, 216, 109084. https://doi.org/10.1016/j.epsr.2022.109084.

Wu, J., Yuan, J., Weng, Y., & Ayyanar, R. (2023). Spatial-Temporal Deep Learning for Hosting Capacity Analysis in Distribution Grids. IEEE Transactions on Smart Grid, 14(1), 354–364. https://doi.org/10.1109/tsg.2022.3196943

Wu, M., Hong, L., Wang, Y., Yan, Z., & Chen, Z. (2022). Volt-VAR control for distribution networks with high penetration of DGs: An overview. The Electricity Journal, 35(5), 107130. https://doi.org/10.1016/j.tej.2022.107130.

Xu, R., Zhang, C., Xu, Y., Dong, Z., & Zhang, R. (2022). Multi-Objective Hierarchically-Coordinated Volt/Var Control for Active Distribution Networks with Droop-Controlled PV Inverters. IEEE Transactions on Smart Grid, 13(2), 998–1011. https://doi.org/10.1109/TSG.2021.3126761.